FROM CINDER CONES TO SUBDUCTION ZONES: VOLATILE RECYCLING AND

MAGMA FORMATION BENEATH THE SOUTHERN CASCADE ARC

by

KRISTINA JANINE WALOWSKI

A DISSERTATION

Presented to the Department of Geological Sciences
and the Graduate School of the University of Oregon
in partial fulfillment of the requirements
for the degree of
Doctor of Philosophy

June 2015

DISSERTATION APPROVAL PAGE

Student: Kristina Janine Walowski

Title: From Cinder Cones to Subduction Zones: Volatile Recycling and Magma Formation beneath the Southern Cascade Arc

This dissertation has been accepted and approved in partial fulfillment of the requirements for the Doctor of Philosophy degree in the Department of Geological Sciences by:

Dr. Paul Wallace   Chairperson
Dr. Ilya Bindeman   Core Member
Dr. Gene Humphreys   Core Member
Dr. Darren Johnson   Institutional Representative

and

Scott L. Pratt   Dean of the Graduate School

Original approval signatures are on file with the University of Oregon Graduate School.

Degree awarded June 2015

DISSERTATION ABSTRACT

Kristina Janine Walowski

Doctor of Philosophy

Department of Geological Sciences

June 2015

Title: From Cinder Cones to Subduction Zones: Volatile Recycling and Magma
Formation beneath the Southern Cascade Arc

Volatiles (H_2O, CO_2, S, Cl) play a key role in magmatic processes at subduction zones. In this study, the dissolved volatile contents of olivine-hosted melt inclusions from cinder cones in the Lassen segment of the Cascade arc are used to investigate dehydration of subducted oceanic lithosphere, magma formation in the sub-arc mantle wedge, and mafic magma storage and evolution in the crust.

Relatively young, hot oceanic lithosphere subducts beneath the Cascade arc. The hydrogen-isotope and trace-element compositions of melt inclusions, when integrated with thermo-petrologic modeling, demonstrate that fluids in Cascade magmas are sourced from hydrated peridotite in the deep slab interior and that the oceanic crustal part of the slab extensively dehydrates beneath the forearc. In contrast to their slab-derived H, the melt inclusions have B concentrations and isotope ratios that are similar to mid-ocean ridge basalt (MORB), requiring little to no slab contribution of B, which is also consistent with extensive dehydration of the downgoing plate before it reaches sub-arc depths. Correlations of volatile and trace element ratios in the melt inclusions (H_2O/Ce, Cl/Nb, Sr/Nd) demonstrate that geochemical variability in the magmas is the result of variable amounts of addition of a hydrous subduction component to the mantle wedge. Radiogenic

isotope ratios require that the subduction component has less radiogenic Sr and Pb and more radiogenic Nd than the Lassen sub-arc mantle and is therefore likely to be a partial melt of subducted Gorda MORB. These results provide evidence that chlorite-derived fluids from the deep slab interior flux-melt the oceanic crust, producing hydrous slab melts that migrate into the overlying mantle, where they react with peridotite to induce further melting.

The basaltic magmas that erupted at Cinder Cone near Mt. Lassen trapped melt inclusions during olivine crystallization at ~7-15 km depth. The melt inclusion compositions require that two different mantle-derived magmas were involved in the eruption, and temporal changes show that arrival of the two batches correlates with two explosive phases of activity. Both magmas experienced rapid crustal contamination before erupting, illustrating the complexities of cinder cone eruptions.

This dissertation includes previously published and unpublished co-authored material.

CURRICULUM VITAE

NAME OF AUTHOR: Kristina Janine Walowski

GRADUATE AND UNDERGRADUATE SCHOOLS ATTENDED:

University of Oregon, Eugene
University of California, Los Angeles

DEGREES AWARDED:

Doctor of Philosophy, Geological Sciences, 2015, University of Oregon
Bachelor of Science, Geology, 2015, University of California, Los Angeles

AREAS OF SPECIAL INTEREST:

Geochemistry, Petrology, Volcanology

PROFESSIONAL EXPERIENCE:

Graduate Teaching Fellow (2010-2015).
University of Oregon, Department of Geological Sciences
Research Assistant (2011-2015)
University of Oregon, Department of Geological Sciences
Advisor: Paul Wallace
Undergraduate Research Assistant (2008-2010)
University of California, Los Angeles, Department of Earth and Space
Sciences
Advisor: Jeremy Boyce

GRANTS, AWARDS, AND HONORS:

GeoPRISMS AGU Student Prize for Best Oral Presentation (2014).
McMurray Award (2014). Department of Geological Science, University of
Oregon.
Goldschmidt Student Travel Grant (2013). Geochemical Society.
Graduate Research Award (2013). Graduate School, University of Oregon.
GeoPRISMS AGU Student Prize Honorable Mention (2012).
Staples Scholarship (2012). Department of Geological Science, University of
Oregon.
Valedictorian (2010), Department of Earth and Space Sciences, University of
California, Los Angeles.

PUBLICATIONS:

Walowski, K. J., Wallace, P. J., Hauri, E. H., Wada, I., & Clynne, M. A. (2015). Slab melting beneath the Cascade Arc driven by dehydration of altered oceanic peridotite. *Nature Geoscience*, 8(5), 404-408.

Walowski K, Wallace P, Clynne M. (2014). Slab Melting and Magma Formation beneath the southern Cascade Arc. *AGU Fall Meeting Abstracts*, V31G-03.

Walowski K, Wallace P, Hauri E, Clynne M & Wada I (2014). Slab Dehydration beneath the Southern Cascade Arc Inferred from B and H Isotopes. *Goldschmidt Abstracts*, 2014, 2613.

Walowski, K. J., Wallace, P. J., Hauri, E. H., Clynne, M. A., Rea, J., & Rasmussen, D. J. (2013). Magma formation in hot-slab subduction zones: Insights from hydrogen isotopes in Cascade Arc melt inclusions. In *AGU Fall Meeting Abstracts* (Vol. 1, p. 01).

Walowski K, Wallace P, Clynne M, Wada I & Rasmussen D (2013). Magma Formation in Hot-Slab Subduction Zones: Insights from Volatile Contents of Melt Inclusions from the Southern Cascade Arc. *Mineralogical Magazine*, 77(5), 2441.

Walowski K, Wallace P, Clynne M, Wada I & Rasmussen D (2012). Understanding magma formation and mantle conditions in the Lassen segment of the Cascade Arc: Insights from volatile contents of olivine-hosted melt inclusions. *AGU Fall Meeting Abstracts,* V14B-01.

Walowski, K. J., Wallace, P. J., Cashman, K. V., & Clynne, M. A. (2011). Inferring the magmatic plumbing system and melt evolution from olivine-hosted melt inclusions at Cinder Cone, Lassen Volcanic National Park, California. In *AGU Fall Meeting Abstracts* (Vol. 1, p. 02).

Walowski, K. J., and Boyce, J.W. (2009). Volatile History of the Bishop Tuff from Apatite Phenocrysts and Inclusions. *AGU Fall Meeting Abstracts,* V23C-2093.

ACKNOWLEDGMENTS

I'd also like to thank the incredible graduate community that I was so lucky be a part of. To the few who were there from start to finish – Kristin Sweeney, Corina Cerovski-Darriau, and Scott Maguffin – we've had a great run, and I hope it doesn't end here! Special thanks to Angie Seligman, who the first floor would not have been the same without, Randy Krogstad, who will always be one of my best friends, Amberlee Darold and Gillean Arnoux, who made Cascade 124 a better place, and, of course, Captain

Malcom Reynolds.

I'd also like to specially thank my first academic 'dad', Jeremy Boyce. He inspired me to follow this path and prepared me so well for the journey that has been my Ph.D. Five years later, he is still there for me whenever I need advice and guidance, which is something I truly value.

To my Mom and Dad, I could never thank you enough for your unconditional love and support. You have both taught me so much, and given me everything I could have ever needed. It is difficult to put into words how much you both mean to me, and I love you both very much. To my brother, Chris, thank you for showing me the coolness of science. I truly value our friendship and look forward to joining you in the higher-ed scientist club. Finally, I'd like to thank my partner Alexander Handwerger, without whom none of this would have been possible. Thank you for being there for me every single step of the way, and bringing me so much happiness. Our time in Oregon has been incredible, and I can't wait to start our next adventure together in Scotland!

To My Family

TABLE OF CONTENTS

LIST OF FIGURES

LIST OF TABLES

CHAPTER I

INTRODUCTION

1.1. Water, Subduction, and the Cascade Arc

The distribution of water in the Earth's mantle has a strong impact on the evolution of our planet. Introduced to the mantle through subduction, water makes active plate tectonics possible on Earth by reducing rock viscosities, facilitating mantle convection (e.g. Jung and Karato, 2001). Melting of the mantle wedge in subduction zones would not be possible without the addition of water (e.g., Ringwood, 1974), and once these melts reach the surface, their water contents directly affect the explosivity of the magma (e.g., Roggensack, 1997; Metrich and Wallace, 2008). The influence water has on a number of processes, such as the formation of volcanic arcs and production of continental crust, makes understanding the origins and distribution of water in subduction zones a very important area of research in the earth sciences.

Perhaps the most important role of H_2O in subduction zones is driving magma production. When the oceanic lithosphere is subducted, increasing temperatures and pressures cause the progressive breakdown of hydrous phases in a series of reactions that release H_2O into the overlying mantle wedge (e.g., Schmidt and Poli, 1998). In the classic model of petrogenesis at subduction zones, these aqueous fluids infiltrate the mantle wedge, lower the solidus, and cause melting. However, convergent margins vary globally - they subduct oceanic lithosphere of different ages and at different rates (e.g., Syracuse et al., 2010), and have sediment packages of different thicknesses and compositions (e.g., Plank & Langmuir, 1993). Different combinations of plate age and convergence rate

control how rapidly temperatures in the slab increase with depth, and therefore influence the depths at which dehydration reactions occur (e.g., Schmidt & Poli, 1998; Hacker, 2008), and the composition of the fluids and/or melts that infiltrate the mantle wedge (e.g., Kessel et al., 2005).

The Cascadia subduction zone, which runs from northern California to southern British Columbia, represents a global endmember, subducting very young oceanic lithosphere (6-10 Ma at the trench; Wilson et al., 2002, Kirby et al., 2002). The processes that drive magma formation beneath the Cascade arc and other warm-slab subduction zones have been debated because young oceanic crust should largely dehydrate beneath the forearc (Van Keken et al., 2010), where the mantle wedge is not at high enough temperatures to melt. In addition, geochemical variability along strike in the Cascades has led to contrasting interpretations about the role of volatiles in magma generation (e.g., Leeman et al., 1990; Grove et al., 2002; Ruscitto et al., 2010). In this dissertation, I focus on the Lassen segment of the Cascade arc, where previous studies have demonstrated that across-arc geochemical variations in primitive basaltic magmas result from varying extents of mantle wedge fluxing by material recycled from the slab. Using direct measurements of dissolved magmatic volatiles and a number of other geochemical tools, I show how the subduction of warm oceanic lithosphere beneath the Cascades influences dehydration reactions in the downgoing slab and melt production in the mantle wedge.

1.2. Scientific Approach

Volatiles, such as H_2O, CO_2, S, Cl, and F, play a key role a number magmatic processes. Pre-eruptive volatile contents are difficult to estimate, however, because they

2

decrease in solubility as pressure decreases and exsolve from the magma during ascent, driving explosive eruptions (e.g., Roggensack, 1997; Metrich and Wallace, 2008). As a result, most magmatic volatiles are lost to the atmosphere, leaving the resulting volcanic material with only a small fraction of the volatile contents with which it began (e.g., Holloway and Blank, 1994). In this dissertation, I utilize the geochemistry of melt inclusions hosted in olivine crystals to get around this problem. Melt inclusions are small volumes of melt trapped inside of phenocrysts at depth. Olivine-hosted melt inclusions are one of the best tools currently available to directly measure pre-eruptive volatile concentrations, because they are often trapped at depth, before significant degassing occurs (Anderson, 1974; Schiano, 2003). Because they are trapped at depth, they not only provide estimates of pre-eruptive volatiles, but may also provide a unique snapshot of melt compositions, before magmatic evolution occurs.

1.3. Dissertation Organization

This dissertation is separated into three stand-alone chapters that are prepared as individual manuscripts for publication. Chapters II and III investigate deep magmatic processes, such as mantle melting and slab recycling, while Chapter IV focuses on shallow (crustal level) magmatic processes that occur prior to and during cinder cone eruptions. The unifying theme of the dissertation is the use of melt inclusions in olivine sampled from tephra deposits at mafic cinder cones. Throughout the dissertation, I show that melt inclusion datasets can be utilized to answer a wide range of questions when integrated with other types of data (e.g., radiogenic isotopes, mineral chemistry, eruptive

stratigraphy) and modeling (e.g., geodynamic, geochemical, and thermodynamic modeling).

In Chapter II, "Slab Melting beneath the Cascade Arc driven by dehydration of altered oceanic peridotite," I use the hydrogen isotope composition of basaltic melt inclusions from seven different cinder cones to fingerprint the fluid sources that initiate magma generation beneath the Cascade arc. I also develop a thermo-petrologic model to calculate progressive D/H fractionation in the subducting plate to inform the geochemical data. The results show that the downgoing plate beneath the southern Cascades experiences extensive dehydration and that fluids derived from the slab interior may flux-melt the slab top. In Chapter III, "Slab Melting and Magma Formation beneath the Southern Cascade Arc," I use a larger melt inclusion dataset to further test the interpretations presented in Chapter II. I use B concentrations and isotope ratios, trace elements, and the volatile concentrations of the melt inclusions along with the radiogenic isotope ratios of bulk tephra from the eight different cinder cones (one additional cone to the seven discussed in Chapter II). This dataset is used to demonstrate that geochemical variability of primitive basalts in the Lassen region is the result of variable amounts of addition of a hydrous subduction component to the mantle wedge, and also provides strong evidence that melting of the subducted basaltic oceanic crust beneath the Lassen region plays an important role in magma formation in the mantle wedge. The combined results of Chapters II and III indicate that chlorite-derived fluids from the deep slab interior can flux-melt the oceanic crust, producing hydrous slab melts that migrate into the overlying mantle, where they react with peridotite to induce further melting. I suggest that this mechanism for slab melting and magma formation may be common in arcs

beneath which young oceanic crust subducts, such as central Mexico (e.g., Cai et al., 2014).

In Chapter IV, I investigate the compositional evolution of magmas from the youngest cinder cone in the Cascade arc, Cinder Cone (eruption age 1666 C.E.; Sheppard et al., 2009). I integrate melt inclusion compositions with stratigraphic information, bulk lava and tephra compositions, mineral chemistry, and physical volcanology to better understand the processes and timescales associated with the storage, ascent, and eruption of magmas at this monogenetic volcano. I find that two different mantle-derived magmas were tapped during the eruption of Cinder Cone, correlating with two explosive eruptive phases. Both magmas experienced rapid crustal contamination before erupting at the surface similar to other well-documented cinder cone eruptions (e.g., Paricutin and Jorullo, in Meixco; e.g., Pioli et al., 2008, Johnson et al., 2008). However, the timescales and mechanisms of contamination and eruption are shown to occur more rapidly at Cinder Cone than monogenetic volcanoes in central Mexico, illustrating the complexities of short-lived cinder cone eruptions.

For all chapters in this dissertation, I am the first author, and performed all of the laboratory work, field-based work, and analytical work, unless explicitly stated. Chapter II has been published in *Nature Geoscience* with Dr. Paul Wallace (advisor), Dr. Erik Hauri (Carnegie Instiution of Washington), Dr. Ikuko Wada (University of Minnesota), and Dr. Michael Clynne (U.S. Geological Survey). Chapter III is in preparation in the style of *Earth and Planetary Science Letters* and will be coauthored by Dr. Paul Wallace (advisor), Dr. Michael Clynne (U.S. Geological Survey), Dan Rassmussen (Ph.D. candidate, Lamont-Doherty Earth Observatory), and Dr. Dominique Weis (University of

British Columbia). Chapter IV is in preparation in the style of *Bulletin of Volcanology* and will be coauthored by Dr. Paul Wallace (advisor), Dr. Michael Clynne (U.S. Geological Survey), Dr. Kathy Cashman (University of Bristol), J. Katie Marks (M.S., University of Oregon), and Dr. Philipp Ruprecht (Lamont-Doherty Earth Observatory).

CHAPTER II

SLAB MELTING BENEATH THE CASCADE ARC DRIVEN BY

DEHYDRATION OF ALTERED OCEANIC PERIDOTITE

This work was published in volume 8 of the journal *Nature Geoscience* in May, 2015. Sample collection was performed by me with the help of Dr. Wallace and Dr. Clynne. Sample preparation for and Nano-secondary ion mass spectrometry volatile and hydrogen isotope analyses were performed by me with the help of Dr. Hauri. Data corrections, analyses, and interpretation were performed by me, with the help of Dr.Wallace. The fractionation model was created by me with the help of Dr. Wada and incorporated her previously published work. I drafted all the figures used in this article and the text was written by me, with editorial assistance by Dr. Wallace.

2.1. Introduction

Water is returned to Earth's interior at subduction zones. However, the processes and pathways by which water leaves the subducting plate and causes melting beneath volcanic arcs are complex; the source of the water—subducting sediment, altered oceanic crust, or hydrated mantle in the downgoing plate—is debated; and the role of slab temperature is unclear. Here we analyse the hydrogen-isotope and trace-element signature of melt inclusions in ash samples from the Cascade Arc, where young, hot lithosphere subducts. Comparing these data with published analyses, we find that fluids

in the Cascade magmas are sourced from deeper parts of the subducting slab—hydrated mantle peridotite in the slab interior—compared with fluids in magmas from the Marianas Arc, where older, colder lithosphere subducts. We use geodynamic modelling to show that, in the hotter subduction zone, the upper crust of the subducting slab rapidly dehydrates at shallow depths. With continued subduction, fluids released from the deeper plate interior migrate into the dehydrated parts, causing those to melt. These melts in turn migrate into the overlying mantle wedge, where they trigger further melting. Our results provide a physical model to explain melting of the subducted plate and mass transfer from the slab to the mantle beneath arcs where relatively young oceanic lithosphere is subducted.

The Cascadia subduction zone and associated magmatic arc in the U.S. and Canada is a global endmember example of a "warm-slab" subduction zone [1,2], in which very young (6-9 Ma at the trench)[3] and therefore hot oceanic crust subducts (Fig. 2.1). Such arcs have proven to be a challenge to our current understanding of arc magmatism because the hotter nature of the young subducted plate causes most dehydration of the oceanic crust to occur beneath the forearc rather than the arc[4,5]. As a result, little H_2O may reach sub-arc depths to initiate melt production in the overlying mantle wedge, unless there is substantial H_2O carried to greater depths by hydrated (serpentinized) peridotite in the mantle portion of the downgoing slab[6]. Basaltic magmas in the Cascades have H_2O contents (3.2 ±1.2 wt%)[7,8,9] that are only slightly lower than the global arc average (3.9±0.45 wt%, 1 s.d.)[10], raising questions about the extent of dehydration of the subducting plate beneath the forearc and the extent to which hydrated mantle in the subducting plate carries H_2O to sub-arc depths.
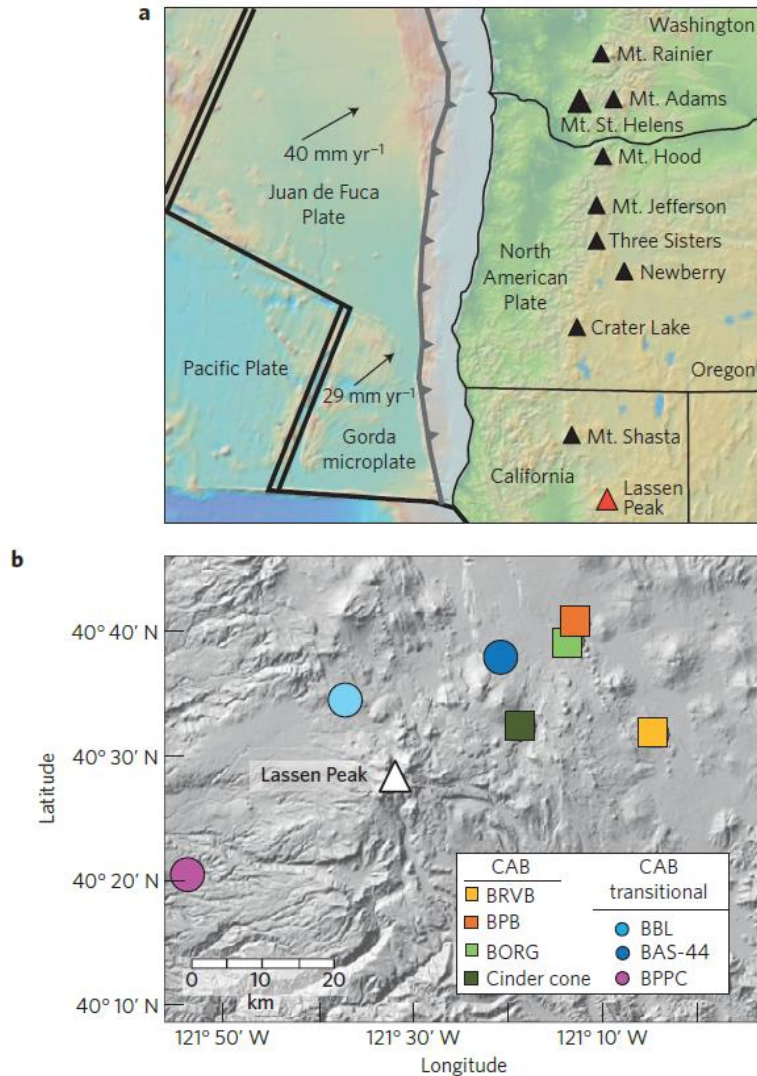
Figure 2.1. Cascade arc regional map and Lassen sample locations. a) Regional map of the Northwestern United States showing major tectonic boundaries. Black arrows show the direction and convergence rate of the Juan de Fuca and Gorda plates. Lassen Peak (red triangle) represents the southernmost active volcanic center of the Quaternary Cascade arc. b) Expanded map of the Lassen Region with locations of Quaternary cinder cones sampled in this study. Symbols and colors for calc-alkaline basalt (CABs; squares) and CAB-transitional (circles) samples are used throughout the article.

Hydrogen isotopes have a larger mass difference than any other isotope pair, and as a result, they exhibit strong isotopic fractionation during various geologic processes. In subduction zones, as hydrous minerals break down with increasing temperature and

pressure, the D/H ratio is fractionated, producing D-enriched fluids and a complementary residual slab that is isotopically lighter[11]. Recent work in the Marianas has shown that because the contribution of D and H from the overlying mantle is minimal, the δD signature ($\delta D=1{,}000 \times [(D/H)_{sample} - (D/H)_{SMOW}] / (D/H)_{SMOW}$, where SMOW is standard mean ocean water with $\delta D=0$) of slab fluids may be retained in primitive arc magmas[11]. This makes magmatic D/H ratios a valuable tool for investigating volatile recycling in the Cascade arc because the thermal structure of the slab strongly influences the depths at which key dehydration reactions occur in the downgoing plate[6,12].

Here we focus on the Lassen segment of the Cascade arc, the southernmost active segment of the arc, where previous work has shown across-arc geochemical variations related to subduction enrichment[13,14] (Fig. 2.1a). Our samples were collected from tephra deposits associated with primitive basaltic cinder cones (MgO > 7 wt%; Supplementary Table A.1; see Appendix A for all supplementary information for this chapter), which span ~80 km across the arc axis (Fig. 2.1b). Melt inclusions – glassy "blobs" of silicate melt trapped inside olivine crystals – were used in this study to measure pre-eruptive volatile contents. We present the analyses of melt inclusions from four calc-alkaline basalts (CAB) and three basalts that are transitional between CAB and low-K tholeiite (LKT) based on trace element patterns (Supplementary Fig. A.1). Using the maximum volatile contents at each cone to represent the undegassed magma, we find values of 2.47-3.4 wt% H_2O for CABs and 1.3-1.4 wt% H_2O for transitional CABs in the Lassen region (Table 2.1). The CAB values are similar to H_2O contents of other Cascade CAB magmas[7,8,9], whereas the transitional CABs have lower values, as expected, given that

they are transitional towards LKTs, which are interpreted to be relatively dry magmas formed by decompression melting[15].

Table 2.1. Average volatile, trace element and stable isotope composition of melt inclusions from Lassen Region cinder cones.

	Average volatile, trace element and stable isotope compositions of melt inclusions from Lassen Region cinder cones.									
Sample	$\delta D_{avg.\ measured}$* (‰)	$\delta D_{lowest\ measured}$ (‰)	$\delta D_{initial}$ (‰)	H_2O_{max} (wt%)	H_2O_{max}/Ce	$(Sr/P)_N$	La/Yb	Nb/Zr	SiO_2 (wt%)	Olivine Fo
BBL	−66	−79	−85	1.40	802	1.18	3.45	0.0429	49.76	84–87
BAS-44	−52	−53	−70	1.30	521	1.80	3.31	0.0341	49.66	87–88
BPPC	−46	−56	−75	2.47	1,503	2.81	2.97	0.0239	51.70	86–88
BRVB	−33	−42	−75	2.60	702	1.19	8.04	0.0705	49.73	84–86
BORG	−58	−67	−90	3.40	2,026	2.87	3.84	0.0413	50.49	86–89
Cinder cone	−67	−83	−95	3.20	1,329	1.46	5.01	0.0602	51.85	89–90
BPB	−36	−37	−80	3.23	969	1.31	6.91	0.0591	51.94	85–87

*$\delta D_{avg.\ measured}$ is the average of measured values excluding those severely effected by post-entrapment hydrogen loss. $\delta D_{initial}$ is a calculated best estimate of the initial δD after correction for diffusive hydrogen loss (see Supplementary Fig. 3 and Methods). SiO_2 and Olivine Fo (forsterite content) are averages and ranges, respectively, taken from a larger melt inclusion data set (see Supplementary Methods).

In addition to H_2O, trace element ratios of large ion lithophile elements (LILE) and light rare earth elements (LREE) are also commonly used to distinguish addition of a hydrous subduction component to the mantle source because of the fluid mobility of LILEs and relative depletion of LREE in the mantle wedge. In the Lassen region, $(Sr/P)_N$ (N refers to normalization to primitive mantle[16]) has been used to distinguish a subduction component because it correlates with LILE/LREE ratios and varies systematically across the arc[13,14]. For magmas from the Lassen region, $(Sr/P)_N$ correlates with other slab component tracers such as H_2O/Ce (Fig. 2.2a), demonstrating a clear link between volatile and trace element enrichment of the mantle wedge as the result of variable addition of a hydrous slab component.

2.2. Slab Surface Temperatures

To better understand thermal conditions at the slab-wedge interface, we developed a 2-D steady-state thermal model for this region[2]. The maximum depth of slab-

mantle decoupling (MDD) controls the trench-ward extent of solid mantle wedge flow, and this depth tends to be 70-80 km for most subduction zones[2]. In our model for the Lassen segment, we assume that the MDD is 75 km. Temporal changes in regional tectonics or slab geometry can cause deviation from the common MDD. Thus, the range of slab surface temperatures predicted by models with MDD of 65–85 km depth are shown in Figure 2.2b. We also calculated slab surface temperatures using the H_2O/Ce ratio[17] (see Supplementary Information A.) as an independent comparison with the thermal model. Slab surface temperatures at sub-arc depths of ~85-95 km[18] beneath the Lassen segment calculated using this method are 725-850 ± 50 °C (Fig. 2.2b), slightly lower than temperatures predicted by the thermal model. Our thermal model does not include the effects of fluid circulation within the oceanic crust at shallow depths in the subduction zone or the latent heat of fusion that would affect temperatures if the oceanic crust at the plate top was partially melted (see Supplementary Information A.2). Each of these effects could reduce the slab surface temperatures by ~50 °C[19]. Furthermore, in interpreting H_2O/Ce temperatures, we neglect the potential effects of lateral migration of fluids and melts through the wedge[20] which may contribute to the difference between the two estimates (see Supplementary Information A.2). Regardless of the small offset, both the thermal model and H_2O/Ce temperature estimates indicate active fluxing of hydrous material from the slab into the mantle wedge beneath the arc rather than down-dragging of hydrous mantle from the forearc region. If the latter was an important process, it would have imprinted the mantle wedge with relatively high H_2O/Ce, resulting in lower apparent temperatures[17]. Calculated slab surface temperatures beneath the Cascades (from both methods) also plot at or above the solidi of both mid-ocean ridge basalt

(MORB)+H_2O[21] and sediment+H_2O[22] (Fig. 2.2b), indicating the likelihood of partial melting of the slab top if H_2O is present.
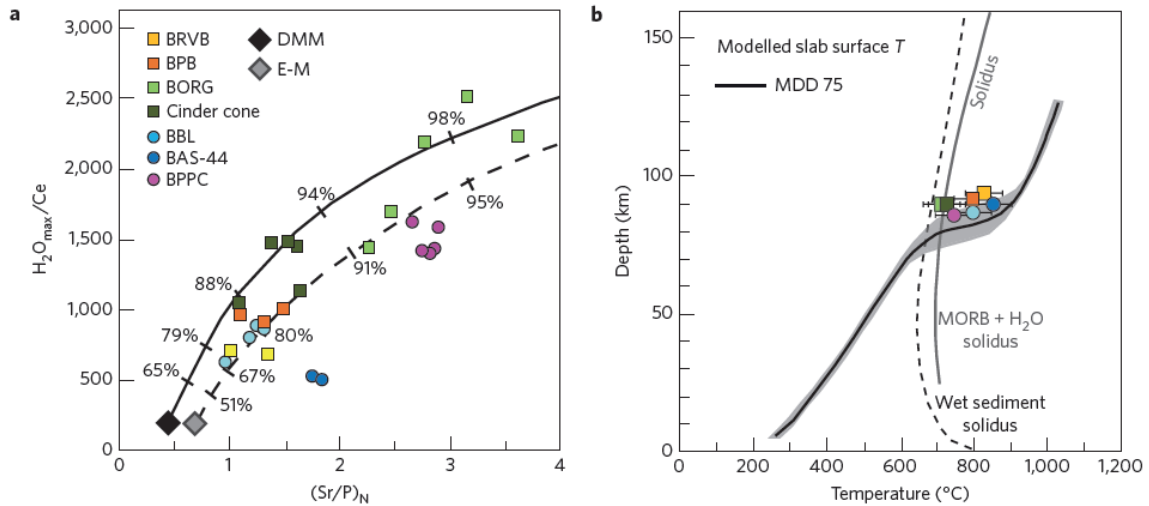
Figure 2.2. Melt inclusion compositions and slab surface temperatures. a) H_2O_{max}/Ce versus $(Sr/P)_N$ for least degassed melt inclusions. 10% partial melts of depleted mantle (DMM)[46] and more enriched mantle[47] (E-M; 66% DMM and 33% E-M; see Supplementary Fig. A.2 and Information) mixed with a hydrous component were used to calculate curves, labeled with the % of total H_2O contributed by the subduction component in the final magma. b) Slab surface temperatures from the H_2O/Ce thermometer[17], 2-D thermal model for the Lassen segment (MDD of 75 km; solid black curve), and the sediment + H_2O [22] and MORB + H_2O solidi[21]. Temperatures predicted by thermal models with MDDs of 65–85 km shown by grey shaded region.

2.3. Hydrogen Isotopes

The melt inclusion data from the Lassen region show a negative correlation between measured δD values and H_2O (Supplementary Fig. A.3). Recent experimental work demonstrates that this correlation is the result of post-entrapment fractionation caused by preferential diffusive loss of H relative to D through the olivine host[23, 24], and

13

our data show the first evidence for this process in naturally glassy samples (Supplementary Fig. A.3). Using a diffusive re-equilibration model[24], we calculated the initial δD composition for each cone by assuming that the highest H_2O concentrations measured are in melt inclusions that are least affected by this process (Supplementary Fig. A.3). We compare our results (Fig. 2.3a) with published data from the Marianas[11] where negative correlations between δD and H_2O wt% are not observed. The Marianas data come from longer-lived volcanoes that erupted more explosively, and diffusive H loss may have been minimized by rapid ascent rates and lower magmatic temperatures[11]. In the shallow crust, magma degassing can also cause strong fractionation of D/H but should produce a positive correlation with H_2O due to the affinity of D for the vapor phase[25]. Positive trends are not, however, observed in the data, and we conclude that degassing before entrapment did not play a significant role in modifying δD values of the Cascade or Marianas samples.

Initial δD values (corrected as described above) from the Cascade melt inclusions fall in a range from -95 to -70‰, despite a large range in H_2O (Fig. 2.3a). These values are isotopically lighter than those for the Marianas, which range from -55 to -12‰[11] (Fig. 2.3a). Marianas melt inclusions have δD values that are higher than mantle values (-80±10 ‰)[26], and have been interpreted to result from addition of D-enriched fluids to a relatively D-depleted mantle wedge[11]. Other estimates of δD for arc magmas based on phenocrysts (-47 to -25‰ for Kamchatka)[27] and fumarolic gases (-30 ± 10‰ for arcs globally)[28] agree well with the Marianas melt inclusion values. Although the Cascade values overlap with mantle values, a minimum of 67–79% of the H_2O in the Cascade magmas must be sourced from a hydrous subduction component (Fig. 2.2a). We interpret

14

the lighter isotopic values for the Cascades to represent fluids sourced from a plate that

has experienced more dehydration prior to reaching sub-arc depths than in the Marianas.

As the slab becomes progressively more dehydrated, it becomes isotopically lighter as D-

enriched fluids are removed. Thus, fluids released at higher temperatures and greater

extents of slab dehydration should have more negative δD values than fluids that were

removed from the slab at lower temperatures. An alternative possibility is that the

differences in δD between the Cascades and other arcs is the result of large-scale

diffusive fractionation of D and H in the slab, mantle and/or crust during migration of

fluids and melts. Although this cannot be ruled out, it would require that the transport of

H_2O is largely diffusive rather than advective, which is inconsistent with field evidence

for fluid migration through fracture networks (see Supplementary Information A.).

2.4. D/H Fractionation Model

To test the interpretation that differences in δD between the Cascades and

Marianas are due to different extents of slab dehydration, we created a model that

describes D/H fractionation during dehydration reactions in the subducted plate beneath

the two arcs. Using an equilibrium fractionation equation (Supplementary Eq. 1), we

calculated the δD of fluids progressively released from the slab with increasing

temperature and depth. We calculate H_2O released from the slab by coupling a 2-D

thermal model[2] with the thermodynamic calculation code Perple_X [29,30]. We divide the

slab into 1000-m wide vertical columns and calculate the cumulative δD value of fluid

released from each column from the shallowest to the deepest column, assuming that the slab consists of 2 km of basalt, 5 km of gabbro, and 2-4 km of hydrated mantle peridotite (Fig. 2.3b, 2.3c; see Supplementary Fig. A.4 and Information), using temperature and lithologically dependent fractionation factors (Supplementary Fig. A.5). A sedimentary package was excluded from this model because most clay minerals break down at shallow depths (5-10 km; ~250-450°C) and contribute little to the fluid flux at sub-arc depths[6,21].

Model results show that beneath the southern Cascades, the upper portions of the slab, consisting of MORB volcanics and lower crustal gabbros, become completely dehydrated by ~65 km depth (Fig. 2.3b), similar to previous predictions[6]. The hydrated upper mantle portion of the subducted plate is able to carry bound H_2O to greater depths in the form of chlorite, but this phase is predicted to break down when the slab top reaches ~80-90 km depth, which is directly beneath the volcanic arc (Fig. 2.3b). Our model predicts two fluid pulses from the subducted plate: one beneath the forearc from final dehydration of MORB volcanics and gabbros in the crustal part of the slab and another beneath the arc from chlorite breakdown in the upper mantle portion of the slab. The predicted depths of these fluid pulses correlate well with regions of low electrical resistivity and low shear wave velocity in the overlying mantle wedge as imaged by magnetotelluric and seismic data, respectively[31,32].
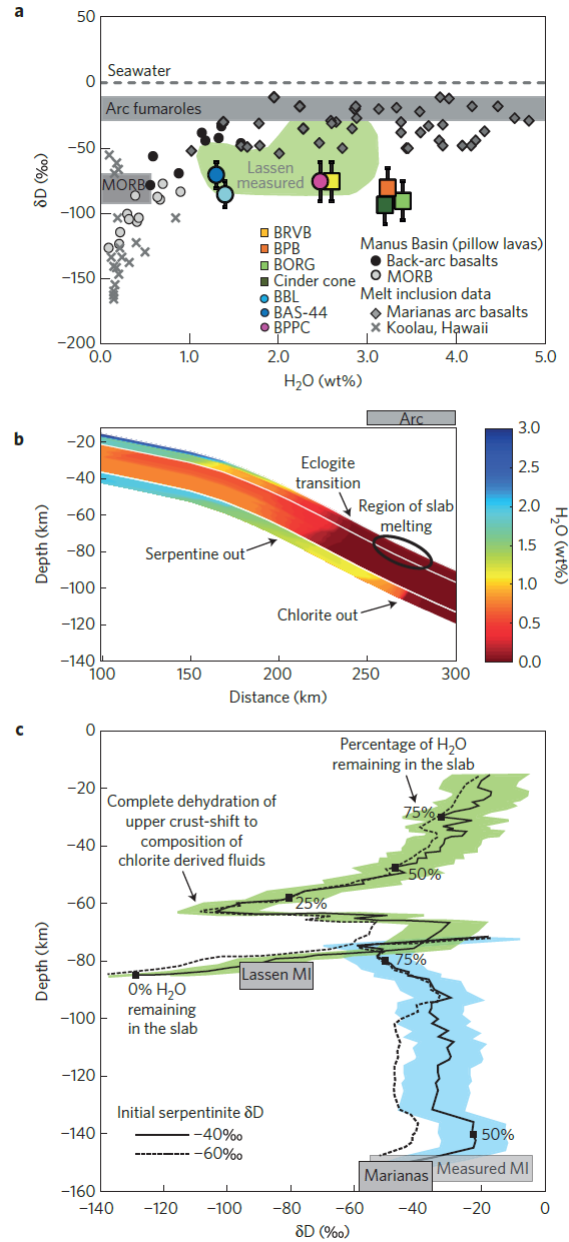
Figure 2.3. Hydrogen isotopes: measured values and model results. a) H_2O versus δD for Lassen (green shaded region excludes inclusions severely affected by H-loss; colored symbols are initial values; errors based on diffusion correction; Table 2.1; Supplementary Information A.), the Marianas Arc[11], Koolau[48], Manus Basin[49], MORB[26] and arc fumaroles[28]. b) Distribution of bound H_2O in the slab calculated with our Lassen thermal model (Supplementary Fig. A.4 and Information). Slab thickness exaggerated x3. c) Fractionation model results. δD of fluids released from the entire slab package as a function of slab top depth beneath the Cascades (green) and Marianas (blue). Uncertainty is ± 15‰ (shaded regions; 2σ; Supplementary Fig. A.4 and Information). Grey boxes show range in melt inclusion data at sub-arc depths.

17

At sub-arc depths beneath the Lassen region, modeled values of δD of the hydrous component released from the slab overlap with corrected melt inclusion values (Fig. 2.3b, 2.3c). This agreement suggests that Cascade arc magmas record the D/H ratio of fluids derived from the deeper interior of the slab. The δD values of antigorite- and chlorite-bearing peridotites, interpreted as subducted slab mantle, from Cerro del Almirez (Spain)[33] agree well with our model predictions (see Supplementary Information A.). In contrast to the Cascades, model results for the Marianas (Fig. 2.3c), where older oceanic crust is being subducted, show that temperatures within the slab remain cool enough to carry bound H_2O in hydrated upper mantle well past sub-arc depths (~160 km). In the Marianas, modeled D/H values for fluids released from the plate overlap with the lowest measured melt inclusion values. Although the modeled values do not reproduce the full range of the data for the Marianas, the model does predict higher δD values for fluids released beneath the Marianas arc compared to the Cascades.

2.5. Evidence and Implications for Slab Melting

Beneath the Lassen region, the upper, completely dehydrated portions of the plate are likely at or above the MORB + H_2O[21] and sediment + H_2O[22] solidi (Fig. 2.2b). Our model results predict that H_2O-rich fluids are released from the slab interior during chlorite breakdown at sub-arc depths, providing H_2O that could cause partial melting of the slab top. Although sediment melting imparts a distinctive trace element signature on many arc magmas worldwide[34], in the Lassen Region it appears to be subordinate to contributions from the subducted basaltic crust[13]. Previous work in the Lassen segment[13,14] found that magmas with the highest $(Sr/P)_N$, and therefore the greatest

18

amount of subduction component, have the lowest Sr isotope ratio ($^{87}Sr/^{86}Sr$ = 0.7029-0.7034), similar to unaltered Gorda Ridge MORB[35] ($^{87}Sr/^{86}Sr$ = 0.7024; Supplementary Fig. A.6). In light of our new results, we interpret the MORB-like $^{87}Sr/^{86}Sr$ signature to reflect hydrous partial melting of Gorda MORB in which altered domains with radiogenic Sr derived from seawater have lost much of their Sr during the shallower stages of dehydration (see Supplementary Information A.). Strong negative correlation of $^{87}Sr/^{86}Sr$ and $(Sr/P)_N$ in the Mt. Shasta region[15] is also consistent with this interpretation, but existing data for other segments of the arc further to the north do not show this pattern[36,37] (Supplementary Fig. A.6).

Our results provide a mechanism for melting of sediments and basalt in the upper part of the subducted oceanic plate by fluids rising from deeper parts of the slab[17,38,39,40]. Because melting of the upper oceanic crust takes place in the garnet stability field, a hallmark of slab melting is the geochemical signature imposed by garnet, such as high Sr/Y and La/Yb. Lavas from the Cascades and other relatively hot-slab subduction zones like Mexico have values of these ratios that are higher than most other arc magmas, but not as extreme as many so-called adakites, which are interpreted to be slab melts[41]. Wet melts of the basaltic crust are expected to be andesitic to dacitic in composition[42,43] and will infiltrate and react with the overlying mantle wedge and lower its solidus temperature as they rise from the plate interface. A comparison of temperature sensitive (H_2O/Ce) and garnet sensitive (La/Yb) parameters for arc magmas worldwide (Supplementary Fig. A.7) lends support to our interpretation that slab melting plays an increasingly important role in arcs where younger, warmer oceanic crust is being subducted.

19

2.6. Bridge

In the preceding chapter (II), the hydrogen isotopes compositions of olivine-hosted melt inclusions from seven cinder cones in the Lassen region were compared with a thermo-petrologic model to investigate slab dehydration and melting beneath the Cascade Arc. The next chapter (III) uses the volatile contents, major and trace elements, and the B isotope compositions of olivine-hosted melt inclusions from eight cinder cones (one in addition to the seven discusses in chapter II) to provide further evidence for the conclusions drawn in chapter II and investigate magma generation processes in the mantle wedge beneath the southern Cascades.

CHAPTER III

SLAB MELTING AND MAGMA FORMATION BENEATH THE

SOUTHERN CASCADE ARC

This chapter includes material co-authored with Dr. P.J. Wallace, Dr. M.A. Clynne, Dr. D. Weis, and Dan Rasmussen. Sample collection was performed by me with the help of Dr. Wallace and Dr. Clynne. All melt inclusions were prepared and analyzed by me using Fourier transform infrared spectroscopy (H_2O and CO_2), electron microprobe (major elements), laser ablation inductively coupled plasma mass Spectrometry (trace elements), and secondary ion mass spectrometry (B isotopes), with assistance from D. Rasmussen for two cinder cones. Analyses, data corrections, geochemical modeling, and interpretation were performed by me, with the help of Dr. Wallace. Radiogenic isotopic analyses on bulk tephra were performed by Dr. Weis. Models of mantle melting, using pMELTS, were performed by me. I drafted all the figures used in this article and the text was written by me, with editorial assistance by Dr. Wallace.

3.1. Introduction

Dehydration of subducted oceanic lithosphere drives arc magmatism at convergent plate margins. However, the thermal structure of an individual subduction zone controls the depths at which key dehydration reactions occur (Schmidt and Poli, 1998; Hacker et al., 2008; Van Keken et al., 2011; Wada et al., 2012), and consequently, affects the composition and sources of fluids and/or melts (e.g., Cooper et al., 2012;

Ruscitto et al, 2012) that infiltrate the mantle wedge to trigger melting. The thermal structure is commonly assessed using the thermal parameter (Φ), which is a function of downgoing plate age, dip angle, and convergence rate (Syracuse et al., 2010, Wada and Wang, 2009). Variability in Φ globally is predicted to cause a wide range of slab surface temperatures beneath arcs (give T range), as estimated from geodynamic models (Syracuse et al, 2010; Wada and Wang, 2009) and geochemical tools (Plank et al., 2009; Cooper et al., 2012). The results suggest a continuum of subduction zones between 'cold' (i.e., Tonga, Kamchatka) and 'warm' slabs (i.e., the Cascades, Mexico). Although fluids released from the subducting slab have been shown to become more solute-rich with increased temperature (Manning, 2004; Kessel et al., 2005a; Herman and Spandler, 2008; Cooper et al, 2012; Ruscitto et al, 2012), whether or not the oceanic crust begins to melt beneath arcs has been debated, despite geochemical evidence for slab melt contributions beneath some warm-slab endmembers such Mexico (e.g., Cai et al., 2014), and the Cascades (Walowski et al., 2015). Isolating the role of different components in the subducted lithosphere (altered oceanic crust, sediments, serpentinized peridotite) and how each component transfers material to the overlying mantle wedge (as fluids, melts or a supercritical phase), is important for our understanding of mass transfer to the mantle, both beneath and beyond arcs, as well as the processes by which the mantle melts in subduction zones.

The Cascade arc represents a global warm-slab endmember due to slow shallow subduction of young oceanic crust (6-10 Ma at the trench; Wilson et al., 2002; Kirby et al., 2002). Estimations from geodynamic models (Syracuse et al., 2010; Wada and Wang, 2009) and geochemical studies (Cooper et al., 2012; Ruscitto et al., 2012; Walowski et

al., 2015) agree that slab surface temperatures beneath the arc axis are hotter, on average, than many other arcs globally. Previous work in the central Cascades has suggested that the mantle wedge beneath the arc receives a reduced flux of volatiles from the downgoing slab (Ruscitto et al., 2012), and H_2O concentrations in olivine-hosted melt inclusions from both the central and southern Cascades (~3.2 wt%; Ruscitto et al., 2010, 2011, LeVoyer et al., 2010) fall slightly below the global average (~3.9 wt%; Plank et al., 2013). Walowski et al. (2015) found that hydrogen isotope ratios of primitive magmas from the Lassen region of the southern Cascades are lighter than those for the Marianas. This was demonstrated to reflect waning dehydration of the deep slab interior (hydrated mantle) after the crustal portion of the slab had already dehydrated beneath the forearc. These results also provide evidence that flux-melting of the oceanic crust occurs when the fluids released from the slab interior interact with oceanic crust that is above its wet solidus temperature (i.e., Skora and Blundy, 2010; Till et al., 2012; Spandler and Pirard, 2013).

We measured the volatile contents, major element, trace element, and B isotope compositions of olivine-hosted melt inclusions and the radiogenic isotopic compositions of bulk tephra from the same eruptive centers in the Lassen region that were studied by Walowski et al. (2015) for H isotopes. With these near-primary mantle melts, we aim to quantify the chemical contributions from the subducting oceanic lithosphere to better understand how subduction of warm oceanic crust affects the composition of mantle melts and the productivity of melting in the mantle wedge. Lastly, we test the hypothesis presented by Walowski et al. (2015) that magma production beneath the southern

23

Cascade Arc involves a multi-stage process that includes flux melting of the subducted oceanic crust and hydrous slab melt addition to the overlying mantle wedge.

3.2. Geologic Setting

The Lassen Segment is the southern terminus of the active Cascade arc (Guffanti and Weaver, 1988). Volcanism is the result of oblique subduction of the Gorda micro-plate beneath the North American plate (Fig. 3.1; Wilson, 2002), producing dominantly calc-alkaline magmas (Clynne and Muffler, 2010). Westward expansion of the Basin and Range extensional province into the eastern flanks of the Cascade Arc, including the Hat Creek and Lake Almanor Grabens, has produced many normal faults that provide pathways for mafic magmas to reach the surface (Guffanti et al., 1990; Clynne and Muffler, 2010). The Quaternary volcanics in the Lassen region sit above a broad platform of mafic to intermediate volcanoes and volcanic products 2-4 km thick (Berge and Stauber, 1987). This volcanic platform is underlain by plutonic Sierran and metamorphic Klamath terrain basement rocks as suggested by constant modeled seismic velocities across the Sierra Nevada-Cascade Range boundary (Berge and Stauber, 1987).

Surrounding the volcanic center of Lassen Peak, a dacitic dome complex (Clynne and Muffler, 2010), is a large volcanic field containing over 500 monogenetic cinder cones and small shield volcanoes erupted in the last 12 Ma (Guffanti et al., 1990). Previous work on these mafic cinder cones has identified a range in compositions from low-K tholeiitic basalts to calc-alkaline basalts, basaltic andesites, and andesites (Clynne, 1993; Borg et al., 1997). Also observed in the most primitive calc-alkaline volcanic rocks is distinct across-arc geochemical variability interpreted to be caused by variable
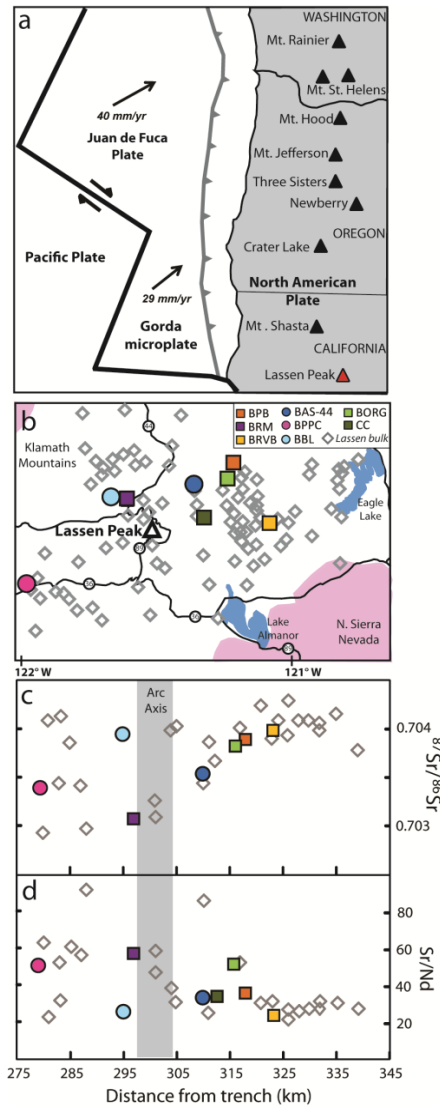
Figure 3.1. Sample locations and across-arc geochemical variability. a) Regional map of the Northwestern United States showing major tectonic boundaries. The Cascade volcanic arc is defined by the major peaked labeled with black triangles. Lassen Peak is highlighted in red. Black arrows show direction and are labeled with the convergence rate relative to North America (Wilson et al., 2002). b) Larger scale map of the Lassen region with locations of vents sampled in this study (BRVB: Basalt of Round Valley Butte, BPB: Basalt of Poison Butte, BRM: Basalt of Red Mountain, BBL: Basalt of Big Lake, BAS-44: Basalt of Hwy 44, BPPC: Basalt of Paine Parasitic Cone, BORG: Basalt of Old Railroad Grade, and CC: Cinder Cone; see Table 3.1 for details) and previously sampled by Clynne (1993) and Borg (1995; grey diamonds). Lassen Peak (large white triangle), outcropping basement rocks (shaded pink areas), major highways (thin black lines), and large lakes (shaded blue regions), are also highlighted. c) Distance from the trench vs. Sr/Nd and d) 87Sr/86Sr for samples in this study(colored symbols) and Borg et al. (1997; grey diamonds). Symbols and colors for individual cinder cones are consistent throughout the manuscript.

enrichment of the mantle by a subduction component, a key factor for targeting this

region in our study (Fig. 3.1; Borg 1997, 2002). Figure 3.1 shows variations in both

Sr/Nd and ^{87}Sr/^{86}Sr with increasing distance from the trench. Decreasing Sr/Nd has been

interpreted to indicate the waning addition of a subduction component towards the back-

arc (Borg et al., 1997). The ^{87}Sr/^{86}Sr compositions, however, increase toward the back-

arc, indicating that the subduction component has a less radiogenic Sr isotope signature

than the sub-arc mantle. Furthermore, variability in Nb/Zr suggests that the Lassen sub-

arc mantle is heterogeneous (Borg et al., 1997; Walowski et al., 2015), but there are no

systematic variations of Nb/Zr with distance from the trench.

3.3. Sample Descriptions and Analytical Methods

Samples were collected from the tephra deposits of Quaternary monogenetic vents

spanning ~80 km from the forearc to the backarc (Fig. 3.1). Vents that erupted primitive

basalt or basaltic andesite (MgO > 7 wt%) identified from bulk rock analyses (Clynne,

1993; Borg et al., 1997) were targeted because they are close to primary mantle melts in

composition. Coarse ash was collected because it quenches more rapidly than lava,

bombs, and lapilli, minimizing the potential for syn-eruptive diffusive H loss or

crystallization of melt inclusions (e.g., Lloyd, 2013). Loose olivine crystals (50 μm to 1

mm in size) were hand-picked from washed and sieved tephra. The olivine crystals were

treated in HBF_4 to remove glass adhering to the crystal surface and examined in

immersion oil (refractive index 1.675) to locate melt inclusions. Olivine crystals hosting

fully enclosed, glassy melt inclusions were mounted in acetone-soluble resin on glass

slides and prepared as doubly polished wafers. H_2O and CO_2 concentrations of the melt

inclusions were measured at the University of Oregon using a Thermo-Nicolet Nexus 670 FTIR spectrometer interfaced with a Continuum IR microscope. Concentrations were calculated from IR peak absorbances using the Beer–Lambert law and compositionally appropriate absorption coefficients (see Johnson et al., 2008, for details). Melt inclusions and host olivine were analyzed for major elements (plus S and Cl for inclusions) on the Cameca SX-100 electron microprobe at the University of Oregon (see Ruscitto et al., 2010, for details). Melt inclusions were subsequently analyzed for a suite of trace elements on the Photon Machines Analyte G2 193 nm ArF ''fast''Excimer Laser system at Oregon State University, using 50 µm spot size with a 5 Hz pulse rate. Measured trace element concentrations were determined by reference to GSE-1G glass as a calibration standard and using ^{43}Ca as an internal standard (see Loewen and Kent, 2012, for details). BHVO-2G, BCR-2G, and GSD-1G glasses were also analyzed to monitor accuracy and precision, and the analyzed values were within 10% of accepted values.

A subset of the melt inclusions that were analyzed for H isotopes and trace elements by Walowski et al. (2015) were also analyzed for B isotope ratios using the Cameca IMS 1280 at the Northeastern National Ion Microprobe Facility, Woods Hole Oceanographic Institution, with O- primary beam, 20-40 nA primary current, 10,000 V secondary voltage, and a 10 µm spot size. More detailed methods are described in Marschall and Monteleone (2014). Some of the melt inclusions were too small to allow a new SIMS spot adjacent to an existing NanoSIMS spot (20x20 rastered area, ~5 µm deep). In these cases, the SIMS spot was placed within the pre-existing NanoSIMS spot. Tests comparing measurements within pre-existing spots to those on a clean surface from a single melt inclusion revealed no systematic differences.

Sr, Nd, Hf, and Pb isotope ratios were measured at the Pacific Centre for Isotopic and Geochemical Research at the University of British Columbia. Pb, Nd, and Hf isotope ratios were measured by MC-ICP-MS (Nu Instruments Ltd., Nu II 214), and Sr isotope ratios were measured by Thermo Finnigan Triton TIMS using procedures described in Weis et al. (2007) and Weis et al. (2006). Additional details regarding sample preparation and analytical techniques are given by Mullen and Weis (2015). Tephra from sample CC was excluded from isotopic analyses due to clear crustal contamination (abundant quartz xenocrysts) of the bulk material.

3.4. Results

3.4.1. Melt Inclusion Major and Trace Element Compositions

The olivine host crystals vary from Fo_{84} to Fo_{90} (Table 3.1). For each cinder cone, 11-17 melt inclusions were analyzed and individually corrected for post-entrapment crystallization (PEC) and Fe-loss using Petrolog 3.1 (Danyushevsky and Plechov, 2011; Danyushevsky, 2000). Volatile contents and trace elements, which are not included in the Petrolog calculations, were also corrected using the ratios of K_2O in corrected and uncorrected inclusions. Initial Fe contents were based on the FeO^T of the bulk tephra or individual melt inclusions with the highest MgO and FeO^T at a single cone (bulk tephra compositions were not available for cones BBL and CC). Calculated percentages of PEC for all melt inclusions range from 0 - 14%. Corrected melt inclusion compositions overlap with the most primitive lava samples previously analyzed in the Lassen region (Fig. 3.2) and contain MgO concentrations of 7.4 - 9.8 wt%

Table 3.1. Averaged Primary Melt Compositions.

Sample	BBL-05	BORG-1	BPB-1	BAS-44-02	BPPC-01	BRVB-01	CC-1	BRM-1	
Lat (N)	40°34'33.72"	40°39'15.63"	40°40'40.80"	40°37'50.64"	40°19'34.22"	40°31'48.78"	40°32'24.50"	40°34'13.17"	
Long (W)	121°37'1.32"	121°13'29.07"	121°12'51.00"	121°20'40.14"	121°54'38.64"	121° 4'34.32"	121°18'37.00"	121°35'31.59"	
Distance (km)	295	316	318	310	279	323	312	297	
	n = # of inclusions								
(wt%)	n = 11	n = 15	n = 16	n = 17	n = 14	n = 14	n = 13	n = 15	1 s.e.
SiO_2	48.94	49.95	51.52	49.42	51.16	48.96	52.54	49.85	0.28
Al_2O_3	14.72	16.14	15.98	16.23	15.69	13.98	17.15	16.25	0.19
FeO^1	9.10	8.18	7.23	8.22	7.38	9.24	5.93	8.06	0.10
MgO	14.01	12.40	11.00	11.50	11.18	14.30	8.85	12.41	0.19
CaO	8.82	9.33	9.53	10.28	10.51	7.96	10.31	8.12	0.10
Na_2O	2.72	2.50	2.67	2.68	2.60	2.91	3.15	3.40	0.12
K_2O	0.36	0.47	0.78	0.28	0.30	0.93	0.85	0.68	0.02
TiO_2	0.92	0.70	0.84	0.93	0.76	1.22	0.86	0.77	0.03
MnO	0.12	0.10	0.11	0.12	0.12	0.11	0.09	0.09	0.012
P_2O_5	0.16	0.09	0.23	0.15	0.18	0.27	0.16	0.26	0.007
S	0.09	0.11	0.09	0.11	0.11	0.13	0.09	0.16	0.003
Cl	0.02	0.05	0.05	0.03	0.04	0.04	0.04	0.20	0.002
CO_{2max} (ppm)	884	1384	1436	754	1209	622	1436	521	50
H_2O_{max}	1.29	3.02	2.94	1.21	2.29	2.28	3.45	2.58	0.20
% Ol	16.90	7.90	8.80	4.00	7.50	20.10	1.00	14.8	
(ppm)									
Li	7.17	6.97	7.36	5.39	6.23	11.45	10.44	7.27	1.83
B	1.77	3.72	8.25	2.59	3.00	8.00	5.29	3.18	2.34
Sc	37.91	38.46	34.22	40.72	35.02	32.31	27.09	22.99	1.97
V	225.08	276.51	204.98	217.83	210.28	252.36	185.95	192.96	14.96
Rb	5.49	5.44	14.24	4.79	5.07	21.56	15.39	10.43	0.84
Sr	270.41	438.31	475.59	407.95	449.60	454.29	342.48	1196.94	8.97
Y	21.20	12.63	15.83	18.63	15.69	18.28	13.13	11.37	1.38
Zr	79.34	52.21	92.80	77.53	58.75	104.58	70.89	89.80	6.40
Nb	2.99	2.06	5.56	2.71	1.42	6.99	4.03	5.22	0.60
Ba	156.99	141.35	295.54	116.72	108.81	378.27	202.53	277.05	6.95
La	6.24	5.60	11.26	7.43	5.60	14.15	7.46	15.04	0.41
Ce	15.89	12.76	24.03	19.65	13.00	34.87	16.92	35.50	0.91
Pr	2.20	1.70	3.30	2.68	1.80	4.37	2.31	4.36	0.29
Nd	10.80	8.25	13.67	12.38	8.73	19.66	10.52	18.77	0.64
Sm	2.77	2.24	3.12	2.91	2.23	4.25	2.41	3.30	0.37
Eu	1.04	0.84	1.05	1.01	0.85	1.35	0.80	1.12	0.27
Gd	3.50	2.43	3.13	3.19	2.77	3.96	2.47	2.86	0.35
Dy	3.80	2.43	2.88	3.01	2.67	3.66	2.55	2.11	0.47
Er	2.51	1.40	1.80	2.21	1.81	1.97	1.39	1.24	0.34
Yb	2.47	1.37	1.73	2.11	1.73	1.92	1.39	1.27	0.29
Hf	1.78	1.35	2.22	1.99	1.71	2.54	1.73	2.33	0.24
Ta	0.17	0.11	0.34	0.15	0.08	0.35	0.26	0.23	0.04
Pb	1.85	2.26	4.01	1.54	1.62	4.14	3.22	4.81	0.56
Th	0.52	0.58	1.75	0.59	0.54	1.77	1.63	1.68	0.10
U	0.18	0.29	0.49	0.21	0.18	0.61	0.52	0.49	0.04
$^{87}Sr/^{86}Sr$	0.70394	0.70381	0.70388	0.70353	0.70340	0.70399	N/A	0.70308	
$^{208}Pb/^{204}Pb$	38.65026	38.53864	38.61236	38.56385	38.46401	38.64561	N/A	38.562	
$^{177}Hf/^{176}Hf$	0.28306	0.28306	0.28306	0.28309	0.28305	0.28303	N/A	N/A	
$^{143}Nd/^{144}Nd$	0.51286	0.51286	0.51283	0.51295	0.51293	0.51283	N/A	0.512901	
$\delta^{11}B$ ‰ (2SE)	-4.24(6.30)	-2.64(3.58)	-5.09(3.98)	-4.53(6.10)	-4.95(3.89)	-4.97(2.47)	-9.89(2.55)	-2.38(3.42)	
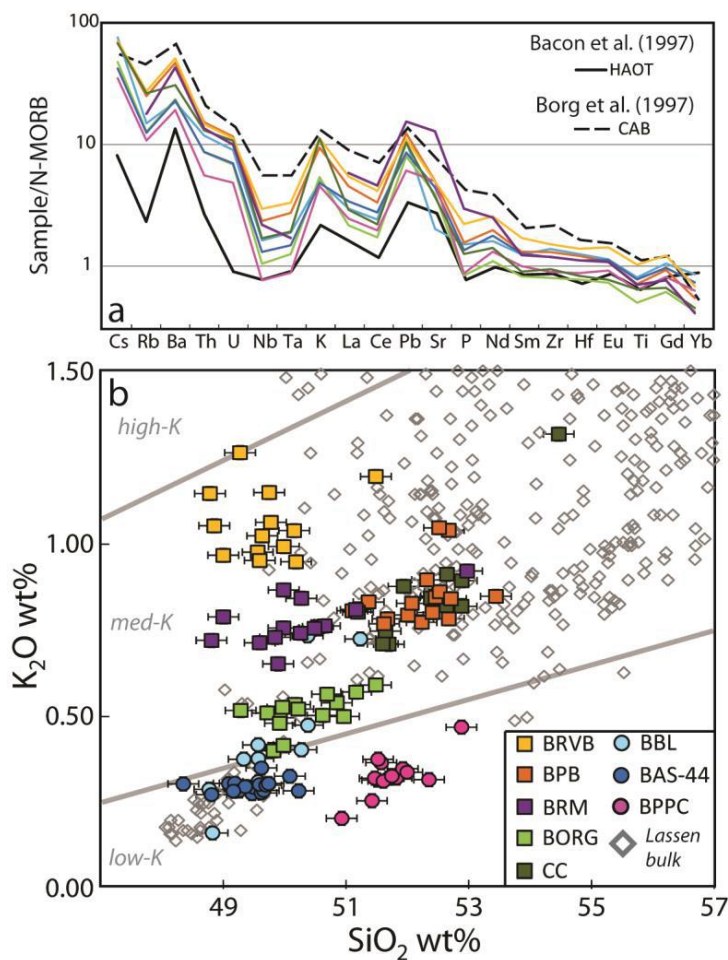
Figure 3.2. Corrected melt inclusion major and trace element compositions. a) Average melt inclusion trace element composition for each vent normalized to normal-MORB (N-MORB; Sun and McDonough, 1989) and compared with previously determined end-member compositions (CAB, Borg et al. 1997; HAOT, Bacon et al. 1997). b) K_2O and SiO_2 contents of individual melt inclusions (corrected, volatile-free normalized values) compared with bulk rock analyses from Clynne, (1993; grey diamonds). Classification of low-, med-, and high-K based on Peccerillo and Taylor (1976).

(Supplementary Table B.1; see Apendix B for all supplementary information for this

chapter). To estimate a primary melt composition for each cone, we incrementally added

equilibrium olivine (0.1 wt% steps) to the average melt inclusion composition from each

cone until the melt composition was in equilibrium with mantle olivine (Fo$_{90}$; Table 3.1;

Ruscitto et al., 2010). The calculated primary melt compositions required addition of 1-20% equilibrium olivine (Table 3.1).

The melt inclusion glasses are dominantly medium-K calc-alkaline basalt (CAB), with some that fall into the low-K field (Fig. 3.2a). Previous work in the Lassen region has suggested that low-K tholeiitic magmas (also called high-alumina olivine tholeiites; HAOT) and calc-alkaline magmas have fundamentally different source regions (Clynne, 1993; Bacon et al., 1997; Baker et al., 1994). However, the low-K samples used in this study do not display the lower LREE/HREE and LILE/HFSE values typical of the endmember HAOT volcanic rocks in this region (Fig. 3.2, Bacon et al., 1997). Rather, all compositions used in this study display similar trace element patterns to the regional CABs (Fig. 3.2), suggesting that despite variability in major and trace element compositions, they likely formed as the result of flux-melting, and not decompression melting of the mantle.

3.4.2. Magmatic Volatile Contents

Dissolved H_2O contents of the melt inclusions range from 0.6-3.5 wt%. At individual cinder cones, a range in H_2O concentrations is observed and is likely due to differences in extent of pre-entrapment degassing (Metrich and Wallace 2008; Johnson et al., 2009) and post-entrapment hydrogen loss (Lloyd et al., 2013, Gaetani et al., 2012, Bucholz et al., 2013). Because these processes systematically decrease H_2O concentrations, the maximum measured H_2O/K_2O ratio for each cone was used to estimate the initial H_2O content (H_2O_{max}) of the magma erupted at that cone. In the Lassen region, H_2O_{max} ranges from 1.3-3.4 wt%. Primary melt H_2O concentrations (1.1-

3.4 wt%, calculated from H_2O_{max} using the olivine addition method described above; Table 3.1) overlap with calculated primary melt H_2O values for basaltic and basaltic andesite melt inclusions from central Oregon (1.4-3.0 wt%; Ruscitto et al., 2010). In contrast to H_2O, Cl is not affected by degassing and post-entrapment diffusive effects. Concentrations of Cl in calculated primary melts range from 100-600 ppm, except at BRM, where Cl values are as high as 2500 ppm (Supplementary Table B1).

3.4.3. Isotopic Compositions

The $\delta^{11}B$ values from individual cinder cones in the Lassen region range from -9.9‰ to -2.4‰ (Table 3.1; Fig. 3.3). These values overlap with those measured for bulk rock samples from the southern Washington Cascades, which range from -9‰ to -0.4‰ (Leeman et al., 2004), and those from melt inclusions from Mt. Shasta (Fig. 3.3; Rose et al., 2001; LeVoyer et al., 2010). Melt inclusions from the Cascades have lower B concentrations and more negative $\delta^{11}B$ than those measured in other arcs, such as Kamchatka and Japan, where older oceanic crust subducts (Fig. 3.3; Ishikawa et al., 2001; Ishikawa and Tera, 1999).

The Sr, Nd, Hf, and Pb isotope measurements for bulk tephra samples overlap with those previously determined for volcanic rocks in the Lassen Region (Borg et al., 1997; Borg et al., 2002) and show variability in $^{87}Sr/^{86}Sr$ (0.703396-0.703985±0.000007), $^{208}Pb/^{204}Pb$ (38.4640-38.6503±0.0026), $^{177}Hf/^{176}Hf$ (0.283035-0.283094±0.000006), and $^{143}Nd/^{144}Nd$ (0.512827-0.512948±0.000006) (Table 3.1).
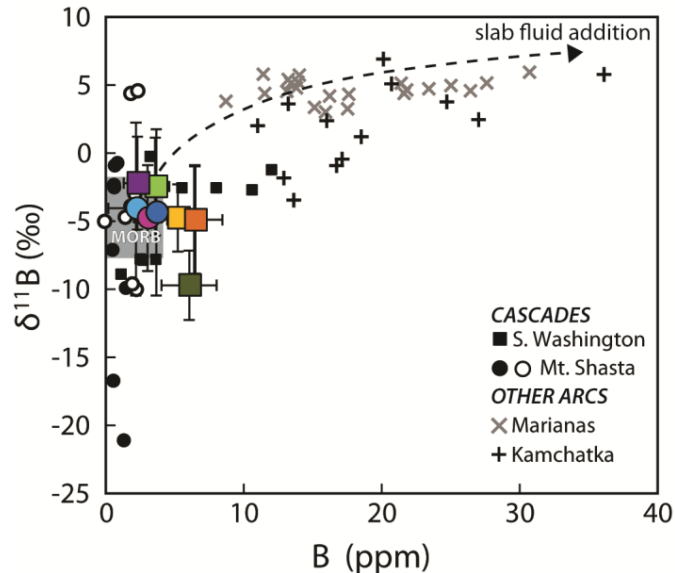
Figure 3.3. Boron isotope compositions. Each data point (symbols as in Fig. 3.1) represents an average from 4-6 individual melt inclusion analyses. Data for comparison from the southern Washington Cascades (Leeman et al., 2004; filled squares, whole rock analyses) Mt. Shasta (Rose et al., 2001, open circles; individual melt inclusions; LeVoyer et al., 2010, filled circles), the Marianas (Ishikawa, 2001), and Kamchatka (Ishikawa and Tera, 1999). Dashed black curve represent mixing between MORB (Chaussidon and Jambon, 1993) and a hydrous slab fluid (Marschall, 2007).

3.5. Discussion

3.5.1. The Source of Volatiles in Lassen Region Primitive Magmas

B is a highly fluid mobile element, and because it is found in higher concentrations in subducted materials than the mantle, it can be an excellent tracer of fluids derived from subducting slabs (e.g., Bebout et a.,1993, Ryan and Langmuir 1993, Tonarini et al., 2001). In addition, subducted materials such as sediment, oceanic crust, and serpentinitized mantle have $\delta^{11}B$ signatures that are distinct from the mantle wedge (e.g., Ishikawa and Nakamura, 1993; Smith et al., 1995; Boschi et al., 2008; Chaussidon and Jambon, 1994). However, the B isotopic composition and low B concentrations in the

33

melt inclusions from the Lassen region suggest that the sub-arc mantle receives little to no B from the subducting slab (Fig. 3.3). This is probably the result of extensive dehydration of the slab before it reaches sub-arc depths (Leeman et al., 2004; Manea et al., 2014). Geodynamic modeling and calculated metamorphic phase equilibria suggest that H_2O can be carried to sub-arc depths by the hydrated mantle portion of the downgoing slab, in the form of chlorite, beneath the Lassen region (van Keken et al., 2011; Walowski et al., 2015). The D/H ratios measured in melt inclusions from the Lassen region are in agreement with modeled values which indicate that fluids are likely sourced from the final breakdown of chlorite in the deep slab interior (Walowski et al., 2015). Because nearly all B is released from hydrated peridotite during the antigorite breakdown reaction (which occurs in the slab beneath the Cascades before reaching sub-arc depths), chlorite-derived fluids contribute little to no B to the subduction component (Spandler et al., 2014). This explains how the slab beneath the Cascades can release a hydrous slab component to the mantle wedge that contains very little B, such that primitive magmas formed in the wedge have B isotope ratios and concentrations typical of mantle-derived magmas (MORB).

Despite low B concentrations, H_2O and Cl are high compared to MORB, which requires that these volatiles are retained in the slab to greater depths than B (Spandler et al., 2014). Furthermore, strong correlations of H_2O_{max}/Ce and Cl/Nb with Sr/Nd clearly demonstrate that volatile and trace element enrichments are coupled and therefore are derived from the same process (Fig. 3.4). To better quantify this relationship, we calculated partial melt compositions for two mantle endmembers to which variable amounts of subduction component were added. Figure 3.4 shows good agreement

between the model curves and the melt inclusion data, which indicates that volatile and trace element variability at different cones is the result of different amounts of a subduction component added to a heterogeneous mantle wedge. However, in some cases, such as BRM, a sample will have a lower H_2O/Ce for a given value of Sr/Nd than predicted by the melting model. This may be caused by variability in the H_2O and trace element ratios of the hydrous subduction component, or it may suggest that at some cones, H_2O_{max} is still a partly degassed composition (either because of pre-entrapment degassing or post-entrapment H loss). Cl/Nb should provide a more robust indication of initial volatile concentration because Cl is not affected by diffusive loss and only degasses at very low pressure. Good agreement between the data and melting models for Cl/Nb vs. Sr/Nd provides support for the interpretation that initial H_2O concentrations are related to the amount of a subduction component added to the mantle wedge beneath the arc and that the slab component has ratios of H_2O and Cl to LILE that are not highly variable (Fig. 3.4b and c). This evidence indicates that BRM, the sample with the highest Sr/Nd and therefore largest amount of a subduction component, has very low H_2O/Ce as the result of extensive degassing in the crust or post-entrapment hydrogen diffusive loss.

Volatile and trace element ratios from the central Oregon Cascades can also be explained using the calculated melting curves, but require subduction component addition to a more enriched mantle source than most Lassen region magmas (Fig. 3.4a; Ruscitto et al., 2010). Interestingly, melt inclusions with the highest values of Sr/Nd in both the Lassen region (BRM) and the Mt. Shasta region do not have the highest values of H_2O/Ce, but they do have the highest Cl/Nb, and also have Cl concentrations significantly higher than other cones throughout the Cascades. As suggested above, these

magmas likely experienced extensive degassing of H_2O in the crust before melt inclusion

entrapment, and/or were affected by post-entrapment H loss. However, if the BRM and

Mt. Shasta magmas had pre-degassing compositions that fit the model curves in Figure

3.4a, they would have initially had up to ~8-10 wt% H_2O. This is consistent with

experimental phase equilibria showing that high-Mg basaltic andesites and andesites at

Mt. Shasta had very high initial H_2O contents (10-14 wt%; Krawczynski et al., 2012).

Such high initial H_2O is also consistent with the very high Cl/Nb values for high-Mg

basalts and basaltic andesites at Mt. Shasta (Ruscitto et al., 2011).
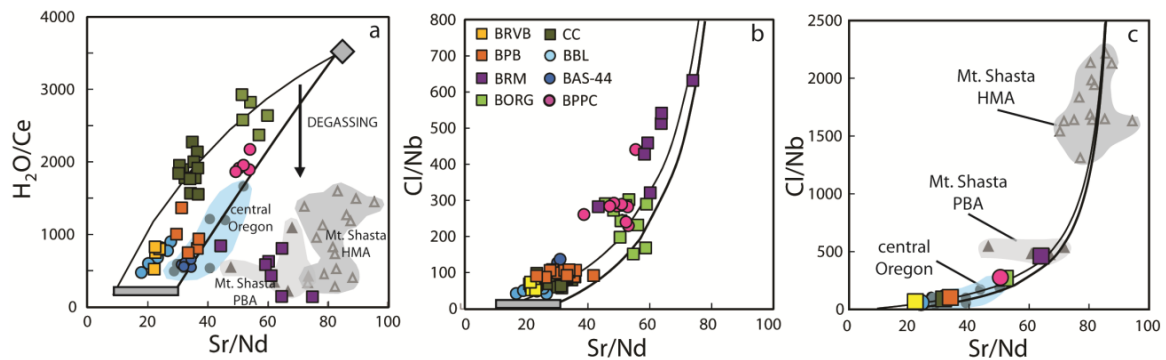
Figure 3.4. Corrected melt inclusion volatile and trace element ratios. a) H_2O/Ce vs. Sr/Nd (corrected melt inclusions that contain H_2O concentrations within 0.5 wt% of the H_2O_{max} from each cone to represent the least degassed compositions), b) Cl/Nb vs. Sr/Nd (all melt inclusions; corrected) and c) Cl/Nb vs. Sr/Nd (y-axis extents to higher values, average values calculated using corrected melt inclusions from each cone). Data from central Oregon (Ruscitto et al., 2010; restored melt inclusions; solid blue circles enclosed in light blue shaded field) and Mt. Shasta (Ruscitto et al., 2008; restored melt inclusions; primitive basaltic andesite (PBA): solid grey triangles enclosed in grey shaded field; high-Mg andesites (HMA): open grey triangles enclosed in a grey shaded field), for comparison. Black lines represent 10% partial melts of two endmember mantle compositions (DMM; Workman and Hart, 2005; average central Oregon mantle; Ruscitto et al., 2010) mixed with variable amounts of a hydrous subduction component (grey diamond; calculated using methods of Portnyagin et al. (2007), with primary mantle composition of BORG; Table 3.1). Grey bar represents the range in sub-arc mantle compositions determined by Walowski et al. (2015). Melt inclusions that have experienced degassing or syn-eruptive H loss will cause deviation from the melting curves as indicated by the black arrow in panel (a).

The Blanco Fracture zone, which separates the Juan de Fuca and Gorda plates, may provide a pathway for deep serpentinization of the upper mantle in the downgoing slab offshore of the Cascades, and has been proposed to source the volatile-rich component at Mt. Shasta (Grove et al., 2002; Manea et al., 2014) However, plate reconstructions and symmetry of the fracture zone on the Pacific plate suggest that the Blanco Fracture zone is not old enough to project beneath the arc (Wilson, 2002), and thus, the causes of the geochemical differences between the Mt. Shasta and Lassen regions (Fig. 3.4) remain enigmatic.

3.5.2. Evidence for Slab Melting

Previous work using trace elements and radiogenic isotopes in the Lassen region found negative correlations between LILE/LREE ratios and $^{87}Sr/^{86}Sr$, which suggests that the subduction component is less radiogenic than the sub-arc mantle (Borg et al., 1997, 2002). New radiogenic isotope data from this study overlap with the published data (Fig. 3.5). Because elevated H_2O/Ce, Cl/Nb, and Sr/Nd ratios are related to subduction component addition, our data confirm that the subduction component is MORB-like, with less radiogenic Sr and Pb isotopic composition and more radiogenic Nd isotope composition than the Lassen region sub-arc mantle. In its isotopic characteristics, the subduction component beneath the Lassen region is similar to offshore Gorda Ridge MORB (Davis et al., 2008). However, a major contribution from the melting of subducted MORB crust was originally discounted because dry eclogitized oceanic lithosphere requires higher temperatures than expected for the slab top at sub-arc depths (Borg et al., 1997). Similar isotopic and trace element relationships are observed in the

Mt. Shasta region (Fig. 3.5). Grove et al. (2002) discounted slab melting beneath Shasta as a possible explanation because models of hydrous peridotite melting could reproduce the observed major element compositions of primitive volcanic rocks in that region. Recent work by Walowski et al. (2015) interpreted the light D/H values of melt inclusions from the Lassen region as resulting from final dehydration of chlorite in the hydrated upper mantle portion of the downgoing slab. This provides a mechanism to deliver H_2O to the MORB-volcanic portion of the slab top and drive wet slab melting beneath the arc.

To further test this hypothesis, we calculated mixing and partial melting models involving the Lassen sub-arc mantle and a partial melt of Gorda Ridge MORB (Fig. 3.5). Because temperatures of the plate top are at or above the wet MORB and wet sediment solidi (Schmidt and Poli, 1998; Herman and Spandler, 2008), we assume the subduction components are partial melts rather than aqueous fluids (Cooper et al., 2012; Ruscitto et al., 2012; Walowski et al., 2015). We also assume that the Gorda MORB component is unaltered. This assumption relies on the fact that oceanic crust is heterogeneously altered during hydrothermal alteration (e.g., Bach, 2003), and that the unaltered portions retain their MORB-like signature, whereas altered zones likely lose most of their seawater-enriched Sr beneath the forearc during transition to ecologite (Walowski et al., 2015). Because Sr/Nd is an indicator of subduction enrichment, primitive basalts and basaltic andesite with the lowest Sr/Nd values should be most representative of the Lassen sub-arc mantle. For the samples with the lowest Sr/Nd, a small range of Sr, Nd, and Pb isotope ratios are observed, and these ranges are probably indicative of mantle heterogeneity beneath the arc, as previous suggested by Borg et al. (1997; 2002) and
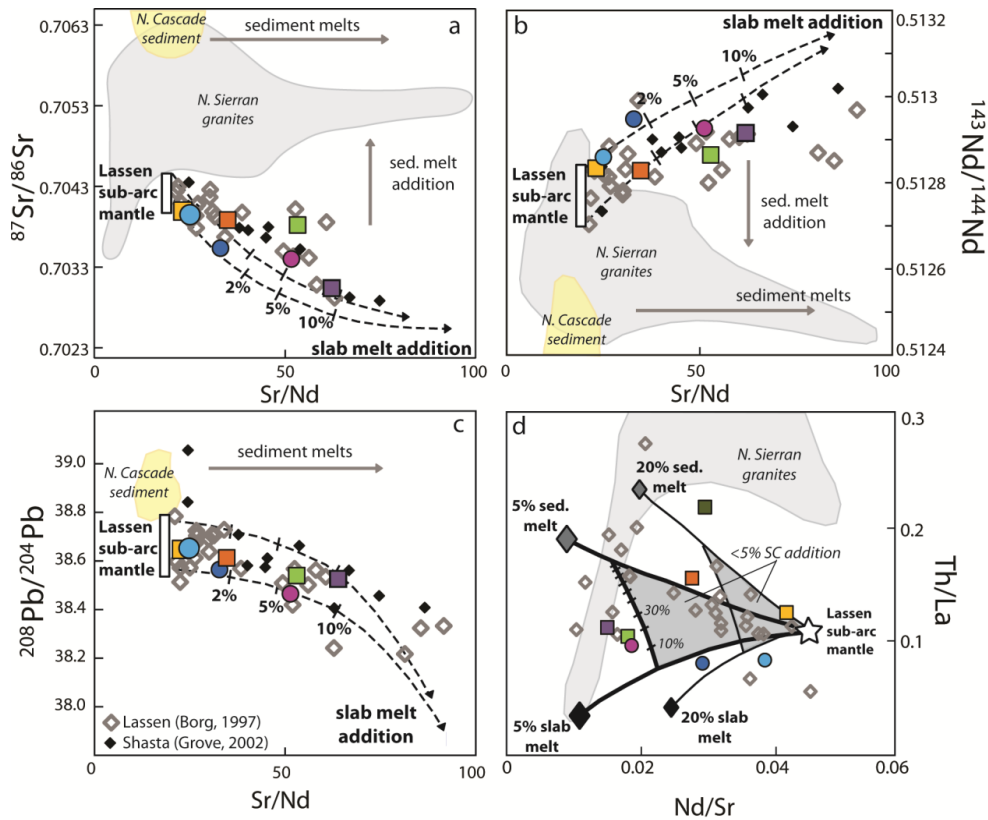
Figure 3.5. Radiogenic isotope compositions and slab melt mixing models. a) Bulk tephra compositions of a) ^{87}Sr/^{86}Sr b) ^{208}Pb/^{204}Pb, and c) ^{143}Nd/^{144}Nd vs. average Sr/Nd from melt inclusions for each cone (symbols as in Figure 3.4). Isotopic composition of BRM is from Borg et al. (1997), as it was not analyzed in this study. CC was omitted due to evidence for crustal contamination (see main text). Bulk lava analyses from the Lassen Region and M. Shasta (Borg et al., 1997; Grove et al., 2002, respectively) for comparison. North Cascade sediment (yellow shaded region; Carpentier et al., 2013, 2014) and northern Sierran granites (grey shaded region; Cecil et al., 2012) highlighted to show possible components that may contribute to trace element and radiogenic isotope variability of samples. Melting models (dashed lines) calculated using the batch melting equation for a range in mantle sources (calculated for the Lassen sub-arc mantle; see text) mixed with 2, 5, and 10% (labeled on modeled curves) of a 5% partial melt of Gorda MORB (Davis et al., 2008; partition coefficients from Kessel et al., 2005a; at 4 GPa, 1000°C). Bulk partition coefficients calculated for a spinel peridotite assemblage 35/30/12/5-Ol/OPX/CPX/Sp (Hughes and Taylor, 1986) using mineral partition coefficients of Eiler et al. (2005) for Sr and Nd. Melt fractions derived from PMELTS model results (for a given temperature and amount of slab melt addition; Fig. 3.6). d) Lassen sub-arc mantle (based on bulk rock sample with smallest amount of apparent subduction component) mixed with sediment partial melts (5%, large filled grey diamond, and 20%, large filled grey diamond, melts of N. Cascade sediment using partition coefficients from Kessel et al. (2005) a) and slab partial melts 5%, large filled black diamond, and 20%, large filled black diamond, melts of Gorda MORB using partition coefficients from Kessel et al. (2005a).

39

Clynne and Borg (1997). We thus use a range in sub-arc mantle compositions (Fig. 3.5; $^{87}Sr/^{86}Sr = 0.7039 - 0.7043$, $^{208}Pb/^{204}Pb = 38.512 - 38.782$, and $^{143}Nd/^{144}Nd = 0.5127-0.5128$). Figure 3.5 shows curves that represent mantle melts formed by melting of the sub-arc mantle mixed with variable amounts of Gorda MORB melt. The model results suggests 1-10 wt% addition of a subduction component that is a slab melt. Although the model results can explain a majority of the compositions, they under-predict some values of Sr and Pb isotopes, and overpredict the range in Nd isotopes. There are three potential explanations for these small offsets: 1) zones of alteration in the MORB volcanic section of the downgoing plate that retained their isotopic signature even after complete dehydration beneath the forearc, 2) involvement of small proportions of a sediment melt component, and/or 3) contamination by continental crust. All three components may play a role in causing the slight offset of the slab melt models from the Lassen data seen in Figure 3.5. The latter two explanations will be discussed in further detail in the following section.

Our proposed mechanism for slab melting relies on breakdown of chlorite in the mantle portion of the downgoing oceanic plate. However, in the model shown in Figure 3.5, this component has been neglected in our melting calculations. Fluids produced from the breakdown of chlorite at sub-arc depths have some distinct trace element characteristics (e.g., elevated LREE/HREE), but overall, are solute poor (Spandler et al., 2014), and as a result, will have little effect on the trace element composition of the resulting magmas formed by flux melting of the upper oceanic crust. For example, Sr concentrations in fluids produced from the breakdown of serpentine and chlorite range from 1.7-2.8 ppm (Spandler et al., 2014), an insignificant contribution when compared to

the average Sr composition of oceanic crust, 90 ppm (Sun and McDonough, 1989). We therefore conclude that fluids derived from chlorite breakdown in the hydrated mantle portion of the slab dominantly contribute H_2O to the system but do not impart a distinctive trace element signature.

3.5.3. The Role of Sediment Melts and Crustal Assimilation

Low Sr/Nd magmas in the Lassen region have elevated $^{207}Pb/^{204}Pb$, which was previously used to suggest the sub-arc mantle was enriched by a sediment component, but it was concluded that this took place during an earlier, possibly Mesozoic, subduction event because young Pacific sediments did not have high enough Pb isotope ratios to explain the values (Borg et al., 1997). However, radiogenic isotope ratios measured in sediments offshore of Vancouver Island (Carpentier, 2014; Mullen and Weis, 2015) do have high enough Pb isotopic ratios to explain the isotopic compositions of low Sr/Nd magmas in the Lassen region. This new data allows for an alternative hypothesis that variable proportions of hydrous melts of subducted oceanic crust and sediment make up the subduction component in the forearc, whereas sediment melts dominate in the back-arc. This hypothesis, however, requires bulk sediment addition to the mantle wedge rather than sediment melting (Fig. 3.5). Because sediment melts are more physically plausible given the relatively high slab top temperatures beneath the arc, this component should display higher Sr/Nd than bulk sediment, similar to MORB partial melts, but does not (Fig. 3.5). Furthermore, because thermo-petrologic models suggest that the slab becomes completely dehydrated at sub-arc depths, this would require in-situ breakdown of phengite at great depths to drive sediment melting behind the arc-axis (Spandler and

Pirard, 2013). However, low-velocity anomalies agree well with release of fluids from final chlorite breakdown in the mantle portion of the slab at 80 km, and no further evidence provides support for contributions from the slab past this depth. These observations taken together suggest that subduction of a modern sediment component is not responsible for the isotopic compositions of low-Sr/Nd magmas in the Lassen region (Fig. 3.5).

Conversely, a modern sediment component may contribute to variability in isotopic compositions of high-Sr/Nd magmas that trend to slightly more radiogenic values of Sr and Pb, and less radiogenic values of Nd than predicted by the melting model in Figure 3.5. To further distinguish between sediment and slab melt contributions, we use Th/La systematics as a discriminant because of the high Th concentrations found in sediments relative to MORB and sub-arc mantle (Fig. 3.6; Plank et al., 2005). The mixing model in Figure 3.5d shows that Th/La variations in primitive Lassen region magmas may result from addition of <5% of a subduction component that is made up of variable proportions of sediment and MORB melts. At all but two cinder cones, melt inclusion values suggest that <30% sediment melt contributes to the trace element and isotopic enrichments.

Two cinder cones (BPB and CC) have larger apparent contributions from sediment melts. Cinder Cone in particular contains the highest Th/La values from our dataset. However, the bulk lava and tephra at this cone contain abundant quartz xenocrysts and variably melted granitic xenoliths, which are clear indications of large amounts of crustal contamination (M. Clynne, unpublished data). This sample was therefore excluded from radiogenic isotope analyses. We also note that in general, melt

42

inclusions from the Lassen region samples have lower Th/La values on average than many of the published bulk rock analyses from this area (Fig. 3.5; Borg et al., 1997, 2002). This may be because melt inclusions are trapped at depth, before even minor crustal contamination occurs in the shallow crust prior to eruption. Previous work in the Lassen region interpreted unradiogenic Pb and Os isotopic compositions in the relatively primitive basalts and basaltic andesites as evidence for minimal contamination by continental crust (Borg et al., 1997, 2000). However, because of very high Th concentrations in the granitic basement rocks (Cecil et al., 2012), small amounts of crustal addition could increase the Th/La ratio enough to make it difficult to differentiate between sediment melt contribution and that of the basement rocks.

3.5.4. Modeling Slab Melt Addition to the Mantle Wedge

To determine the influence of slab melt addition to the mantle wedge, we used pMELTS (Ghiorso et al., 2002) to compare the effects of fluid addition and hydrous melt addition to the mantle wedge at temperatures and pressures expected for the Lassen sub-arc mantle. To do this, we created a mantle-wedge source composition by adding various amounts of either a dacitic slab melt (Klimm et al., 2008) or pure H_2O to a primitive mantle composition (MM3; Baker and Stolper, 1994). The pMELTS program was then used to determine the phase equilibria of the bulk mixture from 900-1400 °C at a pressure of 1.5 GPa. These values are based on temperatures from geodynamic model results for the Lassen region (Walowski et al., 2015), beginning at the slab-wedge interface to ~100°C hotter than peak temperatures expected in the mantle wedge. Although this method does not attempt to model the kind of reactive transport mechanism that likely

occurs in the mantle wedge, it is conceptually similar to the approach used by experimental petrologists to simulate mantle melting (e.g., Grove et al, 2002), which involve equilibration of a given bulk composition at various temperatures and pressures.

Figure 3.6 compares the fraction of melt produced at various temperatures for a given starting H_2O concentrations in the model mantle sources generated by addition of fluid or melt. Melt fractions for both the hydrous-melt-fluxed and fluid-fluxed peridotite cases are nearly indistinguishable. This suggests that the amount of H_2O supplied to the mantle strongly controls the degree of melting irrespective of whether the H_2O is added as a hydrous melt or a fluid. Slightly higher melt fractions are seen in the melt-fluxed melting case, which may result from the additional fluxing effect of alkalis on the peridotite solidus (Hirschman et al., 1998).
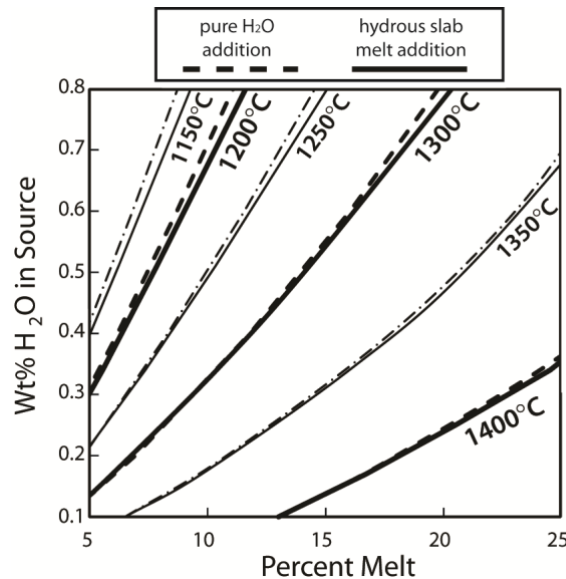
Figure 3.6. Percent melt and source H_2O: results from pMELTS. Relationships between the degree of partial mantle melting and amount of wt% H2O in the starting mantle component at a range of temperatures calculate with pMELTS (Ghiorso et al., 2002). The H_2O in the mantle source (MM3; Baker and Stolper, 1994) was varied by addition of pure H_2O (black dashed lines) and hydrous eclogite partial melts (solid black lines; dacite major element composition with 8 wt% H_2O; Klimm et al., 2008).

44

Figure 3.7 shows the major element compositions of partial melts resulting from various amounts of slab melt and aqueous fluid addition to the mantle wedge. For small amounts of slab melt addition (1-5 wt%), the major element compositions of resulting basaltic melts are similar to those of the aqueous fluid addition case. This shows that equilibrium between partial melt and residual mantle largely controls the major element composition of the final melt. Primary magma compositions calculated from the melt inclusion data have compositions that overlap with the pMELTS model results (Fig. 3.7), demonstrating that hydrous-melt-fluxed melting of the mantle wedge is a viable explanation for the production of these magmas. However, when slab melt addition exceeds 10%, the resulting high bulk H_2O and alkali contents of the fluxed mantle wedge source lead to higher melt fractions at a given temperature, and thus, exhaustion of clinopyroxene occurs at ~1200°C, producing melts with higher SiO_2 at peak mantle wedge temperatures. These high-Mg basaltic andesites may be analogous to natural high-Mg basaltic andesite seen in the Lassen and Mt. Shasta regions (e.g., M. Clynne unpub. data; Grove et al., 2002; Ruscitto et al., 2011).

Figure 3.8b displays the pMELTS model curves for Y and H_2O for various amounts of slab melt addition and temperatures. The H_2O_{max} compositions and average Y concentrations from the Lassen melt inclusions overlap with the model results and are consistent with peak mantle wedge temperatures of 1300-1375°C. The excellent agreement between measured and modeled results, particularly with respect to H_2O, further supports the interpretation that the Lassen primitive magmas were formed by variable addition of a hydrous slab melt component at similar peak mantle wedge temperatures. Values of peak mantle temperatures overlap with those from Till et al.

45

(2012), which predicts temperatures of last mantle equilibration of ~1250-1350°C.

Slightly higher temperatures determined in our study are likely the result of known

temperature over-predictions made by pMELTS of ~50 °C when compared with

experimental methods (Ghiorso et al., 2002).
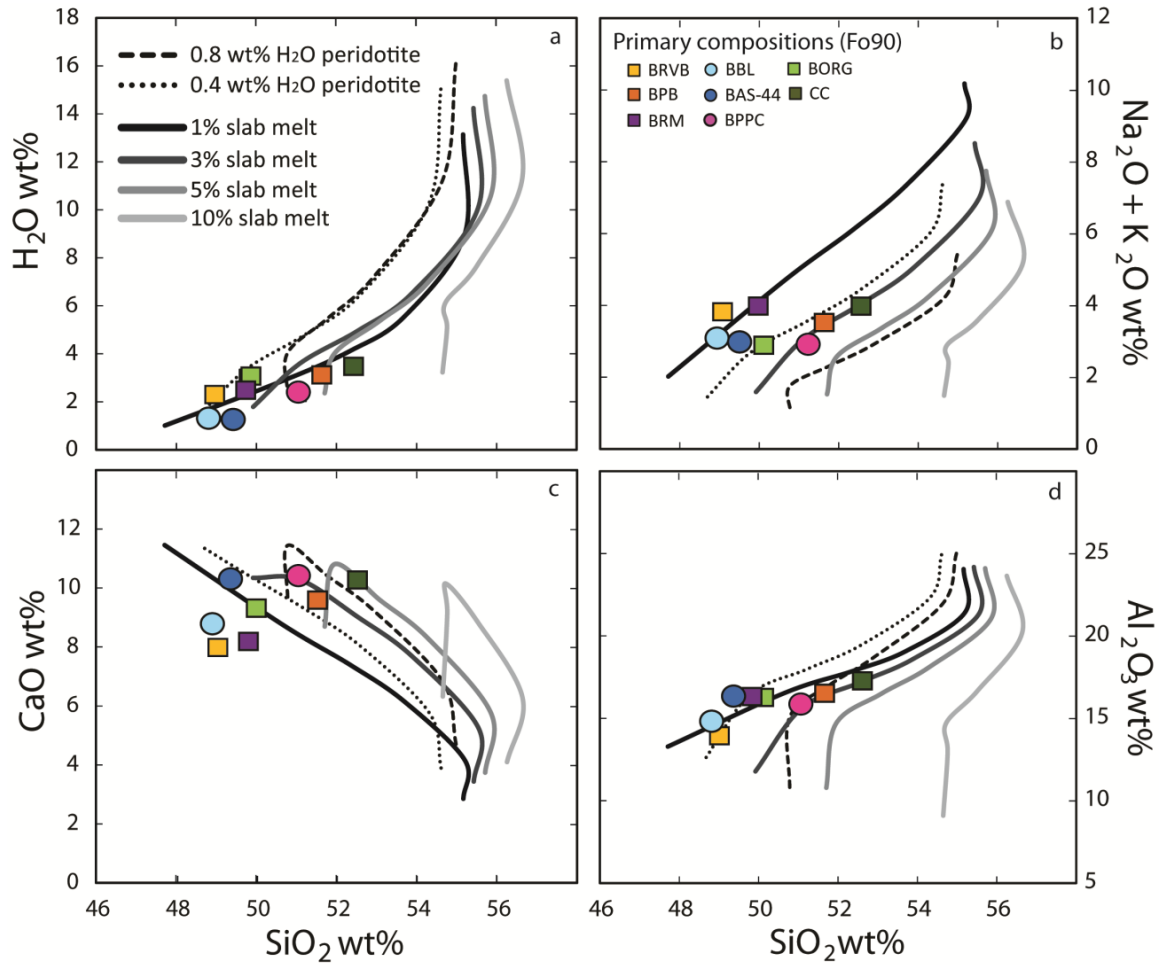
Figure 3.7. Comparison of pMELTS model results and melt inclusion compositions (in eq. with Fo_{90} olivine; Table 2). a) H_2O_{max} (calculated primary composition), b) K_2O + Na_2O, c) CaO and d) Al_2O_3 wt% vs. SiO_2 (all major elements normalized on a volatile-free basis). Phase equilibria were calculated using pMELTS for a mantle source (MM3; Baker and Stolper, 1994) mixed with either pure H_2O (dashed lines) or a hydrous dacite melt (solid lines; Klimm et al., 2008). Each line represent a model result from 900-1400°C at 1.5 GPa (normalized on a volatile-free basis).

3.5.5. The Sr/Y Adakite Signature

One hallmark characteristic of slab melt in arc magmas is high Sr/Y, caused by melting in the presence of garnet, which makes up a large proportion of ecologitized MORB in the downgoing oceanic lithosphere (Duffant and Drummond, 1990). During ecologite melting, Sr is incompatible and increases in the melt phase, whereas Y is compatible with garnet and retained in the downgoing slab. Most Lassen Region magmas, however, do not display high Sr/Y values compared with the global array of adakitic magmas (Fig. 3.8b). Using the same mixed mantle compositions and melt fractions derived from the pMELTS models, melting curves in Figure 3.9b show that for small amounts of slab melt addition (1-10%, similar to major element results), the Sr/Y ratio is dampened due to the addition of Y from the spinel peridotite mantle component. This yields values that overlap with values measured in melt inclusions from all but one sample (BRM) from the Lassen segment (Fig. 3.8b). The results are consistent with previous calculations from Kelemen (1993), which showed that peridotite-melt reactions produced melts with lower LREE/HREE than the initial slab melts. The pMELTS models results indicate that high Sr/Y adakitic signatures may only be retained in arc magmas if slab melt addition is >10 wt%. Larger proportions of slab melt addition are thus required to explain the high Sr/Y value of BRM, consistent with estimates of ~10% slab melt addition derived from radiogenic isotope melting models (Fig. 3.5), and predictions that this sample may have initially contained much higher H_2O concentrations (Fig. 3.4). The high-Mg andesites from the Lassen Region (M. Clynne, unpub. data) and the Mt. Shasta region that have higher values of Sr/Y (~150; Ruscitto et al., 2011) could therefore be produced by larger amounts of hydrous slab melt addition to the mantle wedge.
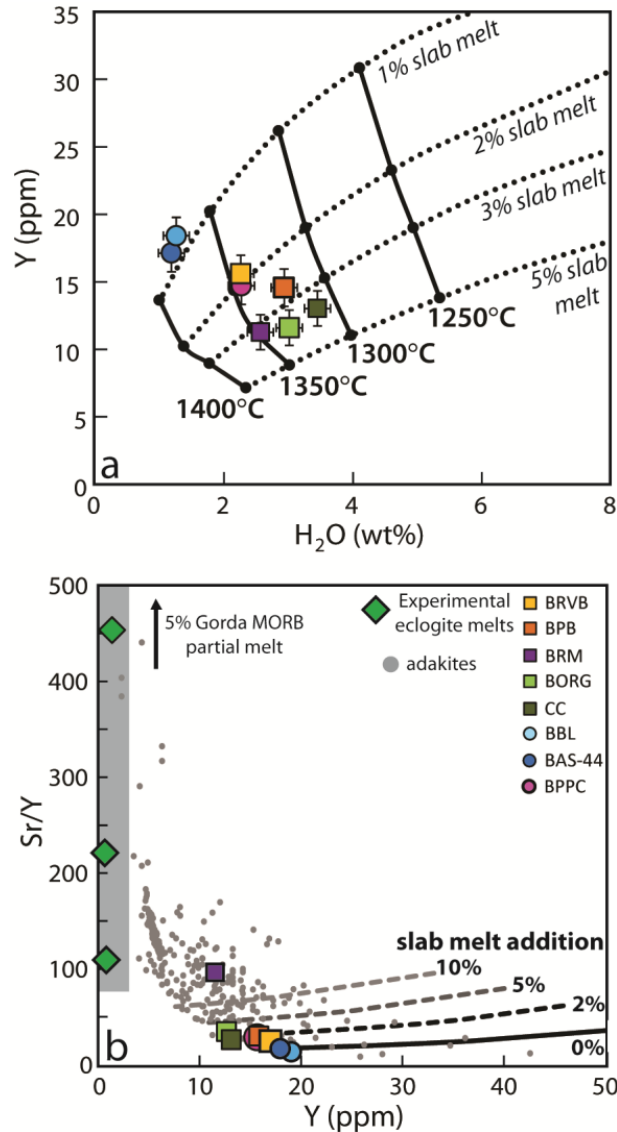
Figure 3.8. The effect of slab melt addition to peridotite for Sr/Y, Y and H_2O. a) H_2O_{max} and b) Sr/Y with average Y for each cone (calculated primary compositions; Fo_{90}; Table 3.1) with global range of adakites (GEOROC database), and experimental eclogite partial melts (Klimm et at., 2008). Solid and dashed curves represent modeled mantle melt compositions for various amounts of slab melt addition from 900-1300°C at 1.5 GPa. Modeled H_2O composition derived as in Fig. 3.7. Modeled Sr and Y were calculated using the batch melting equation for a mantle source (calculated for the Lassen sub-arc mantle) mixed with 2, 5, and 10% (labeled on modeled curves) of a 5% partial melt of Gorda MORB (Davis et al., 2008; partition coefficients from Kessel et al.,2005a; at 4 GPa, 1000°C). Bulk partition coefficients calculated for a spinel peridotite assemblage 35/30/12/5-Ol/OPX/CPX/Sp (Hughes and Taylor, 1986) using mineral partition coefficients of Eiler et al.(2005) for Sr and Eiler et al. (2001) for Y. Melt fractions derived from pMELTS model results (for a given temperature and amount of slab melt addition; Fig. 3.6).

48

Although most primitive Cascade arc magmas do not have particularly high Sr/Y values compared to adakites, they do have other characteristics that indicate melting in the presence of garnet when compared to the global array of basaltic arc magmas. For example, primitive magmas from warm slab subduction zones, such as the Cascades, Mexico, and western Aleutians, display elevated LREE/HREE (e.g., La/Yb; Walowski et al, 2015) and coupled high ^{176}Hf/^{177}Hf and ^{143}Nd/^{144}Nd with lower values of Lu/Hf (Cai et al., 2014) when compared with arcs associated with older oceanic crust. These relationships demonstrate that partial melts of subducted oceanic crust play an increasingly important role in the formation of magmas in arcs beneath which young oceanic crust subducts.

3.5.6. Model for Melt Generation beneath the Southern Cascade Arc

Evidence provided by the geochemical results outlined above suggests that southern Cascade arc magmas are produced by a multi-step process involving fluxing of hydrous slab melts into the hot mantle wedge. Figure 3.9 shows a schematic interpretation of this process that is based on the thermo-petrologic model results of Walowski et al., (2015), the shear wave velocity model from Liu et al., (2012) and the magnetotelluric resistivity data from Wannamaker et al. (2014). In our model, H_2O is retained in the hydrated upper mantle portion of the downgoing slab to greater depths than that at which H_2O is lost from the slab top (Fig. 3.9). Final chlorite breakdown occurs in the slab interior when the slab top reaches ~75-80 km (Fig, 3.9; Walowski et al., 2015). At this depth, the upper portions of the slab consisting of MORB-volcanics are above the MORB+H_2O solidus, and thus should melt when fluxed by rising chlorite-

derived fluids (i.e., Skora and Blundy, 2010; Till et al., 2012; Spandler and Pirard, 2013). The resulting hydrous dacitic melts (Klimm et al., 2008; Jego and Dasgupta, 2013) then rise into the overlying mantle wedge, and react with the surrounding mantle to produce hydrous, calc-alkaline, basaltic to basaltic andesite melts.

As a further test of this model of magma formation beneath the southern Cascades, we determined whether breakdown of chlorite can supply enough H_2O to balance the flux of H_2O erupted from the Cascade arc. Previous work in the Nicaraguan arc and northern Japan has provided evidence for hydration of the deep slab (Ranero et al., 2003; Garth and Rietbrock, 2014) and the importance of fluids released from the deep slab in the production of arc magmas (e.g., Spandler and Pirard, 2013). For the Juan de Fuca plate, higher temperatures at Moho depths caused by the younger slab age may limit the extent of serpentinization (Nedimovic et al., 2009), but no data are available for the Gorda plate to assess upper mantle hydration. Because of this uncertainty, Walowski et al. (2015) conservatively assumed 2 km of hydration below the Moho of the downgoing plate and a bulk H_2O concentration of 2 wt% for the hydrated peridotite. Using these model parameters, the H_2O flux contributed by chlorite breakdown in the slab interior is estimated to be ~1-2 x 10^6 kg/km/yr. For the magmatic flux of H_2O from the Cascades, we use the estimate from Ruscitto et al. (2012). This method, which takes extrusive and intrusive magmatic fluxes into account (Sherrod and Smith, 1990; White et al., 2006) and utilizes primary volatile contents from the central Oregon Cascades (which overlap with those from the Lassen region), yields a maximum H_2O flux of 1.93 x 10^6 kg/km/yr. This agrees very well with the flux resulting from our thermo-petrologic model, demonstrating that fluids derived from the breakdown of chlorite in the hydrated upper mantle portion of

the slab may be sufficient to produce observed magmatic and volatile fluxes in the Cascade arc.

The thermo-petrologic model results of Walowski et al., (2015) also predict two main pulses of fluids from the downgoing slab associated with 1) the final breakdown of hydrous phases during eclogitization of the oceanic crust, and 2) the final breakdown of chlorite in the hydrated mantle portion of the slab (Fig. 3.9). The first, more shallow pulse of fluid release correlates well with the location of low-resistivity anomaly beneath the forearc (Wannamaker et al., 2014), and likely reflects a region of serpentinization of the cold nose of the mantle wedge. The second predicted location, caused by the release of the hydrous melt from the slab, agrees well with regions of low shear wave velocity beneath the Lassen region (Liu et al., 2012). This is consistent with models of fluid migration into the mantle wedge which suggest that, for most values of wedge permeability, slab dip, and convergence velocity, there is a net migration of fluids and melts away from the trench (Cagnioncle et al., 2007). This implies that arc magmas will inherit a slab signature from a region of the slab that is slightly up-dip of the region that lies directly beneath the arc. Therefore, patterns of decreasing amounts of a subduction component towards the back-arc as observed in the geochemical data (Borg et al., 1997; 2002), provides further support for these interpretations.
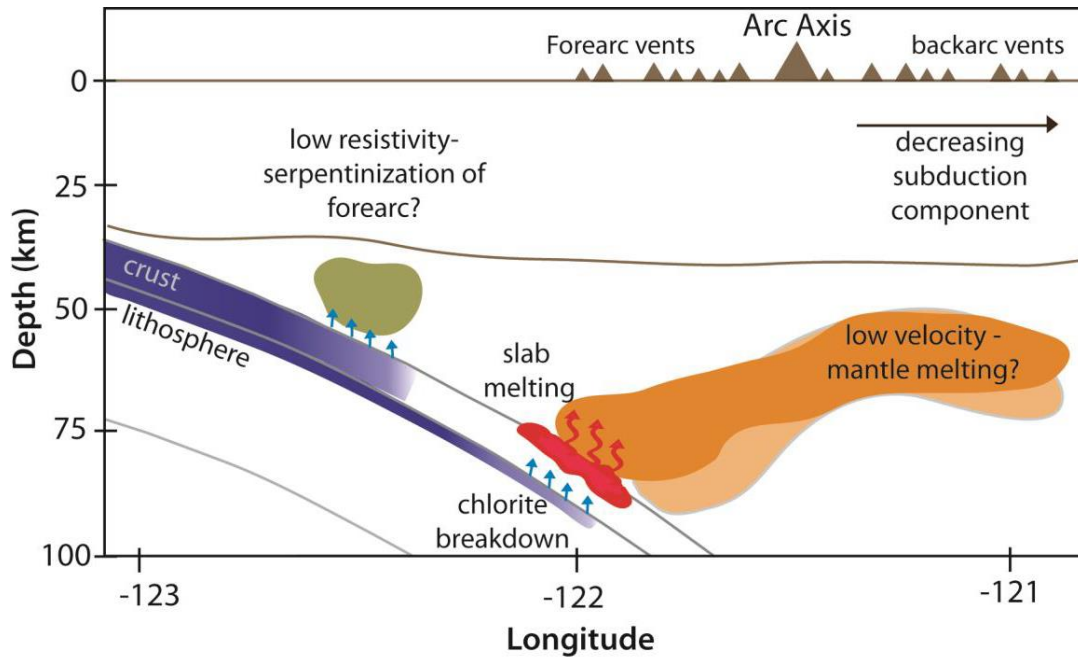
Figure 3.9: Schematic interpretation for magma formation beneath the S. Cascades. Chlorite-derived fluids from the deep slab interior beneath the forearc vents (small blue arrows) drive flux-melting of the oceanic crust (red colored area), producing hydrous slab melts that migrate into the overlying mantle (red arrows), where they react with peridotite to induce further melting. The location of hydrous phase stability in the downgoing slab (dark blue shaded region) and main pulses of fluid release from the slab (small light blue arrows) are based on the thermo-petrologic model results of Walowski et al. (2015). Area of low-velocity (dark and light orange shaded regions for latitudes 41° and 40.6°, respectively) based on shear wave velocity model of Lui et al. (2012). Green shaded region shows the location of low resistivity from Wannamaker et al. (2014).

3.6. Conclusions

Our results provide strong evidence that magma production in the southern Cascade arc is driven by hydrous slab melt addition to the mantle wedge. Low B concentrations and MORB-like B isotope compositions indicate that extensive dehydration of the plate occurs before it reaches sub-arc depths. However, the abundance of volatile elements and correlation of volatile and trace element ratios (H_2O/Ce, Cl/Nb, Sr/Nd) show that Lassen region magmas have been enriched by variable amounts of addition of a hydrous subduction component. Correlation of fluid mobile trace elements

and radiogenic isotopes demonstrates that the subduction component in the southern

Cascades is less radiogenic than the sub-arc mantle wedge, and must be derived from a

partial melt of the subducting Gorda MORB. pMELTS model results show that hydrous-

melt-fluxed melting of the mantle wedge can produce basaltic magmas with similar major

element compositions to those measured in Lassen melt inclusions. Agreement between

pMELTS model results and measured concentrations of H_2O and Y confirms that

variations between magmas are likely formed by differences in the amounts of slab

component addition to the mantle wedge at peak temperatures of approximately ~1300-

1350°C. Our results provide further evidence that chlorite-derived fluids from the deep

slab interior can flux-melt the oceanic crust, producing hydrous slab melts that migrate

into the overlying mantle, where they react with peridotite to induce further melting.

3.7. Bridge

In the preceding chapter (III), the compositions of olivine-hosted melt inclusions

from eight cinder cones were used provide evidence for slab melting and investigate

magma generation processes in the mantle wedge beneath the southern Cascades. In the

next chapter (III), I will focus on the youngest cinder cone in the Lassen region, Cinder

Cone (1666 C.E., Sheppard et al., 2009) to explore the melt evolution and plumbing

system dynamics prior to and during monogenetic eruptions in the southern Cascades.

CHAPTER IV

UNDERSTANDING MELT EVOLUTION AND THE MAGMATIC PLUMBING SYSTEM AT CINDER CONE, LASSEN VOLCANIC NATIONAL PARK, CALIFORNIA: INSIGHTS FROM OLIVINE-HOSTED MELT INCLUSIONS

This chapter includes material co-authored with Dr. P.J. Wallace, Dr. K. V. Cashman, J.K. Marks, Dr. M.A. Clynne, and Dr. Philipp Ruprecht. Sample collection was performed by me with the help of Dr. Wallace, Dr. Cashman, J.K. Marks, and Dr. Clynne. All melt inclusions were prepared and analyzed by me using Fourier transform infrared spectroscopy (H_2O and CO_2), electron microprobe (major elements), and laser ablation inductively coupled plasma mass Spectrometry (trace elements). Analyses, data corrections, geochemical modeling, and interpretation were performed by me, with the help of Dr. Wallace. This melt inclusion dataset is integrated with tephra stratigraphy, componentry, and textural analyses performed by J.K. Marks (Marks, 2012). I drafted all the figures used in this article and the text was written by me, with editorial assistance by Dr. Wallace.

4.1. Introduction

Spanning approximately 1,250 km along the margin of the northwestern United States and southern Canada, the Cascade magmatic arc is comprised of over 2,300

Quaternary volcanoes (Hildreth, 2007). Less than 30 of these volcanoes, however, represent the most identifiable high peaks of the Cascades, while the majority of the vents are small mafic shields and cones (Hildreth, 2007). In the Lassen area alone, over 500 monogenetic cinder cones and small shield volcanoes have erupted in the last 12 Ma (Guffanti et al., 1990; Borg et al., 1997), and they collectively account for a large fraction of the total erupted volume in the southern Cascades (Sherrod and Smith, 1990). Despite the abundance of monogenetic volcanoes in the Cascades, and consequently, their likelihood to pose volcanic hazards in the northwestern United States, these types of volcanoes are understudied in comparison to the more evolved and longer-lived stratovolcanoes.

Compositionally, monogenetic volcanoes in the Cascades are typically mafic, and they can therefore be used as windows into mantle processes such as arc magma formation (e.g., Borg et al., 1995, 1997; Leeman et al., 2004; Ruscitto et al., 2010; Walowski et al., 2015). The eruptions of cinder cones typically last <1-15 years, and these short timescales often result in limited evolution of their magmas. It has been shown, however, that despite these short timescales, some cinder cones produce evolved compositions and complex plumbing systems (e.g., Pioli et al., 2008). At Paricutin in Mexico, for example, magmas evolved from basalt to andesite over the course of the eruption that lasted ~9 years (McBirney et al., 1987; Luhr and Carmichael, 1985; Luhr, 2001; Rubin et al., 2004; Erlund et al., 2009). This compositional evolution was accompanied by a decrease in explosivity and magmatic volatile contents, providing insight into shallow storage reservoirs beneath cones in central Mexico (Pioli et al., 2008; Johnson et al., 2008). At Cinder Cone, in Lassen Volcanic NP, CA, bulk compositions

also evolve systematically over the course of the eruption (Clynne et al., 2000). However, this eruption occurred over a significantly shorter period of time, suggested to be less than one year (Clynne et al., 2000; Sheppard et al., 2009). How do the compositions of magmas from Cinder Cone evolve so rapidly? With a complicated inter-fingering of tephra and lava flows, can we connect pre-eruptive changes in magma chemistry to changes in eruption dynamics? What are the timescales associated with the formation, storage, and ascent of these magmas?

To investigate these questions, we focus on the composition of olivine-hosted melt inclusions sampled from the entire eruptive sequence at Cinder Cone. Melt inclusions are small volumes of melt trapped inside of phenocrysts at depth, and as such they can provide two unique insights in addition to traditional methods of bulk rock and mineral chemistry. (1) Melt inclusions trapped in early crystallizing phases, such as olivine, provide snapshots of melt chemistry, potentially before additional magmatic evolution by fractional crystallization, mixing, and/or contamination occurs. In this way, melt inclusions may provide better information about parental melt compositions, and thus, better constraints on the processes of formation, storage, and evolution of the erupted material. (2) Melt inclusions can be used to estimate pre-eruptive volatile contents (e.g. and Wallace, 2008). The pre-eruptive concentrations of volatiles, such as H_2O, CO_2, S, Cl, in a magma are key to understanding a variety of processes from mantle melting (Gaetani and Grove, 1998; Grove et al., 2006; Hirschmann et al., 2009) to magma ascent and eruption (e.g., Roggensack, 1997; Metrich and Wallace, 2008). Pre-eruptive volatile contents are difficult to determine, however, because they decrease in solubility as pressure decreases and therefore degas from the magma during ascent,

56

driving explosive eruptions, and leaving the erupted material with only a fraction of the volatile contents with which it began (Holloway and Blank, 1994). Melt inclusions (MI) are one of the best tools currently available to directly measure pre-eruptive volatile concentrations, because they are trapped at depth, often before significant degassing occurs. Because the solubility of H_2O and CO_2 in magmas is sensitive to pressure, their concentrations within MI can also provide estimates of entrapment pressures (Newman and Lowenstern, 2002; Papale et al., 2006; Iacono-Marziano et al., 2012), and therefore, magma storage depths (e.g., Johnson et al, 2008; Pioli et al., 2008). Although recent work has shown that melt inclusions are not perfect storage containers and can lose H+ (protons) by diffusion through the host and CO_2 due to formation of a vapor bubble in the inclusion, there are methods for distinguishing and correcting for these effects (e.g., Bucholz et al., 2013; Lloyd et al, 2013; Wallace et al., 2015).

In this study, we use major, trace, and volatile element concentrations in olivine-hosted melt inclusions from the tephra deposit at Cinder Cone in conjunction with lava and bulk tephra compositions and olivine major and trace element chemistry. We interpret the data with regard to stratigraphic relationships between lava and tephra and textural analyses of tephra clasts (Marks, 2012). We use these results to shed light on the processes that led to compositional evolution of the magmas and accompanying changes in eruptive dynamics at Cinder Cone. We show that the volatile contents of melt inclusions can provide insight into the minimum depths at which these magmatic processes occur. We also demonstrate the usefulness of melt inclusions in determining the composition of the mantle source, in a case when the erupted bulk material is sufficiently contaminated by crustal processes. Lastly, we estimate the timescales of

57

olivine residence times in the magmatic system to compare with the estimated timescale of eruption. Using these results, we formulate a schematic model for the plumbing systems beneath Cinder Cone.

4.2. Geologic Setting

Cinder Cone is a basaltic andesite scoria cone located in the northeast corner of Lassen Volcanic National Park (Fig. 4.1). Lassen Volcanic National Park encompasses 430 km^2 of volcanically-sculpted landscape surrounded by the Sacramento Valley and Klamath Mountains to the west, the Sierra Nevada to the south, and the Basin and Range to the east. The park gets its name from Lassen Peak, the tallest point in the national park, a dacite dome complex that last erupted in 1915. Tectonically, Cinder Cone is found within the Lassen Segment where volcanism is related to oblique subduction of the Gorda micro-plate beneath the North American plate, producing the more abundant calc-alkaline magmas (Clynne and Muffler, 2010). Tholeiitic magmas are also common in this region, and are often associated with extensional faulting, the results of westward expansion of the Basin and Range province impinging on the southern Cascade arc. The quaternary volcanics in the Lassen region sit above older mafic to intermediate volcanoes and volcanic products 2-4 km thick (Berge and Stauber, 1987). This volcanic basement is underlain by plutonic Sierran and metamorphic Klamath terrain basement rocks as suggested by mapped outcropping units (e.g. Saleeby et al., 1989; Cecil et al., 2012) and constant modeled seismic velocities across the Sierra Nevada-Cascade Range boundary (Berge and Stauber, 1987).

The eruptions and volcanic history of Cinder Cone have been an ongoing controversy over the past century, and its eruption in 1666 A.D. was only recently confirmed by radiocarbon dates of trees killed by the lava flows (Clynne, 2000). Dendrochemistry and ring-width analyses of living trees were also utilized to determine that the entire eruption likely occurred in less than one year (Sheppard et al. 2009). At approximately 350 years old, it is the youngest cinder cone in the Cascade Arc and, as such, has remained unvegetated allowing for excellent preservation of the lava flows and tephra deposit (Clynne and Muffler, 2010). The eruptive material is comprised of a ~200-meter-tall scoria cone built on top of an earlier cone, a tephra deposit as much as 3 meters in thickness and ~20 by ~10 kilometers in spatial extent, and five main lava flows separated into three phases – Old Bench, Painted Dunes, and Fantastic Lava (OB, PD, and FL, respectively; Clynne and Muffler, 2010)(Fig. 4.1).

4.3. Sample Descriptions and Tephra Stratigraphy

The tephra deposit was first described in detail by Heiken (1978) and originally separated into three phases, Units 1, 2, and 3, thought to correspond with the three phases of lava flow emplacement, OB, PD, and FL, respectively. Samples used in this study were collected from a ~1.2-m-deep pit to the north of Cinder Cone (Fig. 4.2; yellow star in Fig. 4.1). Ten samples were collected from distinctive golden layers throughout the section. Field descriptions of each sample are listed in Table 4.1, and a corresponding field photo is labeled in Figure 4.2. The lowermost sample from the column, LCC-1-9, is interpreted to be the opening phase of Unit 2, because it is thicker than the maximum

59

measured thickness of Unit 1 by Heiken (1978). Unit 2 is visually distinct from Unit 3 in

that it has appears to contain a higher percentage of larger golden tephra clasts. The Unit
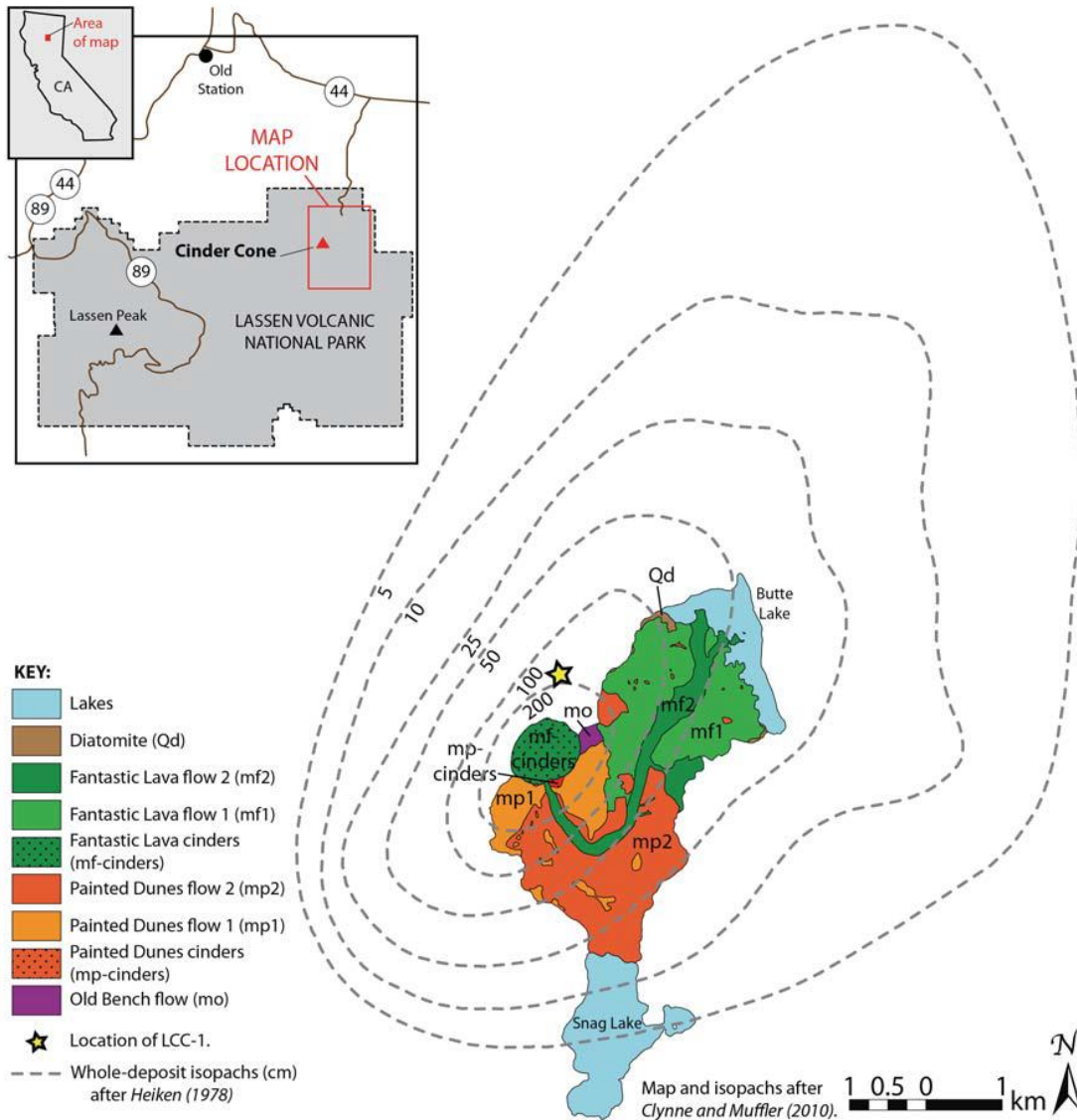
Figure 4.1. Geologic and isopach map of Cinder Cone showing the distribution and geology of the lava flows, and the whole-deposit tephra isopachs. The main tephra column used in this study is shown as the yellow star. The three phases of the lava flows are Purple = Old Bench (tephra Unit 1), orange = Painted Dunes (tephra Unit 2), and green = Fantastic Lava (tephra Unit 3).

60

2 tephra deposit, calculated to have a minimum volume of ~0.6 km^3, is also less voluminous and widespread than Unit 3, which covers ~0.15 km^3 (Marks, 2012). LCC-1-5 is a dark fine ash layer which is interpreted to represent the boundary between Units 2 and 3, and also signifies a change in eruptive dynamics (Marks, 2012). The uppermost layer, LCC-1-1, is overlain by a thin white layer of white 1915 Lassen Peak pumice.

There are several curiosities about Cinder Cone's deposits and therefore its eruption. First, there are ubiquitous quartz xenocrysts in all of the basalt-basaltic andesite lava flows and tephra layers (Clynne et al., 2000). Second, the bulk composition of erupted material changed from basalt to basaltic andesite through the PD flows and from basaltic andesite to basalt through the FL flows (Clynne et al. 2011). The tephra mimic these changes: tephra Unit 2 is compositionally similar to the PD flows and tephra Unit 3 is compositionally similar to the FL flows (Clynne et al. 2011).

Of the ten samples collected, six were chosen for melt inclusion analysis to best represent the main eruptive phases. Tephra from LCC-9, LCC-7, and LCC-6 represent the early erupted tephra, LCC-5, and LCC-4 are interpreted to represent the transition in eruptive phases (closing phase of Unit 2 and opening phase of Unit 3, respectively), and LCC-2 represents the late erupted tephra (Fig. 4.2). These samples were chosen to understand the chemical transitions that accompany the textural changes of the tephra deposit.
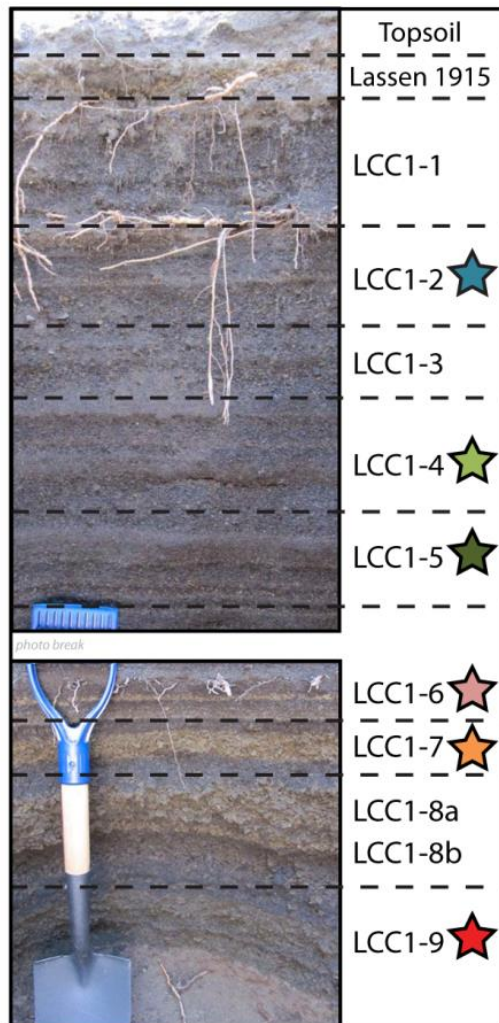
Figure 4.2. Stratigraphic section of sample locality. Field photo of the main tephra column, with samples labeled and color-coded by tephra units. Colors will be used throughout study. Descriptions can be found in Table 4.1 (Photo credit: K. Cashman.)

Table 4.1. Tephra Stratigraphy and Sample Descriptions

Thickness	Unit	Description
--	--	A thin layer of 1915 pumice lies at the top of the section
10 cm	LCC1-1	Coarse ash, vaguely laminated with abundant lava chips
2.5 cm	--	Fine ash layer with abundant roots
2.5 cm	--	Coarse ash layer
1 cm	LCC1-2	Tan fine ash layer
15 cm	LCC1-3	Two coarse ash layers separated by a thin fine ash layer
15 cm	LCC1-4	Two coarse ash layers separated by a thin fine ash layer
2.5 cm	--	Fine ash layer
17.5 cm	--	Alternating cm-size layers of coarse and fine ash
2.5 cm	LCC1-5	Fine ash layer that separates Fantastic Lava from Painted Dunes
1 cm	LCC1-6	Tan Lapilli layer
5 cm	--	Coarse ash layer of dark scoria intermingled with blond tephra
3.75 cm	LCC1-7	Tan Lapilli layer
3.75 cm	--	Dark ash with dense clasts
20 cm	LCC1-8	Coarse tan lapilli layer, inversely graded. Base has abundant oxidized cinder clasts
5 cm	--	Dark coarse ash layer
12.5 cm	LCC1-9	Coarse ash layer with mixed tan and black clasts

4.4. Methods

4.4.1. Sample Preparation

The ash sized fraction of tephra was used for the melt inclusion analyses because it quenches more rapidly than lava flows, bombs, and lapilli sized tephra clasts, minimizing the potential effects post-entrapment modification after eruption (Lloyd et al., 2013). Loose olivine crystals, 1 mm to 250 μm in size, were hand-picked from the washed and seived tephra. The olivine crystals were treated in HBF_4 to remove adhering glass and examined in immersion oils (refractive index 1.675) to locate melt inclusions. Olivine crystals from the deposit are generally euhedral and all contain chrome-spinel inclusions. Nearly all melt inclusions also contained a 10 to 30-μm-diameter vapor bubble. Olivine hosting fully enclosed and glassy melt inclusions were mounted in crystal bond on glass slides and prepared as doubly polished wafers. Wafers were immersed in acetone to completely dissolve the crystal bond before Fourier transform infrared

spectroscopy (FTIR) analysis, and subsequently mounted in epoxy for electron probe

micro-analysis (EPMA) and laser ablation inductively coupled plasma mass spectrometry

(LA-ICP-MS) analyses.

4.4.2. Analytical Procedures

4.4.2.1. FTIR

H_2O and CO_2 concentrations were measured at the University of Oregon using a

Thermo-Nicolet Nexus 670 FTIR spectrometer interfaced with a Continuum IR

microscope. Concentrations were calculated from IR peak absorbances using the Beer–

Lambert law: $C=MA/\rho d\varepsilon$, where M is the molecular weight of H_2O or CO_2, A is the

measured absorbance of the band of interest (3550 cm^{-1} for H_2O, and 1515 and 1435 cm^{-1}

for CO_2), ρ is the glass density at room temperature, d is the thickness of the MI wafer,

and ε is the molar absorption coefficient. An absorption coefficient of 63 L/mol cm

(Dixon et al., 1995) was used for H_2O whereas the absorption coefficients for CO_2 were

calculated for each inclusion based on the major element composition (Dixon and Pan,

1995). The background subtraction methods used to determine the carbonate peak heights

at 1515 and 1435 cm^{-1} are described in Roberge et al, (2005).

4.4.2.2. EPMA

Melt Inclusions and host olivine were analyzed for major elements, S, and Cl on

the Cameca SX-100 electron microprobe at the University of Oregon CAMCOR

MicroAnalytical Facility. MI glass compositions and host olivine were analyzed with a

10 nA, 10 µm diameter beam and 15 kV accelerating voltage for major elements. Time

dependent intensity corrections were made for Na, K, Si, and Al, and these elements were analyzed first. Subsequently, the beam current was increased to 50 nA for collection of S, Cl, Ti, and P. Individual inclusion analyses are averages of three point analyses. Olivine compositions are also averages of three point analyses taken ~100 μm away from inclusions and crystal edges to ensure analysis of olivine unaffected by later stage diffusion.

4.4.2.3. LA-ICP-MS

Melt inclusions and host olivine were subsequently analyzed for a suite of trace elements on the Photon Machines Analyte G2 193 nm ArF ''fast''Excimer Laser system at Oregon State University, using 50 μm spot size with a 5 Hz pulse rate. Measured trace element concentrations were determined by reference to GSE-1G glass as a calibration standard and using 43Ca as an internal standard (see Loewen and Kent, 2012, for details). BHVO-2G, BCR-2G, and GSD-1G glasses were also analyzed to monitor accuracy and precision, and the analyzed values were within 10% of accepted values. A larger set of olivine phenocrysts from LCC-2, LCC-4, and LCC-9 were analyzed at Lamont-Doherty Earth Observatory. Data was acquired using a 193 ArF Eximer laser with a PQExcell ICPMS operated in continuous line scan mode using a circular laser spot (25 μm for data acquisition and 50 μm for pre-ablation) from the core to the rim of each olivine crystal. Scan speed was 3 μm/s (30 μm/s during pre-ablation) and laser pulse rate was held at 15 Hz. Calibration curves were obtained using a set of reference glasses (BIR, BHVO, GOR132-G and GOR128-G) for 15 elements (Li-7, Mg-26, Al-27, P-31, Ca-44, Sc-45, Ti-47, V-51, Cr-52, Mn-55, Fe-57, Co-59, Ni-60, Cu-65, Zn-66). MPI-Ding Gorgona

glasses were specifically included to obtain good calibrations for element compatible in olivine (most notably Ni). Mg-26 was used as internal standard. New calibration curves were obtained prior to each sample. Reference glasses KL2-G and ML3B-G, and San Carlos olivine (USNM 111312/444), were also analyzed to monitor accuracy and precision.

4.5. Results

4.5.1. Olivine Compositions

The host olivines have core compositions of $Fo_{88-90.5}$. A larger population of analyzed olivine phenocrysts from LCC-9, LCC-4, and LCC-2 overlap with the MI host olivine compositions (Fig. 4.3a), and exhibit broad, homogenous cores and thin Fe-rich rims. From this larger population, 10 crystals were identified as xenocrysts because they have variable zonation patterns and contain cores of Fo_{78-87} . These xenocrysts are excluded from Figure 4.3 because they are not representative of the main phenocryst populations. The olivine hosts for the analyzed melt inclusions have high core forsterite compositions. Early erupted tephra have slightly more Mg-rich olivine cores ($Fo_{89-90.5}$) compared with the later erupted tephra (Fo_{88-89}) (Fig. 4.3). Ealy- and late-erupted olivine phenocrysts are also distinguished from each other in their trace element compositions (Fig. 4.3b), with early-erupted olivine containing high Fo cores with a more restricted range in Ni. These values are consistent with olivine previously analyzed from both lava and tephra (M. Clynne, unpublished data).

4.5.2. Post-entrapment Crystallization and Fe-loss Corrections

The melt inclusions analyzed in this study were all sampled from rapidly quenched tephra. However, melt inclusions are commonly affected by crystallization of olivine along the walls of the inclusion and by Fe diffusive loss during the time between trapping and eruption. If the measured composition of a melt inclusion is not in equilibrium with the surrounding host olivine, then the melt inclusion has likely experienced post-entrapment crystallization (PEC; Danyushevsky et al., 2000). The original melt inclusion composition can be estimated by incrementally adding equilibrium olivine back into the melt until it is in equilibrium with its host
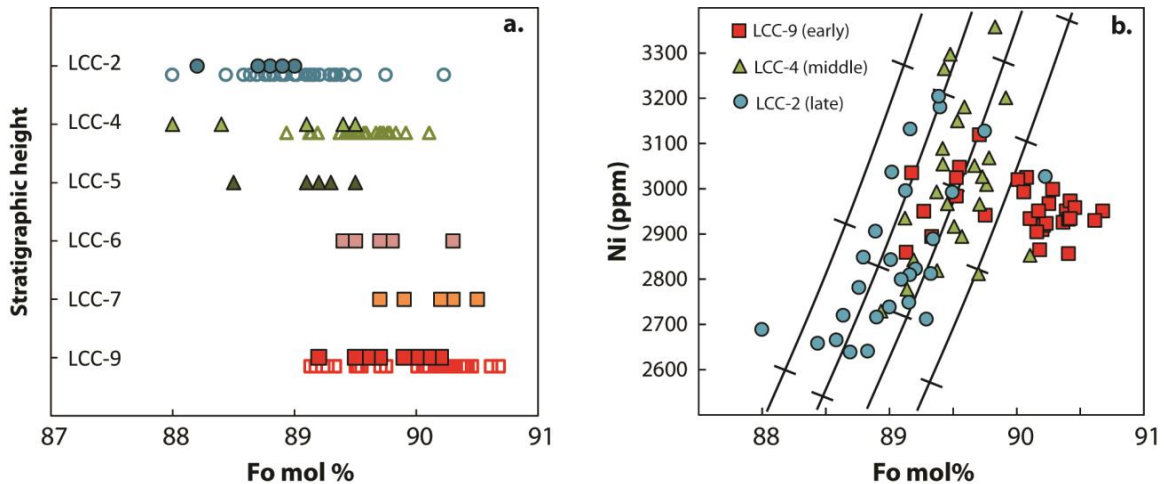
Figure 4.3. Olivine phenocryst compositions. a) Fosterite content of olivine hosting melting inclusions (filled symbols) and larger olivine population measured by LA-ICP-MS (open symbols) ordered by relative stratigraphic height. See Table 4.1 and Fig. 4.2 for exact stratigraphic heights. b) Ni versus Fo for olivine phenocryst cores from the larger population measured by LA-ICP-MS. This excludes olivine xenocrysts, as described in main text. Solid black lines are fractionation curves labeled with tick marks which represent 1% of olivine fractionation.

olivine (e.g., Ruscitto et al., 2010). In this study, Petrolog 3.1 (Danyuchevsky and Plechov, 2011) was used to determine original melt inclusion compositions and to calculate the percent of olivine crystallized from the melt inclusion after entrapment. For this correction, Petrolog 3.1 used Fe-Mg partition coefficients (K_d) between the melt and host olivine from Ford et al. (1983). Oxygen fugacity was determined using the partitioning of V between the melt inclusion and host olivine using methods of Mallmann and O'Neill (2009). The oxygen fugacities of the most primitive MIs were ΔQFM +1.4 ($\pm$0.4), with no distinct difference between eruptive units.

Post-entrapment crystallization corrections also require an estimate of the initial Fe content of the MI prior to Fe-loss by diffusion. Bulk tephra analyses from Cinder Cone were used as a proxy to estimate the original Fe contents. Primitive lavas in the Lassen region have 7-8 wt% FeO^T which overlaps with or is slightly higher than the values for Cinder Cone lavas and bulk tephra (5.5-7 wt% FeO^T). Based on this comparison we assumed that Cinder Cone melts initially had 7 wt% FeO^T. Volatile and incompatible trace element concentrations in the melt inclusions were also corrected for PEC using the Petrolog 3.1 results.

4.5.3. Major Element Compositions

We present data for 47 melt inclusions, 24 of which are from early units, 15 from transitional units, and 8 from the late-erupted tephra. Corrected melt inclusions are basaltic to basaltic andesite in composition (Fig. 4.4), and most fall in a narrow range of SiO_2 contents (51-53 wt% on a volatile-free basis). Variability in total alkalis, however, shows compositional differences in MIs from different units. Early-erupted units (LCC-9,

LCC-7, LCC-6) have lower alkalis (~3.5-4 wt% Na_2O+K_2O) compared to middle- and late-erupted units (LCC-5, LCC-4, LCC-2), which have higher values (~4-4.5 wt%). Middle-erupted or transitional units (LCC-4 and LCC-5) display the most compositional variability and contain the greatest number of inclusions that have higher concentrations of both SiO_2 and alkalis. This pattern is also apparent in the concentrations of other major elements, such as MgO and CaO, which are elevated in early-erupted MIs compared to late-erupted MIs, but highly variable in the transitional units (Fig. 4.5). Because early- and late-erupted MI are easily distinguished with most major elements and are found within tephra units that display distinct eruptive dynamics (Marks, 2012), for simplicity, we will refer to the average early-erupted MI composition as magma batch 1 and the average late-erupted MI composition as magma batch 2.

Most MIs have distinctly lower SiO_2 than the lavas and bulk tephra (Fig. 4.4). This is an indication, as will be discussed further below, that the magmas at Cinder Cone were crustally contaminated after olivine growth and MI entrapment. Furthermore, most olivine crystals (Fo_{89-90}) are not in Fe-Mg equilibrium with the lava and bulk tephra and often contain thin reaction rims of pyroxene (M. Clynne, unpublished data). We did not analyze matrix glass, but the composition of olivine in equilibrium with the bulk tephra (which is olivine enriched compared to the matrix) is $Fo_{87-87.5}$. The olivine phenocrysts rims are also commonly Fo_{88-87}. Therefore, most olivine phenocrysts at Cinder Cone must have grown from a more primitive parental magma before the magma became contaminated. Interestingly, the differences in alkalis between early-erupted and late-erupted MIs are mirrored in the total alkali concentrations of lava and bulk tephra (Fig. 4.4). Melt inclusions with elevated SiO_2 (>54 wt%), which mostly come from the

69

transitional units, overlap with lava and tephra in MgO and Al_2O_3 content, and likely

represent melts that were affected by crustal contamination before being trapped in

olivine (Fig. 4.4 and 4.5).

4.5.4. Volatile Concentrations

H_2O and CO_2 concentrations measured in melt inclusions at Cinder Cone range

from 0.7-3.5 wt% and 0-1500 ppm, respectively (Fig. 4.6), similar to values for other
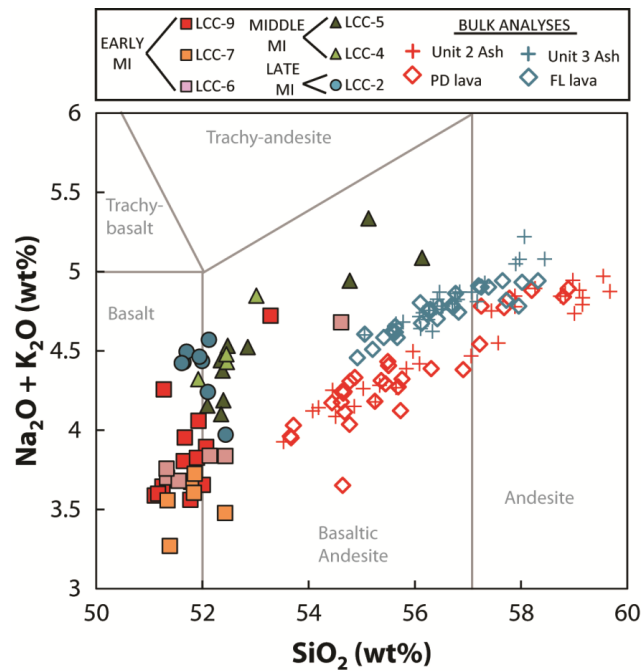
Figure 4.4. Melt inclusion total alkalis and SiO_2 compared to bulk tephra and lava. Filled symbols are melt inclusions from this study normalized on a volatile-free basis. Bulk lava (open diamonds) and tephra (crosses) are unpublished data from M. Clynne. Classification boundaries for basalt, basaltic andesite, andesite, trachy-andesite, and trachy-basalt from LeBas et al., (1986). Uncertainty is less than the symbol size (See Supplementary Table C.1; see Appendix C for all supplementary information for this chapter).
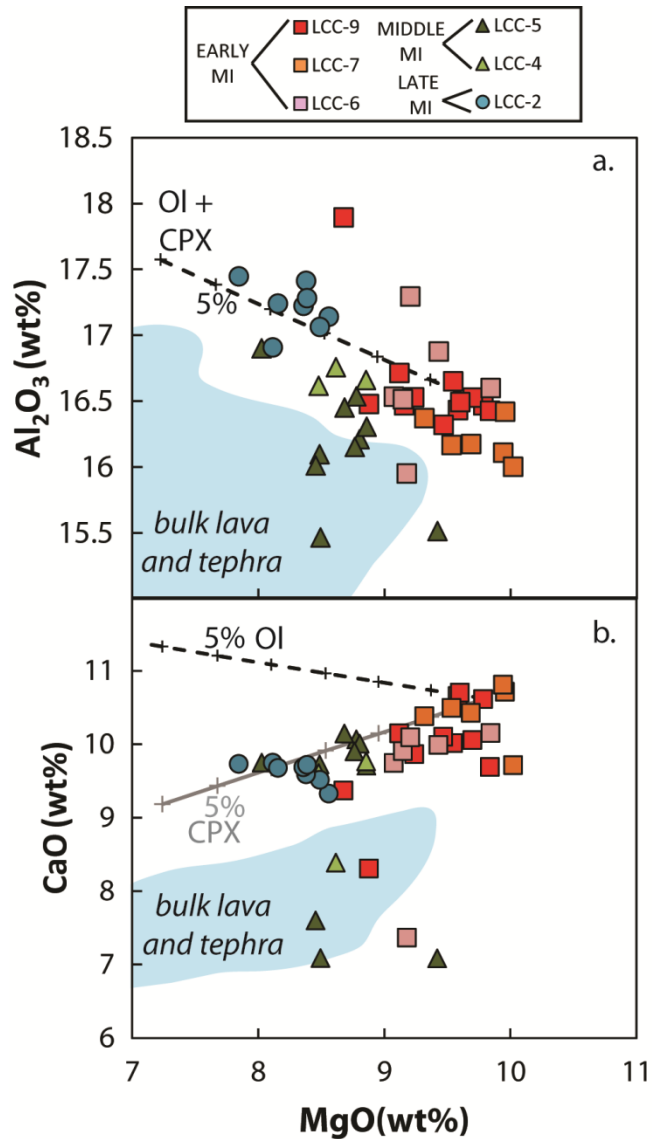
Figure 4.5. Melt inclusion MgO vs. Al_2O_3 and CaO. MgO vs. a) Al_2O_3 and b) CaO for MI compositions (normalized on a volatile-free basis) compared with lava and bulk tephra (shaded blue region; M. Clynne unpublished data). Fractionation curves calculated using Petrolog 3.1 for olivine (Ol, black dashed line; Danyushevsky and Plechov, 2011) and Rhyolite-MELTS at 10 kbar for clinopyroxene (CPX, grey line; Gualda et al., 2012), with tick marks representing 1% fractionation. Uncertainty is less than symbol size (see Supplementary Table C.1).

nearby cinder cones Walowski et al., 2015; in prep.) and cones in the central Oregon Cascades (Ruscitto et al. 2010; Ruscitto et al., 2011; LeVoyer et al., 2011). However, a number of recent studies have shown that MI commonly experience post-entrapment changes that decrease their dissolved H_2O and CO_2 concentrations (Esposito et al., 2011; Gaetani et al., 2012; Bucholz et al., 2013; Lloyd et al., 2013; Hartley et al., 2014; Moore et al., 2014; Wallace et al., 2014). The measured dissolved concentrations therefore represent a minimum estimate of the initial H_2O and CO_2 contents of the magma during entrapment.

Most basaltic MI, including nearly all MI in this study, contain a vapor bubble, the size of which can be used to determine if it is primary (co-entrapped with melt) or formed after entrapment (Riker et al., 2005; Aster et al., in prep.). Shrinkage bubbles form after entrapment as a result of the pressure drop caused by crystallization along the host-inclusion interface and thermal contraction of the melt (Roedder, 1979; Lowenstern, 1995). Because CO_2 has a much lower solubility than H_2O, it strongly partitions into the bubble, leaving only a fraction of the CO_2 dissolved in the melt compared to that at the time of entrapment (Esposito et al., 2011; Hartley et al., 2014; Moore et al., 2014). Recent work suggests that 40-90% of the total CO_2 in the MI can be lost to this shrinkage bubble (Moore et al., 2014; Wallace et al., 2014), leading to a drastic underestimation of entrapment depths when only dissolved CO_2 is taken into account. To correct for CO_2 loss, we used a modified calculation based on the methodology of Riker (2005) and Wallace et al. (2015). A comparison of this method with results of experimental redissolution of CO_2 in shrinkage bubbles and Raman spectroscopic determination of CO_2 densities in bubbles shows good agreement (Wallace et al., 2015; Aster et al., in

prep). First, we estimate the size of the vapor bubble at the time of eruption (Riker, 2005). This bubble volume is formed as the result of cooling-induced crystallization (PEC) and melt contraction as a function of the change in temperature between entrapment and pre-eruption (ΔT). We use the phase equilibria of the most primitive melt inclusion compositions calculated with rhyolite-MELTS (Gualda et al., 2012) and the volume and thermal expansion data for silicate melts (Lange and Carmichael, 1990) and olivine (Kumazawa and Anderson, 1968; Suzuki, 1975) to derive an equation for the Cinder Cone magmas:

$$\text{Bubble volume } \% = 0.0092 \ \Delta T. \qquad \qquad \text{Equation (1)}$$

For each individual melt inclusion, we used Petrolog 3.1 to estimate the ΔT and then equation (1) to estimate bubble volume %. Melt inclusions that did not contain a vapor bubble were excluded from this correction. Although the absolute temperatures calculated with Rhyolite-MELTS (Gualda et al., 2012) and Petrolog 3.1 (Danyushevsky and Plechov, 2011) are different, the ΔT calculated for each MI from the two methods is similar (Aster et al., in prep).

With this estimate of the pre-eruption bubble volume %, the pre-eruption temperature, and the dissolved H_2O and CO_2 concentrations of each inclusion, we used the VolatileCalc program (Newman and Lowenstern, 2002) to determine the pressure of entrapment and the mol% CO_2 in the equilibrium vapor phase. We then used the Redlich-Kwong equation of state to determine the molar volume of CO_2 in the vapor bubble. The results of the CO_2 restoration calculations suggest that 25-78% of the initial dissolved CO_2 in the MIs at the time of trapping was lost to vapor bubbles during post-entrapment crystallization. Corrected concentrations of CO_2 are shown in Figure 4.6.

The H_2O contents of MIs can also be modified after entrapment. Experimental studies have shown that at magmatic temperatures, olivine hosted MI can lose nearly all of their H_2O in hours to days via H^+ (proton) diffusion, depending on temperature (Gaetani et al., 2012; Bucholtz et al., 2013). To investigate whether some MI from Cinder Cone had lost H by diffusion, we compared S/K_2O and H_2O/K_2O ratios, because correlated low values would indicate that lower H_2O values in the MI were the result of degassing of the melt before it was trapped (e.g., Johnson et al., 2010). However, the inclusions show variable H_2O/K_2O with a more restricted range of S/K_2O, and this suggests the H_2O variations may be the result of variable diffusive loss. For this reason, we cannot employ the methods described in Lloyd et al. (2013) to infer original H_2O contents. Thus, to correct for post-entrapment H loss by diffusion, we assumed that all melt inclusions initially had H_2O/K_2O values similar to that of the highest measured value. This correction procedure should yield the maximum likely initial H_2O content for each inclusion. Melt inclusions that have >1 wt% K_2O were not corrected for H-loss by diffusion because they likely experienced crustal contamination, and may have been trapped more shallowly after some degassing of H_2O.

Trapping pressures for the restored H_2O and CO_2 concentrations were calculated using solubility relations of Iacono-Marziano et al. (2012) and Papale et al. (2006). The two methods gave similar trapping pressures, with values ranging from ~2-4.2 kbar for the corrected MI (Fig. 4.6). These estimates are nearly 2 kbar higher than those estimated from measured dissolved H_2O and CO_2 contents. Assuming an average crustal density of 2.6 g/cm^2, these pressures represent entrapment depths of ~7-15 km below the surface. Three melt inclusions did not contain vapor bubbles and were trapped more shallowly

74

(<2 kbar). Corrected melt inclusions fall more closely along open- or closed-system degassing paths (Fig. 4.6), indicating that they may have been trapped at a range in pressures, but this could simply be an artifact of our assumption of initially constant H_2O/K_2O values (cf., Lloyd et al., 2012).
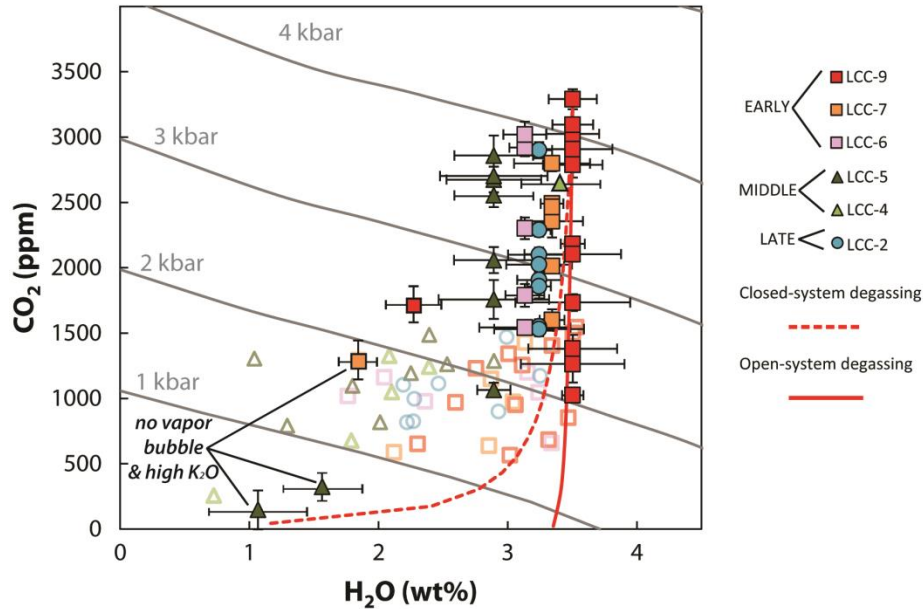
Figure 4.6. Melt inclusion corrected H_2O vs. CO_2. H_2O wt% and CO_2 ppm for corrected (filled symbols) and measured/uncorrected (open symbols) MI, as described in the text (Supplementary Tables C.1 and C.2). Inclusions without vapor bubbles do not require this correction and were trapped at lower pressure. Isobars calculated using methods of Papale et al., (2006) for an average melt inclusion composition. Open and Closed system degassing paths calculated using the VolatileCalc program (Newman and Lowenstern, 2002). Error bars are one standard deviation.

4.5.5. Trace Element Concentrations

Melt inclusions at Cinder Cone have typical calc-alkaline, subduction-related trace element patterns that are enriched in large ion lithophile (LILE) and light rare earth (LREE) elements relative to high field strength elements (HFSE) like Nb and Ta (Fig. 4.7). MI from late erupted units have higher concentrations of highly incompatible

elements than early erupted MI (Fig. 4.7). MIs from transitional units that have elevated SiO_2 and alkalis are even more enriched in highly incompatible elements such as Sr, Ba, U, and Pb (Fig. 4.7).
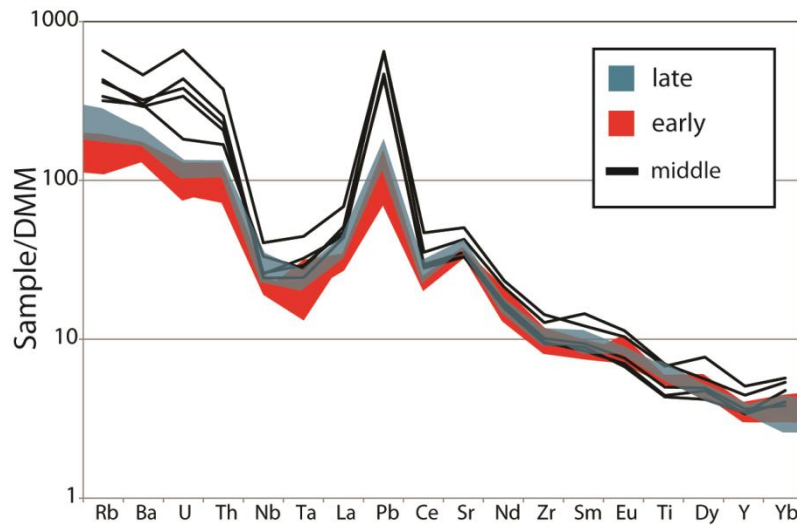
Figure 4.7. Spider diagram of average melt inclusions compositions. MI trace element compositions corrected for PEC and normalized to depleted MORB mantle (DMM; Workman and Hart, 2005). Blue and red shaded regions show the range in trace element compositions for late- and early-erupted tephra, respectively. Black lines represent individual melt inclusions from LCC-4 and LCC-5 that have higher SiO2 contents to highlight trace element enrichments seen in these units.

4.6. Discussion

4.6.1. Crustal Contamination at Cinder Cone

The major element compositions of most MIs have distinctly lower SiO_2 than the lava and bulk tephra at Cinder Cone. This observation suggests significant chemical evolution of the magma after olivine growth and melt inclusion entrapment. The ubiquitous presence of quartz xenocrysts in the tephra and lava suggests that this evolution was dominantly the result of crustal contamination. Partially melted and/or

vesiculated granitic clasts in the lavas (M. Clynne, unpublished data) likely represent the source of the abundant quartz xenocrysts and rare K-feldspar xenocrysts.

Figure 4.8 shows the results of mixing calculations between the low-SiO_2 melt inclusion compositions and high-SiO_2 compositions of the granitic xenoliths. Bulk tephra and lava compositions fall along mixing lines between magma batch 1 (early-erupted MI) and magma batch 2 (late-erupted MI) and the average granitic xenolith composition. Early erupted PD lava and tephra can be produced by 10-35 wt% assimilation of granitic basement by magma batch 1 (Fig. 4.8). Late erupted FL lava and tephra can be produced by 15-30% assimilation of granitic basement by magma batch 2 (Fig. 4.8). Rare mafic enclaves in the late-stage FL lava flows are similar in composition to the LCC-2 MI compositions (M. Clynne, unpublished data), providing further evidence that the MI represent the parental magma compositions. Unit 1 tephra, associated with the eruption of the Old Bench lava flows, is compositionally similar to mildly contaminated early-erupted Unit 2 tephra (which contains uncontaminated MI – samples LCC-9, LCC-7, and LCC-6).

Melt inclusions from LCC-5 have TiO_2 values that are more similar to the early-erupted units or that fall along mixing lines with the early-erupted units. MI from LCC-4, conversely, have TiO_2 contents more similar to the late-erupted tephra. These associations are consistent with our interpretations of the tephra stratigraphy, which suggest that LCC-5 represents the final, waning phase of Unit 2, whereas LCC-4 is the opening phase of Unit 3 (Fig. 4.2). LCC-5 also has the largest number of MIs that have contaminated compositions, and which are similar to the lava flows and bulk tephra. This may be related to the slowing of the eruption, which lead to shallow crystallization as the

77
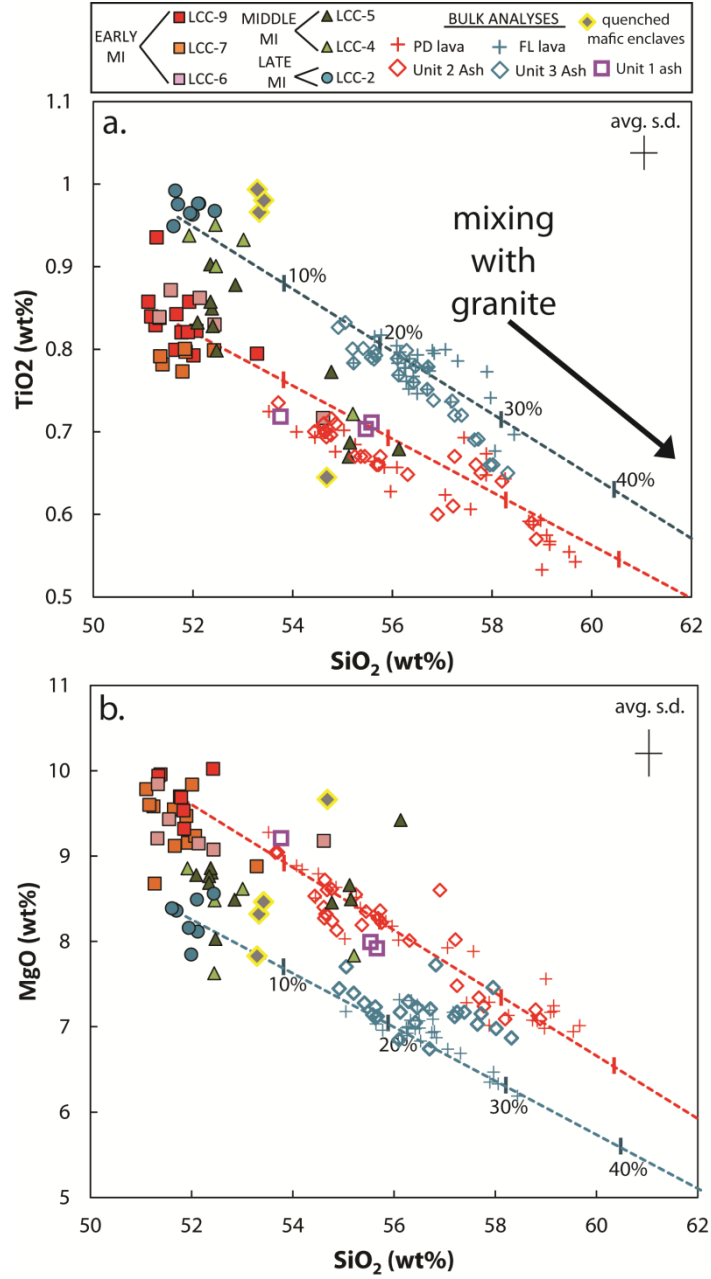
Figure 4.8. Modeled mixing with granitic xenoliths. SiO_2 vs. a) TiO_2 and b) MgO comparing MI compositions (normalized on a volatile-free basis; filled symbols) and lava, bulk tephra, and quenched mafic enclaves (M. Clynne unpublished data). Curves represent bulk mixing between granitic xenolith compositions (M. Clynne unpublished data) and average composition of batch 1 (early-erupted MI; red dashed curve) and batch 2 (late-erupted tephra; blue dashed curve) parental magmas, see text for details. Tick marks represent increments of 10% bulk addition of granitic material. Average analytical uncertainty in upper right hand corner of each panel (see Supplementary Table C.1).

78

first eruptive phase came to a close. This slowing or waning of the first eruptive phase is evidenced by increased groundmass crystallinity seen in the transitional tephra clasts (Marks, 2012).

Further evidence for assimilation of granitic basement is provided by the trace element compositions of MIs. Figure 4.7 shows that MI with elevated SiO_2, which are dominantly found in the transitional units, also have higher concentrations of incompatible trace elements, such as Pb, Ba, U. These incompatible trace elements are also found in high concentrations in the xenoliths and locally outcropping granitic basement rocks (Wolf Creek Granite; M. Clynne, unpublished data), the likely source of the xenoliths. The Li concentrations of the MIs appear to be particularly sensitive to the granitic contaminant, correlating linearly with Pb (Fig. 4.9), and clearly separating MI that have experienced contamination from those that did not.

4.6.2. Parental Melt Compositions

The olivine phenocrysts in the Cinder Cone tephra have compositions of $Fo_{88-90.8}$ and the host crystals for the MI range up to $Fo_{90.2}$. The upper end of the range of olivine compositions overlaps with olivine that would be in equilibrium with mantle peridotite. The trapping pressures of the MI, after accounting for CO_2 lost to vapor bubbles and possible H^+ losses, are in the range of 2 to 4.2 kbar, providing evidence that the host olivine crystallized in the middle crust. These observations require that either parental melts in equilibrium with the mantle ascended into the middle crust without fractionating,

or that mantle sources beneath the Lassen region are relatively refractory, with olivines $>Fo_{90}$.
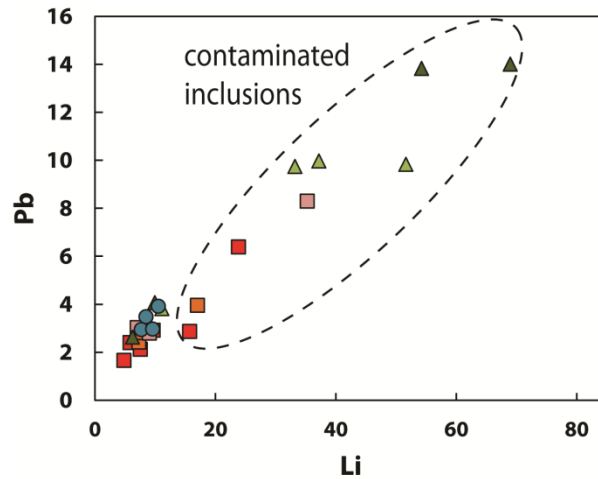
Figure 4.9. Melt inclusion Li vs. Pb corrected for PEC. High Li and Pb concentrations in MI are indicative of addition of granitic material, and highlight melt inclusions which sampled the contaminated magma. Errors can be found in Supplementary Table C.1. Same symbols as in Fig. 4.8.

Late-erupted MI from LCC-2 show distinct compositional differences when compared to early-erupted MI (Figs. 4.4 and 4.6), and are hosted in slightly less-magnesian olivine (Fo_{88}; Fig. 4.3), indicating that they could be related to the early-erupted magmas via crystal fractionation. We used Petrolog 3.1 and pMELTS (Ghiorso et al., 2002) to model equilibrium crystallization of the early-erupted magma at 4 kbar, the maximum trapping pressure estimated from the corrected CO_2 and H_2O contents (Fig. 4.6). Olivine is predicted to be the liquidus phase for the primitive batch 1 composition, but olivine crystallization alone cannot account for the decrease in CaO with decreasing MgO that is observed (Fig. 4.5). Because these basaltic magmas are ultimately derived from the mantle, they may have stalled near the base of the crust and undergone an episode of higher pressure crystallization before ascent into the crust. Pressures near the

Moho beneath the southern Cascades are ~10 kbar (~38 km; Mooney and Weaver, 1989) a pressure above which clinopyroxene may replace olivine as the liquidus phase in hydrous primitive basalts (e.g., Weaver et al., 2011; Blatter et al., 2013). Mass balance modeling suggests that ~5% high-pressure clinopyroxene fractionation may explain the observed major element differences between the two units (Fig. 4.5). However, phase equilibrium calculations with pMELTS at 10 kbar for the composition of the early-erupted magmas do not predict clinopyroxene as the liquidus phase, so we test this possibility further using the trace element compositions of the uncontaminated melt inclusions. Using equilibrium crystallization and partition coefficients between clinopyroxene and basaltic melt for La, Nb, Sc and Th, we model how the melt composition will change as the result of clinopyroxene fractionation. During clinopyroxene fractionation, Sc is compatible and should decrease rapidly in the melt, whereas Nb, Th, and La are incompatible, and should increase. For small amounts of olivine and/or clinopyroxene fractionation, Nb, Th, and La will only increase slightly and show little variability (Fig. 4.10 b, c, d). Figure 4.10 shows that 5% clinopyroxene can explain the variability in Sc and the relatively constant Th concentrations between early- and late-erupted units. However, the magnitude of Nb and La increases with decreasing MgO wt% cannot be explained by fractionation alone. Thus, we suggest small amounts of high-pressure clinopyroxene fractionation have likely affected the compositions of batch 2 parental magmas, but conclude this processes cannot account for the differences in trace element abundances between them. Because magma batches 1 and 2 are not related solely by fractional crystallization, either in the mantle or in the crust, their subtle

differences are likely the result of mantle processes, such as variability in mantle source

composition or the degree of melting.
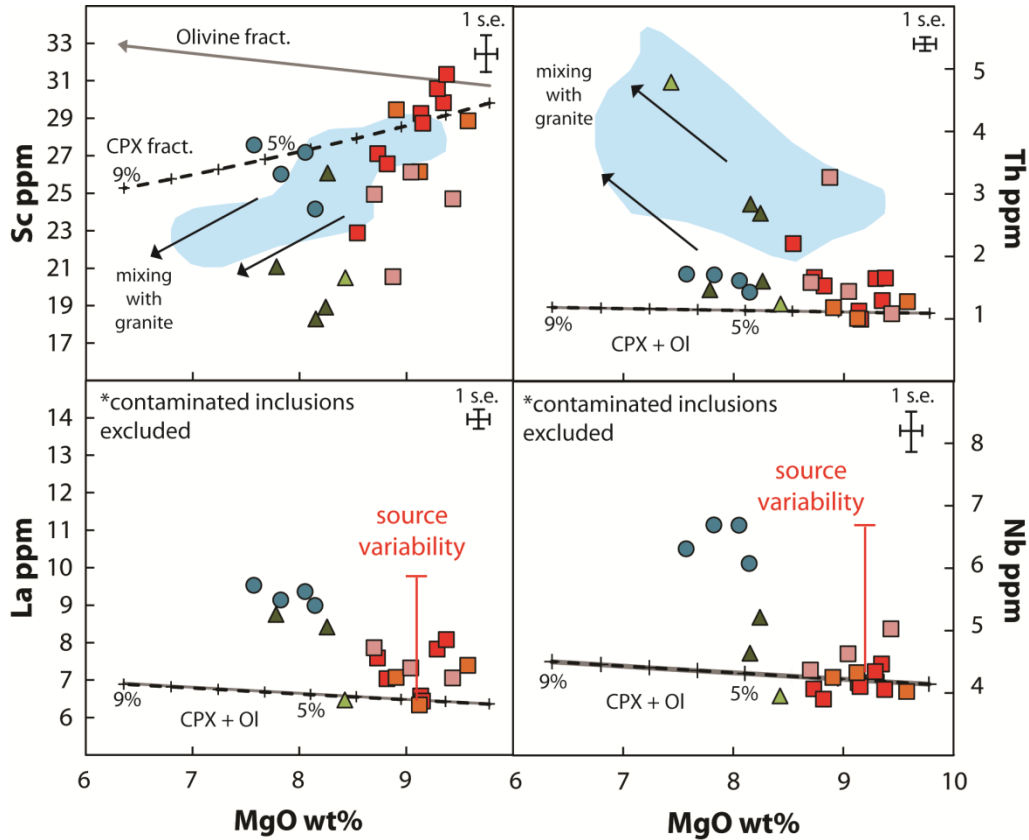
Figure 4.10. Melt inclusion MgO vs. trace elements. MgO (normalized on a volatile-free basis) vs. a) Sc, b) Th c) La and d) Nb (PEC corrected) compared with lava and bulk tephra (blue shaded region; M. Clynne unpublished data). Panels c) and d) exclude MI with elevated Li and Pb, and determined to be contaminated. Fractionation curves calculated using Petrolog 3.1. for MgO and the equilibrium crystallization equation and appropriate partition coefficients for trace elements for olivine (Ol, solid grey line) and clinopyroxene (CPX, dashed black line) with tick marks which represent 1% fractionation. Partition coefficients were taken from Paster et al., (1974; Sc, CPX-basalt), Beattie et al., 1994 (Sc, basalt-Ol, La, basalt-Ol), Hauri et al., (1994; Th., basalt-CPX, La, basalt-CPX, and Nb, basalt-CPX), and McKenzie and O'nions, (1991; Th, basalt-OL, and Nb, basalt-Ol). Average analytical uncertainty designated by symbol it top right corner of each panel. Same symbols as in Fig. 4.8.

Compositional variability amongst olivine phenocrysts can further be used to distinguish between early- and late-erupted parental magmas. Figure 4.3 shows the olivine Ni and Fo core compositions and reveals differences in early- and late-erupted units. LCC-9 has olivine phenocrysts cores with high Fo and a more restricted range in Ni when compared with the late erupted units. Late-erupted olivine cores follow a steep fractionation path (~2-3 % olivine fractionation) beginning with higher Ni, requiring either a more refractory mantle source or presence of mantle pyroxenite (Straub et al., 2011). The range in Ni of early-erupted olivine cores requires less than 1% fractionation of olivine. Interestingly, some olivine phenocrysts from LCC-9, the earliest eruptive phase, overlap with olivine from LCC-2 and LCC-4 (Fig. 4.3b). Given this similarity, it seems likely that the lower-Fo olivine in LCC-9 were derived by interaction of batch 1 and 2 magmas (the latter represented by LCC-2 or LCC-4).

It is important to note that although magma batches 1 and 2 are distinct, they are more similar to each other than to most other primitive basaltic magmas in the Lassen region (Fig. 11; Clynne, 1995; Borg, 1995; Walowski et al., 2015). Walowski et al. (in prep), show that most primitive magmas in the Lassen region are formed by variable amounts of slab component addition to a relatively heterogeneous mantle wedge. Figure 4.11 shows that early- and late-erupted magmas have similar values of Sr/Nd, indicative of similar amounts of subduction component addition (Walowski et al., in prep). Differences in Nb/Zr, however, suggest that late-erupted magma batch 2 may be derived from a slightly more enriched mantle source (Fig. 4.11). It is also possible that both batches were derived from the same mantle source, but separated and experienced different paths, down-temperature, through the upper-most lithospheric mantle. For

example, magma batch 2 may have reacted with pyroxenite veins in the uppermost lithospheric mantle, which could explain the elevated Ni contents in olivine compared to magma batch 1. Together, the observations demonstrate that monogenetic cones may tap different batches of mantle-derived melts during a single, short-lived eruption (Brenna et al., 2010, 2011; McGee et al., 2011). How these different magmas were tapped and where they were stored, however, requires further analysis.
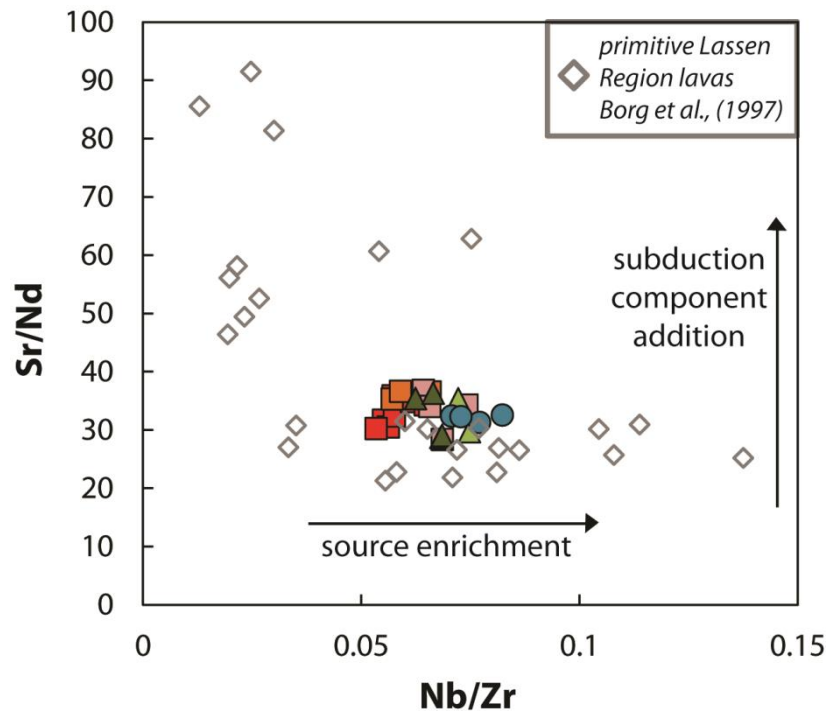
Figure 4.11. Comparison of Cinder Cone to Lassen region magmas. PEC corrected MI compositions of Sr/Nd and Nb/Zr compared with other primitive lavas in the Lassen Region (Borg et al., 1997). Symbol size for MI exceeds analytical uncertainty. Same symbols as in Fig. 4.8.

4.6.3. Timescales of Mixing and Ascent

Olivine phenocrysts from all units typically have broad, homogeneous cores, and Fe-enriched rims (Fig. 4.12). Because Ni is compatible in olivine and has a similar diffusivity (Petry et al., 2004), it displays a similar pattern to Fe/Mg in the Cinder Cone

olivine phenocrysts. These Fe-rich and Ni-poor rims were likely developed during crustal

contamination, magma mixing or entrainment of olivine in new batches of melt,

processes that could lower the Mg and Ni content of the bulk magma. Although some

new olivine growth may have occurred, we can use the diffusion timescales of trace

elements, such as Ni, to estimate a maximum timescale of olivine residence in an evolved

magma prior to eruption.

The effect of diffusion on the Ni concentration in an olivine crystal can be

calculated with Fick's second law, which describes the change in composition with time

over a one-dimensional system:

$$\frac{\partial c}{\partial t} = D \frac{\partial^2 c}{\partial x^2} ,$$
Equation (2)

where C is concentration, t is time, and D is the diffusivity. The above expression of

Fick's law assumes a constant diffusion coefficient, D, which for most natural systems is

an approximation. The diffusion coefficient for Ni in natural olivine, for example, varies

with temperature, pressure, oxygen fugacity and composition (Petry et al., 2004; Dohmen

& Chakraborty, 2007). We also assume that little to no olivine growth occurred during

the mixing event and as a result, our estimate will be a maximum timescale because

olivine growth is faster than Ni diffusion. The diffusion coefficient for Ni in the olivine

phenocrysts is assumed to be 2.6 x 10^{-16} m^2/s, taken from Petry et al. (2004) for a

temperature of 1200°C. For our boundary condition, we assume local equilibrium, that is,

the measured Ni content at the olivine rim is the equilibrium Ni content of the olivine

coexisting with the melt surrounding each olivine crystal. We also assume that the

average core composition is representative of the initial olivine core composition before

magmatic evolution (Fig. 4.12). To determine the best-fit diffusion curve, we calculated

diffusion profiles for a series of time-steps. The average of the two timesteps that were visually determined to best bracket the measured Ni concentration gradient at the olivine rim was used as the best timescale estimate (Fig. 4.12).
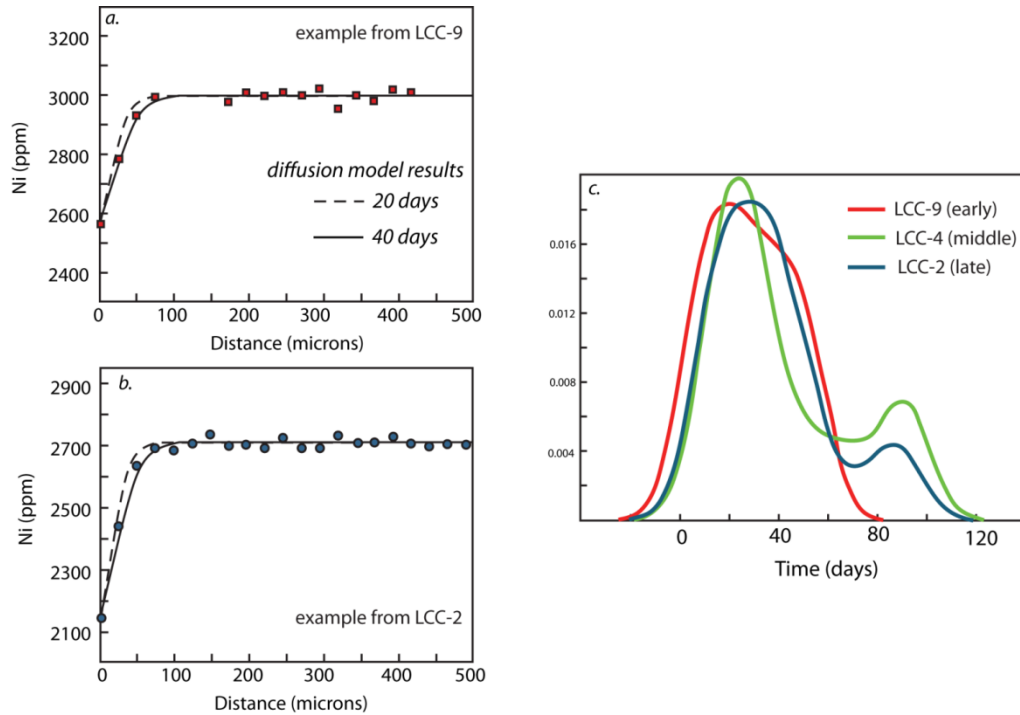
Figure 4.12. Ni diffusion in olivine. Panels a) and b) show examples of diffusion model results as described in the text. Data points represent measured core-rim Ni contents measured by LA-ICP-MS (symbols are the same as in Fig. 4.8). Model curves for 20 (black dashed curve) and 40 (solid black curve) days typically best fit the data. Panel c) shows a probability density function of average model timescales for 7 different olivine crystals from LCC-9, 6 from LCC-4, and 6 from LCC-2.

With these methods, we find that olivine phenocrysts from all units have an average residence time of 20-40 days. Some phenocrysts have longer apparent timescales, up to ~90 days, but uncertainty related to our model assumptions may cause this discrepancy for a few olivine crystals. The largest source of uncertainty in this method is derived from choice in temperature, and thus, diffusivity. Petrolog 3.1

86

estimates average trapping temperatures of ~1225°C and pre-eruptive temperatures of ~1150°C. This indicates that temperatures were decreasing during the mixing event, which is not captured by our model. Decreasing the temperature would result in longer timescales, however, our model also does not include olivine growth, which would decrease the timescale.

The calculated residence times at Cinder Cone are much more rapid than those calculated for olivine at Jorullo volcano in central Mexico (Johnson et al., 2008), which suggested olivine residence times of 200 to more than 1000 days. This is consistent with the total length of the eruption, as the eruption of Jorullo lasted for approximately 15 years (Luhr and Carmichael, 1985), whereas the Cinder Cone eruption probably lasted less than 1 year (Clynne et al., 2000, Sheppard et al., 2009). Differences between mixing and storage timescales and the eruption durations at Cinder Cone and Jorullo emphasizes the diversity of complex behaviors that can be displayed at monogenetic cones. Although there are large uncertainties associated with the calculated timescales, they still provide some constraints for the processes associated with magmatic evolution prior to the eruption of Cinder Cone. Importantly, our results demonstrate that the parental magmas mixed with granitic crustal material very rapidly prior to eruption.

4.6.4. Mechanisms of Crustal Contamination and Plumbing System Evolution

Although the role of crustal contamination in formation of the erupted magmas at Cinder Cone is clear, the mechanism by which this contamination occurred is more difficult to decipher. Determining how contamination occurred can provide constraints on how the magmatic plumbing system evolved prior to and during eruption.

87

Several, somewhat contradictory observations suggest two main hypotheses that may explain the contamination of the Cinder Cone magmas: 1) A shallow, strongly contaminated batch of magma, perhaps andesitic, was mobilized by and mixed with new batches of magma coming from depth, or 2) an initial batch of magma thermally pre-conditioned the granite, creating a zone of crystal- and xenolith-rich rhyolitic mush that was quickly incorporated into the rising new primitive magma batches. In hypothesis (2), there is no intermediate magma.

An important observation in support of hypothesis (1) is that granitic contamination is ubiquitous, but the amount of contamination is heterogeneous and changes throughout the course of the eruption. Specifically, Figure 4.13 shows the temporal evolution of the SiO_2 contents of the erupted tephra. For both eruptive phases, magmas start off more evolved (andesitic), and become progressively less contaminated over time. These temporal patterns in magma composition are similar to those observed during eruptive episodes 2-47 of Pu'u 'O'o in Hawaii (Garcia et al., 1992; Wallace and Anderson, 1998), and may indicate that a shallow, evolved magma batch was simultaneously mixed with and pushed out of the conduit system by the ascending mafic magma.

However, mineralogical or textural evidence for this contaminated magma seems to be lacking. Olivine xenocrysts with lower-Fo cores may be representative of the shallowly stored evolved magma. However, some of these xenocrystic olivine display low-Fo cores and high-Fo shoulders (Costa and Dungan, 2005), as well as low-Ni cores, high-Ni shoulders, and normally zoned rims, suggesting that they began to equilibrate with the primitive parental magma before crustal contamination occurred (Fig. 4.14).

88

Two xenocrysts from unit LCC-4 do not have high-Fo rims, and have

significantly lower Fo contents than the other xenocrysts, and may be representative of

the mixed magma (Fig. 4.14). Conversely, these same crystals may have grown in the

contaminated magma during the waning and transitional period of the eruption, as they

are only observed in the transitional unit, LCC-4. In addition, we did not analyze olivine

less than 250 μm in diameter, and there could be a population of low-Fo olivine derived

from the contaminated magma in this size fraction. None of the analyzed MI have low-Fo

olivine hosts.
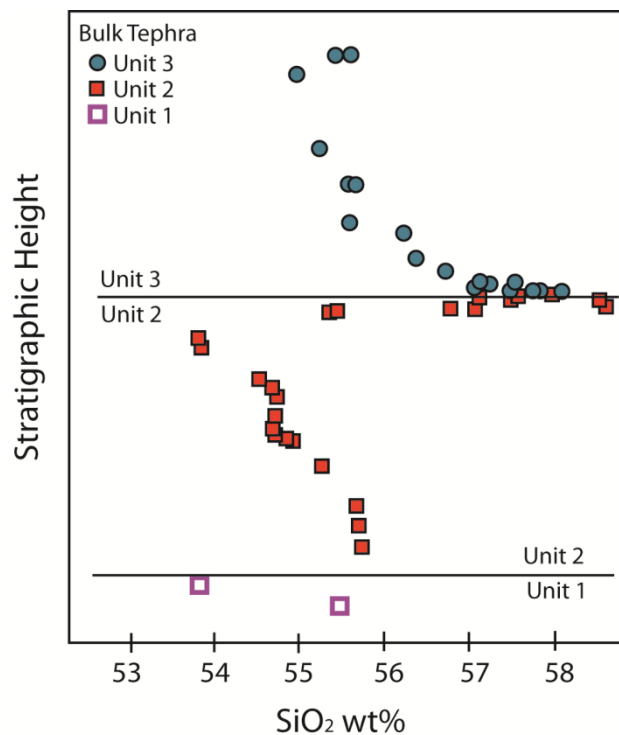
Figure 4.13. Temporal variability in bulk tephra compositions. All data in this figure is unpublished data from M. Clynne, and depicts how tephra compositions change over the course of the eruption at Cinder Cone. Unit transitions as defined by Heiken, (1978). The Unit 1is equivalent to Old Bench. The opening phase of Unit 2 is equivalent to LCC-9. The Unit 2-Unit 3 transition is equivalent to the transition between LCC-4 and LCC-5. Melt Inclusions were not samples from Unit 1.

89
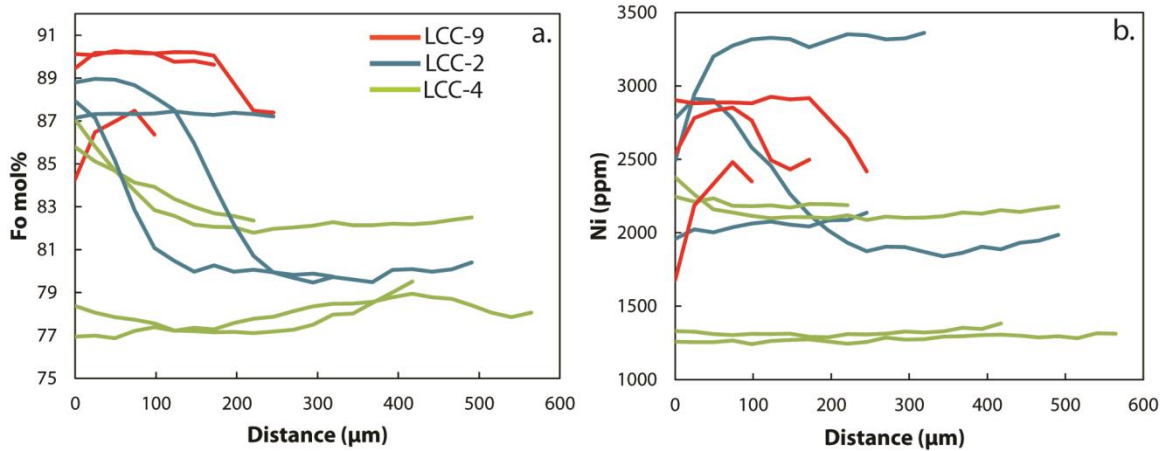
Figure 4.14. Core to rim variations in olivine xenocryts from LCC-9 (early-erupted; red), LCC-4 (transitional; green), and LCC-2 (late-erupted; blue) tephra.

In support of hypothesis (2), lava and bulk tephra fall on mixing trajectories between the granitic material and the two parental magma batches. If, for example, magma batch 2 evolved as the result of mixing with the first batch of contaminated erupted magma, one would expect mixing trajectories between magma batch 2 and the contaminated magma of early-erupted units, which is not observed.

Using the combined observations presented above, we suggest the following model for plumbing system evolution at Cinder Cone. First, one or several intrusions of batch 2 magma enter the middle crust and form a set of small sills, which may be partially integrated, over a range of depths. These batch 2 intrusions crystallize olivine, and have variable compositions and trapping depths as evidenced by fractionation trends in Fo vs. Ni (Fig. 4.3b). In a manner analogous to the model proposed by Grove et al., (1998) at Burnt Lava Flow, which involves the separation of heat and mass transfer, the mid-crustal sills quench on their margins, and become mechanically separated from the

surrounding granitic basement. However, the sills may transfer heat to the surrounding granitic wall rocks, causing them to variably melt or disaggregate. The shallowest sill or sills then become contaminated, where some MI with contaminated compositions and overlapping to lower trapping pressures are derived. Some of the unzoned xenocrysts may also be sourced from various parts of this sill complex, such as the Fo_{77-79} (Fig. 4.14), that produced highly contaminated magma.

Batch 1 magma then rises from the deep crust or mantle. It interacts at least partially with the existing sills because it samples olivine phenocrysts from batch 2 magmas, as suggested by Fo vs. Ni (Fig. 4.3b). A small portion of batch 1 magma interacts briefly with the partially melted granite or contaminated magma, and erupts as Old Bench lava flow and Unit 1 ash (these magmas are compositionally similar to early-erupted lava and tephra; Fig. 4.8). Most of batch 1 magma stalls when it interacts with the partially melted granite, mixing and crystallizing rims for 20-40 days. At this point, the entire system becomes destabilized, and eventually erupts, with the most heavily contaminated parts erupting first. As a result, the batch 2 sills also become destabilized, causing them to ascend, interact with heated and partially molten granite, crystallize lower Fo rims for !20-40 days, and finally erupt in a similar manner to the previously erupted batch 1 magmas.

4.7. Conclusions

The eruption of Cinder Cone produced a series of tephra deposits and lava flows that display complex changes in chemistry over the course of the eruption. High-Fo olivine phenocrysts from all erupted units contain melt inclusions that are more primitive

in composition than the erupted material. The evolved compositions of the lava and bulk tephra and the abundance of quartz xenocrysts within the deposits suggest the parental magmas were rapidly contaminated by granitic material in the middle to upper crust. The basaltic parental magmas sampled by the melt inclusions crystallized at minimum depths of 2-4.2 kbar, which equates to approximately 7-15 km below the surface. Distinct compositional variability between early- and late-erupted units suggest two different mantle-derived basaltic magmas were tapped during the eruption. These two basaltic compositions correlate with the two main explosive phases of the eruption, and were separated by an eruptive slowing or pause evidenced by textural analyses of tephra clasts (Marks, 2012). Diffusion modelling of Ni gradients in olivine rims suggests that olivine residence times in an evolving magma were on the order of weeks, shorter than those calculated for longer-lived cinder cone eruptions, such as Jorullo in Mexico. Temporal changes in lava and bulk tephra compositions indicate that the granitic material was heterogeneously incorporated after olivine growth and melt inclusion entrapment. Although the geochemical evidence suggests that the parental magmas were contaminated by either a shallowly stored evolved magma or a granitic mush, the exact mechanisms that drove crustal contamination of the Cinder Cone magmas remain enigmatic. Our combined results provide new insight into the complexities of short-lived monogenetic eruptions.

APPENDIX A

CHAPTER II SUPPLEMENTARY MATERIALS

A.1. Methods

Cinder cones were chosen based on their primitive compositions to ensure minimal contributions from crustal processes. At each cone, tephra deposits were sampled to guarantee rapid cooling of olivine phenocrysts, thus minimizing the diffusive loss effects that occur during slow cooling in lava flows. Olivine crystals ranging in size from 1 mm to 250 µm were hand-picked from washed and sieved tephra. Fifty olivine-hosted melt inclusions were analyzed for H_2O and δD by NanoSIMS at the Carnegie Institution of Washington. Olivine was polished on a single side to expose the inclusions (50-250 µm in diameter) and pressed into an indium mount along with basaltic glass standard grains, and gold coated for analysis (40 nm thick coat). Each inclusion was analyzed once with a 10 nA Cs+ primary beam (~2µm diameter) rastered over a 20x20 µm area. Ion images were used during pre-raster to verify homogeneity of the analyzed area and avoid beam overlap with surrounding olivine and vapor bubbles (if present).

NanoSIMS analysis of D/H ratios in glass generally followed the methods and standardization described in detail in Hauri et al. (2006) but with NanoSIMS instrument-specific modifications described here. We used a modified entrance slit of 60 µm width to maximize transmission of H and D ions, paired with a standard aperture slit (350 µm width). This combination resulted in a mass resolving power of ~1000; previous measurements[44] have shown that with good vacuum conditions and when using a Cs+

beam, H_2/D ratios are typically $<1.5 \times 10^{-3}$; this was verified at higher mass resolving power prior to beginning analyses, with measured $H_2/D \leq 1 \times 10^{-4}$. H and D were collected on a Faraday Cup and electron multiplier, respectively; we also collected ^{18}O using a Faraday cup. After presputtering and imaging to center the melt inclusion under the beam without overlap onto olivine and/or vapor bubbles (where present), each isotope was counted for one second per cycle, and we collected data over 300 total cycles for each analysis. Faraday Cup backgrounds were measured off-peak 20 times every 80 ratios with the primary beam and electron beam on. Including presputtering, imaging and measurement of signals and backgrounds, each analysis lasted approximately 15 minutes and produced an average precision of $\pm 3‰$ ($2\sigma M$). Data were collected over 4 days of analysis, and overall external reproducibility of the basalt glass standard GL07 D30-1 (1.5% H_2O) was $\pm 10‰$ (2σ, n=32). D/H data were examined for matrix effects using a two-collision cascade model described in detail in Hauri et al. (2006) but specific to the NanoSIMS; the total range of matrix effects from hydrous rhyolite to low-H_2O basalt on the NanoSIMS are reduced (40‰) compared with the 6F ion microprobe (60‰), and similarly it was found that for basaltic glass there are no resolvable matrix effects across the range of H_2O contents from 0.16 wt% to 2 wt% H_2O (cf. Fig. 2.3 of Hauri et al., 2006). Therefore we made no correction for matrix effects and simply corrected for the instrumental mass fractionation (IMF) as determined by repeat analyses of GL07 D30-1 basaltic glass standard. The average precision of the IMF correction ($\pm 6‰$ $2\sigma M$ of standards run on each day, including uncertainty on known D/H ratio of GL07 D30-1) was better than the overall external reproducibility; combining these uncertainties, we estimate the typical uncertainty on a single SIMS measurement (precision + accuracy) is

±12‰ (2σ). Simultaneous measurements of H_2O content were determined from the

measured $^1H/^{18}O$ ratio calibrated against the standard glasses described in Hauri et al.

(2006), with uncertainties of ±6% (2σ).

The same inclusions were subsequently analyzed for a suite of trace elements on

the Photon Machines Analyte G2 193 nm ArF ''fast''Excimer Laser system at Oregon

State University, using 50 μm spot size with a 5 Hz pulse rate. Measured trace element

concentrations were determined by reference to GSE-1G glass as a calibration standard

and using ^{43}Ca as an internal standard[45]. BHVO-2G, BCR-2G, and GSD-1G glasses were

also analyzed to monitor accuracy and precision, and the analyzed values were within

10% of accepted values.

A.2. Supplementary Discussion

Composition of the hydrous subduction component

The curves in Figure 2.2a show the compositions of melts that can be formed by

partial melting of the mantle wedge after variable amounts of a hydrous subduction

component have been added. A hydrous subduction component (fluid/melt released from

the slab into the mantle wedge) was mixed with a 10% partial melt of a depleted MORB

mantle (DMM; Workman and Hart, 2005) and a more enriched mantle (E-M; 66% DMM

and 33% enriched mantle; Donnelly et al., 2004), which reflect the range in relative

mantle enrichment of sub-arc mantle seen in the Lassen region (Supplementary Fig. A.2).

For the subduction component, we have used an H_2O/Ce ratio calculated for the central

Oregon Cascades (Ruscitto et al., 2010) using the method of Portnyagin et al. (2007), and

the value is consistent with the relatively high slab-surface temperature predicted from

geodynamic models (Ruscitto et al., 2012). Because the concentrations of P_2O_5 in the subduction component were not calculated by Ruscitto et al. (2010), we tried various values, together with their maximum Sr concentration, until we achieved a good fit to the data in Figure 2.2a. It is important to note that the absolute concentrations of elements in subduction components calculated using the Portnyagin et al. (2007) method are poorly constrained, as they result from summing the concentrations of all incompatible elements (as oxides) plus H_2O and Cl and then normalizing to 100%. The calculation does not include SiO_2 and many other major elements, so the concentrations of H_2O and incompatible trace elements would be quite different if the subduction component was a hydrous silicate melt rather than an aqueous fluid. As a result, the mass fraction of the subduction component added to the mantle along either of the curves in Figure 2.2a will substantially vary depending on the fluid vs. melt-like character of the component. However, the fraction of the total H_2O in the final silicate melt generated in the wedge that is contributed from the slab does not depend on this, and is a function only of the initial mantle composition and the H_2O/Ce content of the subduction component. For the Cascades, the latter is well constrained from both geochemical data and geodynamic models.

Calculation of slab surface temperatures

We use the H_2O/Ce slab surface geothermometer (Cooper et al., 2012) for comparison with temperatures calculated using a 2-D steady state thermal model (Wada and Wang, 2009). The H_2O/Ce ratio is a geochemical thermometer based on the solubility of the REE-bearing phosphate minerals monazite and allanite (Cooper et al.,

2012). These phases occur within the top-most sediment layers of the slab, making H_2O/Ce a potential thermometer of the slab surface. Basalt melting experiments at sub-arc slab pressures and temperatures suggest that allanite is also stable in basaltic oceanic crust (Kessel et al., 2005; Klimm et al., 2008; Plank et al., 2009), and that its presence in experimental run products is not an artifact caused by REE doping of the experiments (Klimm et al., 2008). Our model for wet melting of upper oceanic crust basalt provides a mechanism for re-equilibration of the more deeply sourced, trace element-poor fluids derived from serpentinized mantle in the downgoing plate, with an allanite-bearing basaltic crust. Although there is uncertainty as to the melt fractions at which allanite is exhausted from the residue during wet melting of basalt, the slab surface temperatures calculated using the H_2O/Ce ratio are in agreement with the thermal model temperatures. If re-equilibration of the mantle-serpentinite-derived fluids with a REE-bearing phase did not occur, then apparent H_2O/Ce temperatures would be much lower because serpentinite derived fluids are H_2O rich and trace element poor. It should be noted, however, that our model and interpretations are based on the slab surface temperatures derived from the 2-D steady state thermal model and do not rely on the correctness of the H_2O/Ce temperatures.

In the H_2O/Ce temperature calculation, we assume that fluid and/or melt migration from the slab and into the mantle wedge are vertical. However, recent work has shown that fluids may migrate updip at the slab-mantle interface (if fluids are mobile) and within the slab (if a permeability barrier exists at the interface) and also down-dip with the subducting slab or the flowing overlying mantle (if fluids are relatively immobile). The details of fluid migration paths predicted by currently available fluid

97

migration models (e.g., Wilson et al., 2014, Cagnioncle et al., 2007, Iwamori 1998, 2007)

vary widely, depending on the specific problems that are being investigated (e.g., some

combination of the effects of compaction, grain size, fluid availability, and melting) and

the assumptions and material properties used in the model. However, if lateral fluid

migration was taken into account, the effects would not change our general conclusions.

First, if up-dip flow was occurring (Wilson et al., 2014), then the fluids would be need to

be sourced from the slab down-dip of the arc. However, the thermal models predict that

no water remains in the slab past the arc. If metastability of hydrous minerals was

allowing water to be carried by the slab deeper than the arc, then the final stages of

chlorite breakdown would be occurring slightly down-dip of the arc, and the fluids rising

up-dip through the slab would have low D/H values. Second, in models that consider

lateral migration of fluids through the wedge once they are released from the slab

(Cagnioncle et al., 2007), the nature of the mantle wedge flow field controls the

migration. Initially, as fluids leave the slab-mantle wedge interface, they migrate in a

direction away from the arc trench because of down-dip flow of the wedge. But as the

fluids rise and trigger melting and the melts migrate through the upper part of the wedge,

the flow is directed back towards the trench because of the pattern of corner flow. Thus,

the two components of lateral migration partially offset each other. For most values of

wedge permeability, slab dip, and covergence velocity, there is a small net migration of

fluids and melts away from the trench (Cagnioncle et al., 2007), implying that arc

magmas will inherit a slab signature from a region of the slab that is slightly up-dip of the

region that lies directly beneath the arc. Overall then, the effects of some up-dip fluid

flow within the slab and lateral migration within the mantle wedge should partially offset

98

each other. For these reasons, we have chosen the zeroth-order assumption that fluid flow is simply vertical, and this is a good starting point from which further studies and modeling efforts can depart.

For both models, we also choose to exclude the latent heat of fusion during slab melting. Assuming a 10% partial melt of the slab, the latent heat of fusion may cool the system by ~50°C. However, the type of discrepancy between H_2O/Ce and geodynamic model temperatures that we find for the southern Cascades (Fig. 2.2) does not occur for the central Oregon Cascades (Ruscitto et al., 2010, and our new unpublished modeling), where a very similar thermal structure should also lead to slab melting. The small offset between the model temperatures predicted for the southern Cascades and the lack of offset for central Oregon is precisely what Cozzens et al. (2012) predicted should occur based on fluid flow modeling and heat flow measurements. We thus think it is a better explanation for the small discrepancy between H_2O/Ce and geodynamic model temperatures in the southern Cascades. Given that the effect of including the latent heat of fusion is relatively small and that other secondary factors that could cause similar small increases or decreases in model temperatures have yet to be included in geodynamic models, we have chosen not to try to incorporate this into our modeling.

Hydrogen diffusive loss corrections

Supplementary Figure A.3 shows the H diffusion loss corrections made for each sample using the diffusive re-equilibration model from Bucholz et al., (2013). Melt inclusion data for each cinder cone are shown in a panel with a histogram and a bivariate plot. Each histogram shows the H_2O concentrations (wt%) measured by FTIR for a larger

set of melt inclusions (Walowski and Wallace, unpublished data) than were analyzed by

NanoSIMS. Each panel also shows δD versus H_2O (wt%) in melt inclusions measured by

NanoSIMS (Supplementary Fig. A.3). The curves show diffusion model results. For each

cone, the curves start at the maximum H_2O concentration (defined as the average of the

highest 3-5 measured inclusions from the larger FTIR dataset), because these values are

assumed to be most representative of the starting, undegassed magma and are therefore

used as the starting value for the diffusive re-equilibration model. Model envelopes

represent variability in melt inclusion and host olivine size, both of which affect the

efficiency of diffusive loss. Starting δD for each model curve was varied in increments of

10‰ (colors shown in panel 1) to find model envelopes that best reproduced the

measured data points. The initial δD values shown in Figure 2.3a are the average of the

starting δD curves that fit the data, and uncertainties are reported as the upper and lower

limits of the starting δD values. Model corrections produce more negative values than are

measured at each cone. However, it is important to note that if the diffusion correction

was not performed and the lowest measured Lassen values were used to represent initial

δD, the values would still be distinctly more negative (isotopically lighter) than those

measured in the Marianas.

D/H Fractionation Model Calculations

The D/H fractionation model calculates the δD of the fluids released from the

downgoing slab using an equilibrium fractionation equation from White (2005),

$$\Delta = \left(1 - \frac{1}{(1-f)/(\alpha-f)}\right) * 1000$$
(Equation 1),

100

where Δ is the difference in the δD of the residual material (or solid) from the initial δD of the starting material, f is the fraction of H_2O remaining in the solid after the reaction, and α is the fractionation factor. Once calculated, Δ is used to then calculate the δD of the residual slab (solid) as,

$$\delta D solid = \delta D initial + \Delta \qquad \text{(Equation 2)}.$$

Because the system is assumed to be in equilibrium, we can then use the definition of alpha,

$$\alpha = (\delta D solid + 1000) / (\delta D fluid + 1000) \qquad \text{(Equation 3)},$$

to calculate the δD of the fluid as,

$$\delta D fluid = ((\delta D solid + 1000) / \alpha) - 1000 \qquad \text{(Equation 4)}.$$

The fraction of H_2O remaining in the slab, *f*, was calculated by adopting the approach developed by Wada et al., (2012). We use a generic lithologic model and initial bulk H_2O concentrations as described in Hacker (2008) and assume localized hydration in the incoming oceanic plate (as opposed to uniform hydration; Wada et al., 2012). For the Lassen Region, we use an incoming plate age of 8 Ma, a maximum depth of decoupling of 75 km, and 2 km thick hydrated upper mantle, while in the Marianas case we assume a 4 km thick hydrated upper mantle (for other thermal model parameters, see Wada and Wang, 2009, for the Cascades and Marianas). The modeling results for .the distribution of H_2O remaining in the slab are shown for the Lassen Region (Fig. 2.3b) and the Marianas (Supplementary Fig. A.4). These results are consistent with calculations from Van Keken et al., (2008). The starting δD values, $\delta D_{initial}$, were based on measured values of natural samples for MORB and gabbro (-50‰; Agrinier et al., 1995) and serpentine in

mantle peridotite (-60‰ to -40‰; Barnes et al., 2009; Alt and Shanks, 2006). The

fractionation factor, α, is calculated using a series of experimentally derived factors of

important hydrous phases found in the slab lithologies (Supplementary Fig. A.5).

Uncertainty in starting δD values (±10‰) and fractionation factors (Supplementary Fig.

A.5) result in an approximate error of ±15‰ (2σ) after propagation.

Previous work, dominantly in the Nicaraguan Arc, has provided evidence for the

hydration of the deep slab (oceanic peridotite up to ~20km depth; Ranero et al., 2005),

and the role of these fluids during the production of arc magmas (Barnes et al., 2009).

Furthermore, our model yields predictions that are very similar to values calculated for

fluids in equilibrium with exhumed chlorite-bearing harzburgites from Cerro del Almirez,

Spain, that have been interpreted to represent subducted oceanic peridotite. Alt et al.

(2012) calculated that fluids in equilibrium with these chlorite-bearing harzburgites at

700°C had δD values that ranged from -65 to -27‰. This calculation employed the same

fractionation factors used in our study (Graham et al., 1984b, Graham at el. 1987), and

our methodologies only differ in that we model progressive dehydration. In our model for

the Cascades, 700°C is reached in the hydrated upper mantle portion of the slab when the

slab surface is at ~60-65 km depth, at which point we predict δD of fluids released from

chlorite-bearing harzburgite to be -55 to -30‰, overlapping values from Alt et al. (2012).

However, because fractionation becomes more extreme as H_2O concentrations decrease

in the peridotite at higher temperatures, large variations in δD in the released fluids occur

over a relatively small range in temperature. Our temperatures in the subducted mantle

beneath the arc are ~770°C, producing fluids with δD values that range from

approximately -100 to -80‰, which overlap with Cascade melt inclusion values.

Large-scale hydrogen isotope fractionation during fluid and/or melt transport

Hydrogen isotope fractionation could potentially occur by diffusion as fluids and/or melts migrate through the slab and wedge. Indeed, this is the large-scale equivalent of the process we observe and correct for in the melt inclusions (post-entrapment H loss). But the significance of this process on the large scale is entirely dependent on whether the H_2O flux is dominantly diffusive or dominantly advective. We postulate that veining within exhumed terrains that represent subducted oceanic lithosphere (John et al., 2008; 2012) is evidence for dominantly advective fluid flow within the slab and superjacent mantle wedge, and so, in our model we ignore diffusion during large-scale dehydration of the slab. Fluid and melt transport within the mantle wedge are also likely to be dominated by advective flow (Wilson et al., 2014, Cagnioncle et al., 2007, Wada et al., 2012).

Sr isotope evidence for slab melting

In many arcs, basaltic magmas have variably elevated $^{87}Sr/^{86}Sr$ ratios that have been interpreted to result from subduction recycling of seawater-derived Sr (e.g. DePaolo and Wasserburg, 1977). However, in the southern Cascades, we observe negative correlations between $^{87}Sr/^{86}Sr$ and subduction component indicators, opposite of what is commonly observed in arcs (Supplementary Fig. A.6). The trend for the southern Cascades requires a subduction component with unradiogenic $^{87}Sr/^{86}Sr$ (Borg et al., 1997), which we suggest may be derived from partial melting of the downgoing basaltic crust. This interpretation relies on the observation that oceanic crust is heterogeneously

altered during hydrothermal alteration (e.g., Bach et al., 2003). Hydrous phases that form during this alteration should acquire elevated $^{87}Sr /^{86}Sr$ values, whereas unaltered portions should retain a MORB-like signature. Because hydrous phases are exhausted at the eclogite transition, before the plate reaches subarc depths beneath the Cascades, much of the radiogenic Sr that was added to the oceanic crust by hydration will likely be lost to the forearc mantle wedge. Fluids from serpentine and chlorite dehydration within the slab interior should have a seawater Sr-isotope signature, but are solute poor, and as a result have little leverage when mixed with more Sr-rich, unradiogenic, partial melts of eclogites (Spandler et al., 2014; Klimm et al., 2008).

Supplementary Table A.1. Bulk Tephra Analyses

Sample	BBL-05[MI]	BORG-1	BPB-1	BAS-44-02	BPPC-01	BRVB-01	Cinder Cone[MI]
Lat (N)	40°34'33.72"	40°39'15.63"	40°40'40.80"	40°37'50.64"	40°19'34.22"	40°31'48.78"	40°32'24.50"
Long (W)	121°37'1.32"	121°13'29.07"	121°12'51.00"	121°20'40.14"	121°54'38.64"	121° 4'34.32"	121°18'37.00"
wt%							
SiO_2	49.76	49.29	52.44	50.04	51.83	50.38	51.85
TiO_2	1.04	0.64	0.92	1.00	0.82	1.32	0.83
Al_2O_3	17.27	15.48	17.16	17.80	16.78	16.86	16.61
FeOt	9.38	8.54	7.65	8.88	7.68	9.39	6.88
MnO	0.14	0.15	0.14	0.16	0.15	0.16	0.09
MgO	8.38	8.05	8.76	9.01	9.14	8.65	9.68
CaO	10.34	8.50	9.35	9.92	10.60	9.24	10.02
Na_2O	3.14	2.07	2.69	2.67	2.56	2.90	3.05
K_2O	0.37	0.40	0.71	0.36	0.34	0.84	0.84
P_2O_5	0.18	0.10	0.19	0.16	0.10	0.27	0.15
CO_{2max} *(ppm)*	856	1199	614	721	1010	570	1138
H_2O_{max}	1.33	3.30	3.23	1.17	2.44	2.67	3.46
Olivine Fo content*	85.13	88.20	86.48	87.71	87.32	84.45	89.84
ppm							
La	7.62	5.54	11.70	8.75	6.30	14.06	7.46
Ce	18.6	13.2	25.7	21.2	15.1	32.0	16.9
Pr	2.60	1.82	3.49	3.03	2.18	4.44	2.31
Nd	11.9	8.16	14.8	13.3	9.77	19.2	10.5
Sm	3.35	2.20	3.51	3.40	2.67	4.58	2.41
Eu	1.18	0.76	1.14	1.17	0.95	1.48	0.80
Gd	3.93	2.29	3.48	3.63	3.04	4.58	2.47
Dy	4.60	2.48	3.41	4.12	3.45	4.46	2.55
Er	2.81	1.39	1.88	2.46	2.12	2.42	1.39
Yb	2.66	1.31	1.68	2.27	1.95	2.12	1.39
Ba	146	154	309	151	125	337	202
Th	1.47	1.07	1.90	1.08	0.69	1.83	1.63
Nb	3.87	2.48	5.61	3.11	1.81	7.06	4.03
Y	24.6	12.9	17.5	22.0	18.9	22.9	13.1
Hf	2.63	1.61	2.53	2.33	1.83	2.91	1.73
Ta	0.25	0.17	0.37	0.20	0.12	0.45	0.26
U	0.44	0.33	0.57	0.34	0.23	0.55	0.52
Pb	3.32	2.48	3.84	2.66	1.89	3.44	3.22
Rb	8.68	7.40	14.60	7.24	6.25	16.03	15.39
Sr	186	362	464	411	461	459	342
Sc	41.4	28.8	30.2	36.7	36.0	30.1	27.1
Zr	104	60.1	98.5	89.3	67.2	114	70.9

MI – Values represent average of the most primitive measured melt inclusion compositions because bulk tephra analyses were not available

*Average Fo content of all host-olivine of analyzed melt inclusions

Sample names are abbreviations based on Clynne and Muffler (2010): BBL = Basalt of Big Lake; BORG = Basalt of Old Railroad Grade 3; BPB = Basalt of Poison Butte 3; BAS-44 = Basalt of Highway 44; and unpublished locations: BPPC = Basalt of Paynes Creek Parasitic Cone; BRVB = Basalt of Round Valley Butte.

Locations are based on NAD27 datum used in Clynne and Muffler (2010). Additional geochemical data for most samples can be found in Clynne et al. (2008); Borg et al. (1997, 2002, 2000); Clynne (1993).
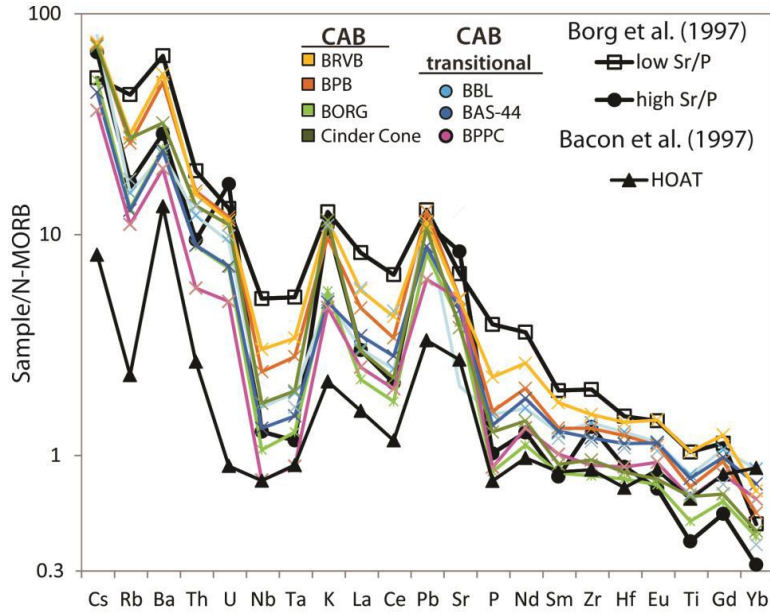
Supplementary Figure A.1. Bulk tephra trace element compositions. Trace element compositions from bulk tephra of analyzed cones in the Lassen Region compared to previously published endmembers. Low and high Sr/P represent endmember CABs with variable amounts of a subduction component (Borg et al., 1997). The high-alumina olivine tholeiite (HAOT, sometimes called low-K tholeiites; Bacon et al., 1997) is an endmember composition of tholeiitic magmas from the Lassen region, associated with normal faulting in the back-arc, which are not influenced by subduction enrichment. Although some magmas used in this study have low K2O, they are more enriched with respect to incompatible trace elements than the HAOT magmas, indicating that they are enriched by a subduction component.
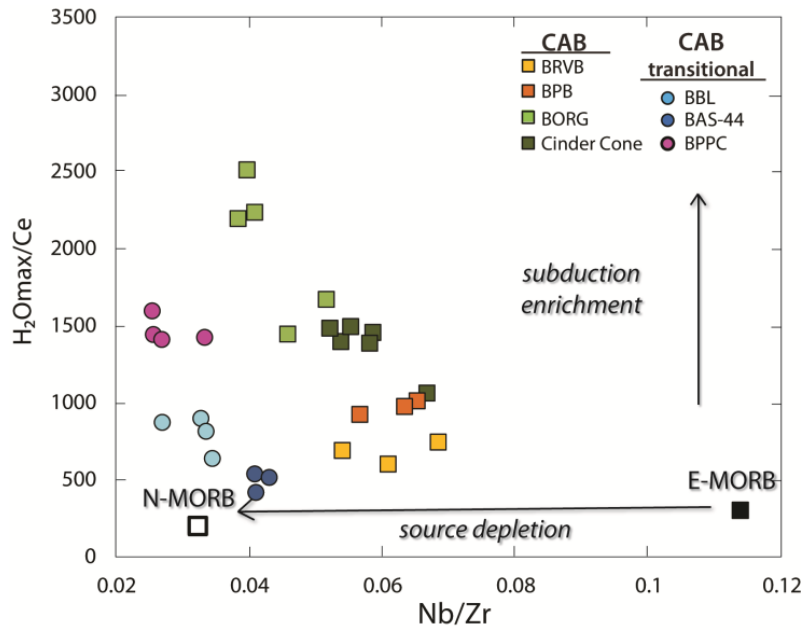
Supplementary Figure A.2. Relative source depletion and subduction enrichment Nb/Zr versus H_2Omax/Ce showing the relative depletion of the source mantle (N-MORB and E-MORB; Sun and McDonough, 1989; Michael, 1995) of the samples and effects of subduction enrichment. The relative depletion of the mantle source seen in this figure is used as the basis for calculating a range in starting mantle components used in Fig. 2.2a and discussed in the Supplementary Materials. This figure also highlights that increased addition of a slab component results in higher H_2O/Ce (and therefore $(Sr/P)_N$) and in conjunction, creates source variability and across-arc trends seen in the Lassen region primitive basalts.
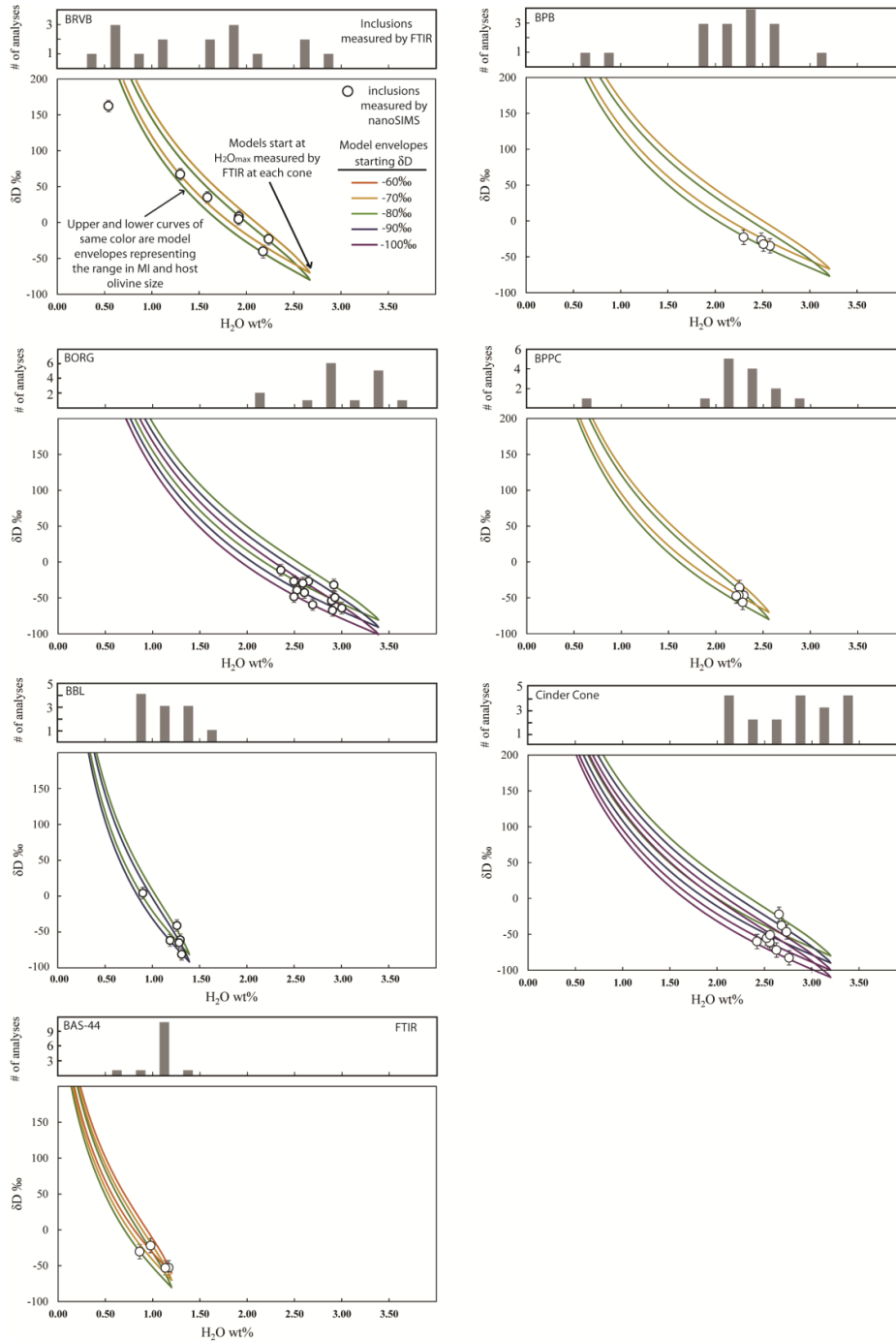
Supplementary Figure A.3. Corrections for effects of diffusive loss from melt inclusions for each cone using the model of Bucholz et al., (2013). A panel for each cinder cone contains a histogram (H_2O concentrations measured by FTIR from a larger set of inclusions) and a bivariate plot of δD versus H_2O. Open circles are individual melt inclusions measured by NanoSIMS, and colored curves are diffusion model results (color based on starting δD shown in panel 1). The starting point for each model, H_2Omax, represents the average of 3-5 melt inclusions with the highest H_2O measured by FTIR.
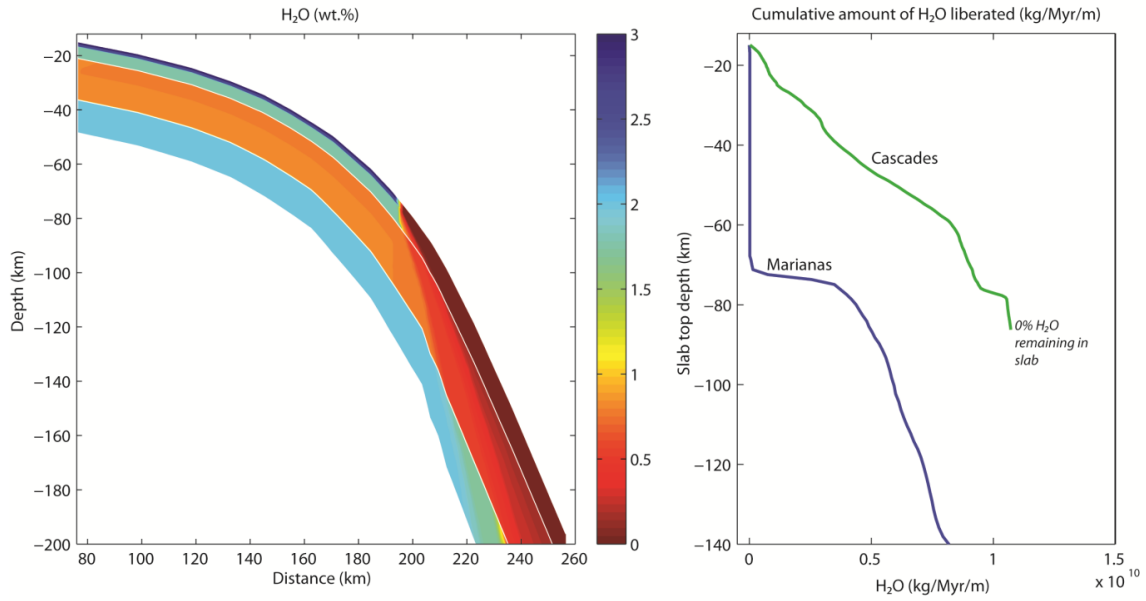
Supplementary Figure A.4. a) Model results showing the distribution of H_2O remaining in the downgoing slab for the Marianas Arc and **b)** the cumulative H_2O released from the slab for both the Marianas and the Cascade Arc. Hydration of incoming plate is based on those previously used in Wada et al., (2012).
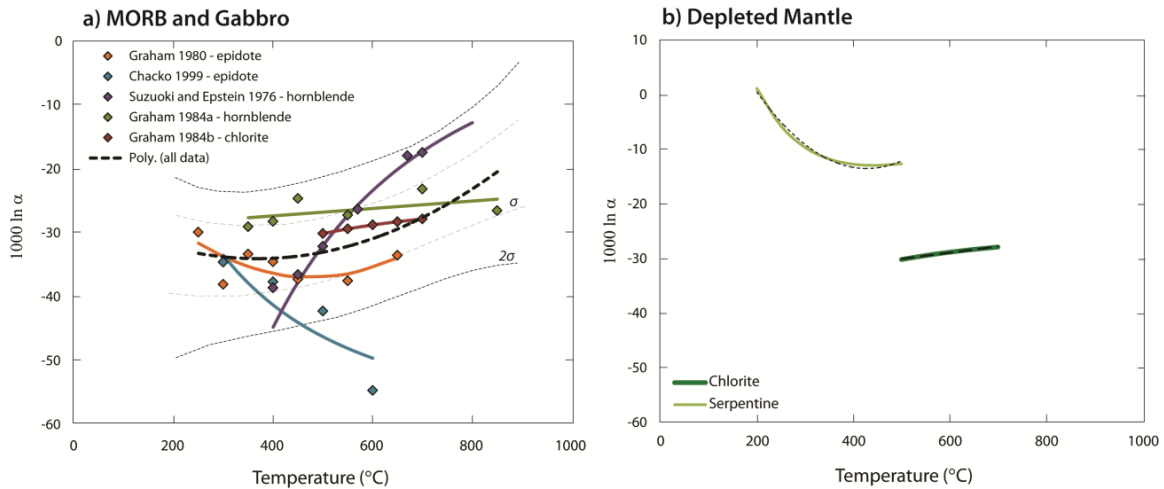
Supplementary Figure A.5. Experimentally derived fractionation factors (1000lnα) versus temperature for minerals found in **a)** MORB and gabbro and **b)** serpentinized mantle. Fractionation factors used are for hornblende (Suzuoki and Epstein, 1976; Graham et al., 1984a), epidote (Graham et al., 1980; Chacko et al., 1999), chlorite (Graham et. al., 1984b), and serpentinite (Sakai and Tatsumi, 1978). In Fig. 5a, large overlaps are seen between experimental results of similar phases, and thus individual experimental data points are plotted along with best fit curves for each set of experiments. The dashed line represents a best fit polynomial regression for all of the data. Because of the range in fractionation factors for similar phases, we use the regression that represents an average rather than calculating modal abundances of minerals present in each lithology. The 2σ curves were used to calculate the total uncertainty in the model contributed by the fractionation factors. For Fig. 5b, serpentinite and chlorite are the only two phases for which fractionation factors exists, and the temperature range over which experiments were performed do not overlap. Therefore, the model uses serpentinite for T<500°C and chlorite for T>500°C.
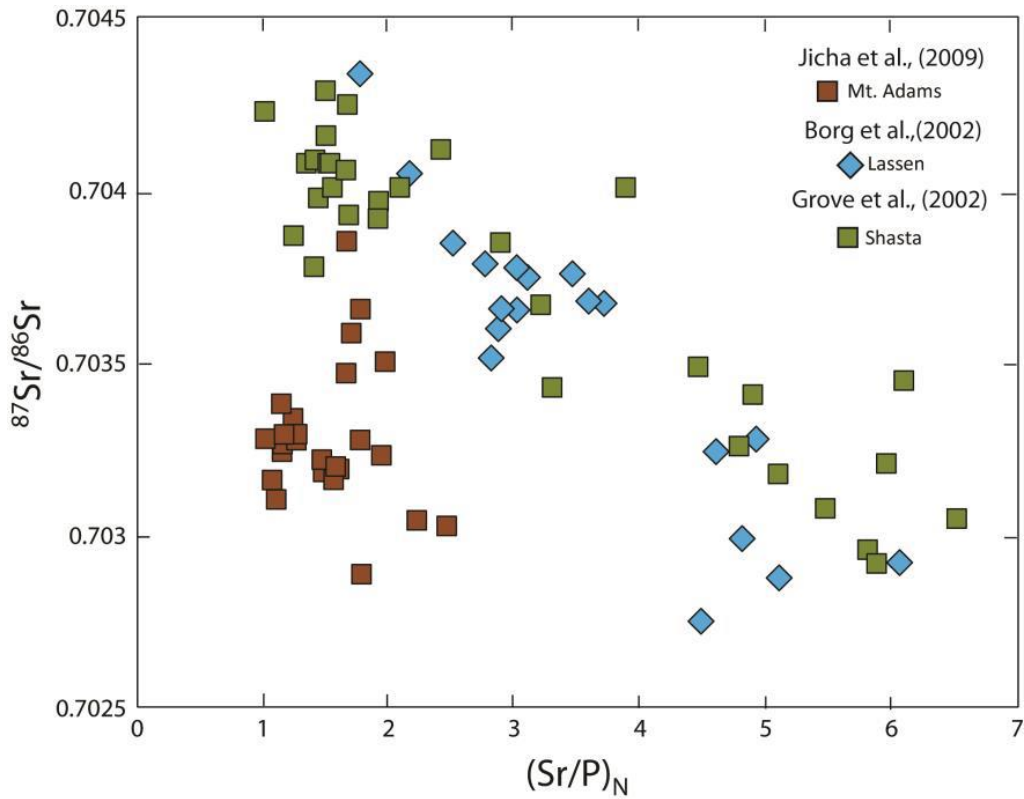
Supplementary Figure A.6. Sr isotopes versus mantle normalized Sr/P for basalts in different Cascade Regions. Variation in $^{87}Sr/^{86}Sr$ in the Mt. Adams region (Jicha et al., 2009) does not show negative correlations seen in the southern Cascades, likely due to a distinct difference in mantle source composition, evidenced by abundant OIB-type magmas in the southern Washington Cascades.
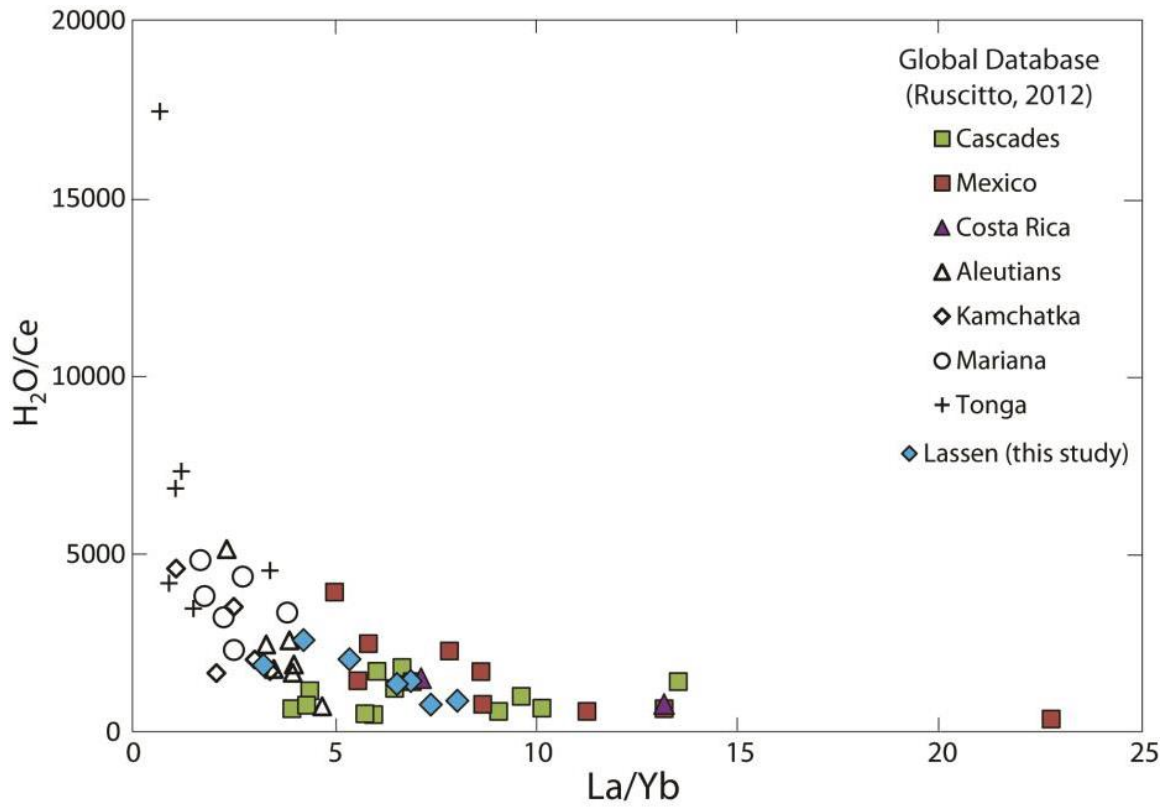
Supplementary Figure A.7. Garnet signature in hot-slab subduction zones H_2O/Ce versus La/Yb from the global database of Ruscitto et al., (2012). Lassen Region data points are averages of each cinder cone analyzed in this study.

A.3. Hydrogen Isotope and Trace Element Compositions

The following table contains analyzed values for individual melt inclusions. H_2O wt% and δD were measured by NanoSIMS, and trace elements weremeasured by LA-ICP-MS, as described in section A.1.

The range in PEC* listed in the table gives the calculated range in post-entrapment crystallization (PEC) from a larger dataset of melt inclusions from the same cinder cones (Chapter III). Major element compositions for the melt inclusions and host olivine were not determined out for these inclusions, and we are therefore unable to correct for post-entrapment modification. However, in the manuscript, we focus on volatile and trace element ratios which should not be affected by PEC.

BORG	S-17	S-13	S-12	S-15	S-09	S-10	S-05	S-06	S-07	S-08	S-01	S-04	S-03
δD (‰)	-11.0	-31.4	-47.9	-29.1	-58.8	-38.7	-42.0	-53.5	-25.1	-26.4	-63.4	-66.8	-48.8
H_2O (wt%)	2.37	2.93	2.51	2.61	2.71	2.54	2.62	2.85	2.44	2.67	3.01	2.92	2.94
Range in													
% PEC*	0.20	- 7.5											
(ppm)													
Li	9.49	6.11	5.19	5.78	4.77	4.61	10.91	10.03	9.65	7.43	5.91	5.64	8.02
B	4.52	3.52	2.95	3.12	4.41	3.13	5.21	5.54	7.28	2.85	1.70	4.78	3.64
P	819	660	710	739	584	605	1291	1096	1009	726	320	1257	685
Ti	5633	4679	4695	4463	4016	4176	4081	6019	6334	4771	1550	7092	4562
V	236	236	318	237	242	262	348	289	288	249	164	307	257
Cu	305	78	110	174	104	103	152	129	369	110	96	138	112
Rb	8.20	5.36	6.03	5.10	4.72	4.95	7.95	7.84	9.78	5.88	1.53	10.25	5.10
Sr	660	533	487	353	410	411	368	602	707	523	541	635	422
Y	15.08	13.03	12.95	13.13	11.68	11.72	12.93	16.00	14.95	13.66	4.60	16.79	12.14
Zr	59.68	53.91	49.88	59.87	46.65	44.87	57.34	65.80	67.88	53.66	14.94	81.60	50.48
Nb	1.78	2.20	2.24	2.33	1.85	1.82	1.59	3.40	2.07	2.15	0.58	3.74	1.93
Ba	230	179	178	125	130	125	138	228	285	177	54	262	135
La	6.65	5.65	4.64	4.46	4.25	4.51	5.09	6.69	7.88	5.39	1.70	8.20	5.07
Ce	15.48	13.05	13.14	11.79	10.73	11.01	13.93	17.01	18.02	13.73	3.94	20.16	13.35
Pr	1.99	1.87	1.77	1.50	1.57	1.56	1.64	2.54	2.41	1.73	0.52	2.96	1.64
Nd	10.23	9.10	9.36	8.80	7.14	7.61	7.84	11.25	12.65	8.54	2.49	12.19	9.29
Sm	2.65	2.51	2.04	1.84	1.75	1.68	1.33	2.67	1.99	2.53	0.44	2.09	2.27
Eu	1.05	0.82	0.79	0.82	0.61	0.73	0.33	0.86	1.12	0.73	0.27	1.17	0.85
Gd	2.53	2.16	1.94	2.34	2.03	2.37	3.77	3.10	3.10	2.76	0.53	2.90	2.71
Dy	2.16	2.15	2.23	2.41	2.26	2.09	2.18	2.91	2.93	2.71	0.51	2.89	2.10
Er	1.43	1.33	1.47	1.38	1.35	1.41	N/A	1.65	1.69	1.73	0.50	1.91	1.32
Yb	1.75	1.63	1.65	1.36	1.22	1.24	N/A	1.67	1.42	1.03	0.47	1.60	1.45
Hf	1.95	1.28	1.35	1.26	1.23	1.09	1.10	1.21	1.78	1.31	0.32	1.58	1.50
Ta	0.07	0.12	0.12	0.11	0.05	0.09	N/A	0.13	N/A	0.05	N/A	0.14	0.07
Pb	4.28	2.90	3.42	1.71	2.38	2.50	2.27	3.46	5.17	2.86	0.82	5.09	3.23
Th	0.93	0.87	0.48	0.68	0.56	0.59	0.80	0.92	1.30	0.69	0.26	1.05	0.60
U	0.37	0.15	0.29	0.21	0.22	0.14	0.38	0.30	0.49	0.08	0.05	0.49	0.26

BBL	BBL-S-06	BBL-S-11	BBL-S-08	BBL-S-05	BBL-S-04	BBL-S-02
δD (‰)	5.17	-63.49	-59.52	-60.22	-79.41	-39.71
H_2O (wt%)	0.905	1.291	1.304	1.194	1.318	1.268
Range in % PEC*	2.2-6.6					
(ppm)						
Li	6.59	5.75	5.04	6.05	10.25	12.15
B	1.38	0.63	1.38	6.23	2.64	N/A
P	874	942	973	3384	857	1237
Ti	5299	6266	6196	13031	5464	7100
V	206	202	219	310	217	259
Cu	151	58	83	75	71	114
Rb	3.67	4.85	5.23	16.51	3.54	7.20
Sr	226	262	256	387	251	266
Y	19.22	21.84	20.74	32.97	19.29	25.20
Zr	60.52	79.48	74.09	194.35	71.64	97.29
Nb	1.77	2.60	2.48	9.24	1.93	3.35
Ba	105	146	146	428	134	189
La	4.05	6.04	5.81	17.44	5.63	7.35
Ce	11.16	14.42	16.08	39.22	15.18	20.04
Pr	1.60	2.05	2.14	5.25	1.94	2.71
Nd	7.90	10.46	8.66	24.34	9.68	11.94
Sm	2.23	3.39	2.89	5.39	2.62	3.25
Eu	0.82	1.04	1.00	1.63	1.02	1.09
Gd	2.13	3.54	2.97	5.72	3.15	3.79
Dy	3.44	3.53	3.33	6.09	3.21	4.08
Er	2.00	2.42	3.00	3.80	2.37	2.41
Yb	2.14	2.50	3.27	3.50	1.77	3.26
Hf	1.51	1.68	1.97	4.90	1.45	2.30
Ta	0.10	0.16	0.09	0.61	0.13	0.20
Pb	1.85	1.85	1.92	6.02	1.86	3.58
Th	0.33	0.44	0.46	1.72	0.20	0.76
U	0.07	0.14	0.16	0.64	0.21	0.21

CC	S-09-1	S-09-5	S-09-6	S-09-7	S-09-9	S-02-6	S-02-10	S-02-3	S-02-1	S-02-8
δD (‰)	-57.67	-37.78	-46.69	-61.28	-22.13	-82.82	-50.95	-71.94	-60.02	-55.45
H₂O (wt%)	2.554	2.680	2.734	2.556	2.654	2.760	2.559	2.627	2.421	2.524
Range in % PEC*	3.1-	12.3								
(ppm)										
Li	8.85	11.27	11.34	11.48	9.33	15.27	12.72	10.35	10.66	11.02
B	9.23	7.76	6.41	4.95	5.61	6.41	6.53	5.68	6.17	7.20
P	1050	1123	1064	1068	1043	1732	1622	1160	1371	1856
Ti	4998	4777	4833	4701	4903	5972	6069	5802	5745	6153
V	214	220	204	239	218	236	224	191	208	260
Cu	75	91	84	82	77	86	97	69	72	95
Rb	18.16	17.35	18.56	16.91	16.23	23.04	19.94	16.86	16.87	19.40
Sr	376	344	383	355	357	419	431	424	412	405
Y	11.92	15.21	13.50	13.36	13.60	16.51	15.35	14.43	16.16	15.86
Zr	78.80	76.91	75.64	69.07	74.46	96.86	94.69	95.01	98.97	91.08
Nb	4.24	4.01	4.43	4.01	4.12	6.46	6.99	6.05	6.44	6.40
Ba	234	204	242	203	219	271	265	268	269	248
La	7.59	7.59	7.67	7.23	7.57	10.30	10.07	10.47	10.42	9.94
Ce	18.26	18.04	18.74	18.43	17.72	26.03	22.62	22.94	23.80	27.27
Pr	2.49	2.35	2.30	2.20	2.27	2.88	3.05	2.85	3.14	3.09
Nd	11.01	10.44	10.46	9.94	9.60	13.45	12.91	13.46	13.84	11.42
Sm	2.48	2.84	2.17	1.99	2.46	2.55	2.99	3.06	2.86	2.18
Eu	0.84	0.66	0.77	0.72	1.02	0.72	0.95	1.05	1.01	0.98
Gd	3.00	2.62	2.42	2.49	1.76	2.79	2.73	3.56	1.93	2.64
Dy	2.60	2.44	2.62	2.67	2.44	2.47	2.73	3.18	2.90	2.75
Er	1.56	1.78	1.26	1.95	1.40	2.12	1.83	2.09	1.82	1.89
Yb	1.40	1.34	1.58	1.55	1.68	2.11	1.40	2.57	1.50	1.72
Hf	1.91	1.86	2.09	1.61	1.93	2.24	1.99	2.12	2.41	2.05
Ta	0.12	0.25	0.17	0.19	0.22	0.28	0.41	0.39	0.46	0.30
Pb	3.65	3.54	3.72	2.87	3.15	3.80	3.92	3.36	3.89	6.31
Th	1.86	1.56	1.90	1.36	1.29	1.76	1.89	1.80	2.06	1.51
U	0.49	0.47	0.59	0.37	0.47	0.56	0.57	0.46	0.61	0.83

BRVB	BRVB-S-14	BRVB-S-11	BRVB-S-9	BRVB-S-8	BRVB-S-13	BRVB-S-6	BRVB-S-1
δD (‰)	-42.09	46.15	8.06	-23.27	4.63	162.27	82.13
H_2O (wt%)	2.187	1.632	1.922	2.236	1.918	0.542	1.372
Range in % PEC*	3.1-10.2						
(ppm)							
Li	6.90	10.48	13.58	9.72	7.14	7.00	8.41
B	4.49	5.46	7.06	4.02	3.61	4.47	4.97
P	1891	1946	2269	1436	1566	1541	1623
Ti	7375	7300	7474	7241	7592	7072	7378
V	216	251	246	208	209	210	203
Cu	65	78	75	60	66	42	61
Rb	18.05	19.01	21.63	14.82	16.26	15.24	16.75
Sr	427	417	391	432	427	398	420
Y	17.15	18.04	19.67	18.14	17.18	19.37	18.24
Zr	96.59	96.99	109.14	110.82	105.87	94.69	104.66
Nb	6.61	6.78	7.04	5.98	6.45	6.08	6.30
Ba	337	335	327	361	350	311	333
La	12.91	12.22	13.79	13.46	13.79	12.79	13.08
Ce	29.56	29.42	32.24	32.64	32.20	27.83	29.09
Pr	3.51	3.71	3.77	3.96	3.91	3.88	4.08
Nd	17.23	16.13	18.26	20.70	17.47	16.12	16.80
Sm	4.05	4.04	3.55	4.47	3.63	4.08	3.80
Eu	1.26	1.19	1.14	1.43	0.92	1.19	1.16
Gd	3.66	3.50	4.30	3.68	4.05	3.43	3.56
Dy	3.34	3.24	3.68	4.20	3.61	3.76	3.52
Er	2.21	1.72	2.05	2.27	1.78	2.13	1.90
Yb	1.60	1.86	1.92	2.20	1.54	2.03	1.56
Hf	2.40	2.22	2.26	3.04	2.18	2.30	2.19
Ta	0.40	0.33	0.27	0.32	0.33	0.31	0.33
Pb	3.89	3.76	4.54	4.06	4.14	3.05	3.24
Th	1.31	1.55	1.71	2.07	1.66	1.34	1.62
U	0.49	0.56	0.40	0.40	0.53	0.41	0.51

BPPC	BPPC-S-01	BPPC-S-07	BPPC-S-11	BPPC-S-05	BPPC-S-04
δD (‰)	-47.21	-35.26	-45.98	-56.15	-46.61
H_2O (wt%)	2.127	2.161	2.154	2.194	2.206
Range in % PEC*	0.3-12				
(ppm)					
Li	6.28	7.97	9.33	5.27	7.81
B	1.79	2.80	4.77	2.40	3.82
P	762	738	746	694	744
Ti	4602	4993	4929	4775	5100
V	246	279	231	232	249
Cu	296	14	28	38	32
Rb	4.49	7.14	6.00	5.89	6.94
Sr	451	470	469	448	455
Y	13.86	16.00	16.60	15.42	15.22
Zr	51.76	61.96	64.83	57.14	60.58
Nb	1.06	1.59	1.74	1.45	2.02
Ba	97	128	125	117	131
La	4.72	5.58	5.86	5.42	5.58
Ce	13.03	14.96	15.25	13.72	15.47
Pr	1.82	1.80	2.12	2.02	1.95
Nd	8.72	10.91	9.55	8.14	9.15
Sm	1.55	2.20	2.50	2.85	2.14
Eu	0.84	0.90	1.08	0.88	0.84
Gd	2.40	2.20	3.16	3.26	2.88
Dy	3.01	3.19	3.69	2.18	2.43
Er	1.74	2.30	2.37	1.95	1.44
Yb	1.40	1.32	1.72	1.66	1.69
Hf	1.50	1.10	1.42	1.56	1.35
Ta	N/A	N/A	0.07	0.10	0.14
Pb	3.22	3.40	2.04	2.07	2.65
Th	0.37	0.68	0.64	0.52	0.58
U	0.17	0.19	0.13	0.16	0.16

	BAS-44-S-03	BAS-44-S-01	BAS-44-S-06	BPB-S-02	BPB-S-04	BPB-S-07	BPB-S-08
δD (‰)	-52.65	-52.37	-29.73	-25.14	-29.12	-37.31	-34.92
H_2O (wt%)	1.135	1.169	0.863	2.299	2.485	2.576	2.506
Range in % PEC*	1.8-4.3	(BAS-44)				0.1-12	(BPB)
(ppm)							
Li	5.13	6.33	3.25	8.67	10.05	9.97	11.06
B	3.01	6.24	2.52	6.42	9.13	4.57	16.96
P	1127	949	1091	2017	1536	1356	1897
Ti	6353	6104	6185	6720	5218	5218	5328
V	229	223	232	255	230	212	256
Cu	50	127	133	97	84	77	100
Rb	5.03	3.76	6.20	16.46	16.38	12.96	25.72
Sr	440	389	416	420	450	450	465
Y	19.18	19.14	19.78	16.14	13.39	14.15	14.47
Zr	78.63	78.49	77.06	96.31	90.32	80.91	83.56
Nb	3.21	3.38	3.16	7.93	5.12	5.28	5.30
Ba	124	126	145	362	314	316	316
La	7.18	7.36	7.66	12.83	11.42	10.84	10.42
Ce	21.35	23.03	21.03	28.91	26.99	25.48	25.74
Pr	2.87	3.13	2.95	3.71	3.23	3.29	3.44
Nd	13.50	13.26	12.72	15.62	14.31	12.72	13.45
Sm	3.36	2.75	3.12	2.98	3.20	2.47	3.68
Eu	1.26	1.00	0.89	1.11	0.93	0.78	0.89
Gd	2.86	3.68	2.57	3.06	2.77	2.70	2.38
Dy	3.71	3.11	3.84	3.00	2.31	3.64	2.30
Er	2.59	2.47	2.42	1.44	1.49	1.86	1.49
Yb	1.64	1.09	2.09	0.84	1.76	1.41	1.37
Hf	1.57	1.78	1.69	2.95	2.30	2.29	1.91
Ta	N/A	N/A	0.25	0.25	0.33	0.26	0.30
Pb	1.92	1.59	2.93	4.31	5.25	3.70	6.15
Th	0.55	0.40	0.83	1.37	1.52	1.43	1.70
U	0.16	0.23	0.28	0.53	0.81	0.45	0.85

	Average Error
NanoSIMS	
δD (‰)	±12‰ (2σ)
H₂O (wt%)	0.12 wt% (2σ)
LA-ICP-MS	
(ppm)	1 S.E.
Li	0.94
B	0.89
P	73
Ti	139
V	7.22
Cu	6.46
Rb	0.63
Sr	8.67
Y	0.53
Zr	2.41
Nb	0.26
Ba	4.9
La	0.35
Ce	0.63
Pr	0.15
Nd	0.64
Sm	0.32
Eu	0.11
Gd	0.38
Dy	0.28
Er	0.24
Yb	0.27
Hf	0.27
Ta	0.09
Pb	0.39
Th	0.15
U	0.16

Supplementary References

Agrinier, P., Hékinian, R., Bideau, D., & Javoy, M. (1995). O and H stable isotope compositions of oceanic crust and upper mantle rocks exposed in the Hess Deep near the Galapagos Triple Junction. *Earth and Planetary Science Letters*, 136(3), 183-196.

Alt, J. C., & Shanks III, W. C. (2006). Stable isotope compositions of serpentinite seamounts in the Mariana forearc: Serpentinization processes, fluid sources and sulfur metasomatism. *Earth and Planetary Science Letters*, 242(3), 272-285.

Bach, W., Peucker-Ehrenbrink, B., Hart, S. R., & Blusztajn, J. S. (2003). Geochemistry of hydrothermally altered oceanic crust: DSDP/ODP Hole 504B–Implications for seawater-crust exchange budgets and Sr-and Pb-isotopic evolution of the mantle. *Geochemistry, Geophysics, Geosystems*, *4*(3).

Bacon C.R., Bruggman P.E., Christiansen, R.L, Clynne, M.A., Donnelly-Nolan, J.M., Hildreth, W. (1997). Primitive magmas at five Cascade volcanic fields: melts from hot, heterogeneous sub-arc mantle. *Canadian Mineralogist*, *35*. 397–42.

Barnes, J. D., Paulick, H., Sharp, Z. D., Bach, W., & Beaudoin, G. (2009). Stable isotope (δ^{18}O, δD, δ^{37}Cl) evidence for multiple fluid histories in mid-Atlantic abyssal peridotites (ODP Leg 209). *Lithos*, 110(1), 83-94.

Barnes, J. D., Sharp, Z. D., Fischer, T. P., Hilton, D. R., & Carr, M. J. (2009). Chlorine isotope variations along the Central American volcanic front and back arc. *Geochemistry, Geophysics, Geosystems*, *10*(11).

Borg, L. E., Brandon, A. D., Clynne, M. A., & Walker, R. J. (2000). Re–Os isotopic systematics of primitive lavas from the Lassen region of the Cascade arc, California. *Earth and Planetary Science Letters*, *177*(3), 301-317.

Cagnioncle, A. M., Parmentier, E. M., & Elkins-Tanton, L. T. (2007). Effect of solid flow above a subducting slab on water distribution and melting at convergent plate boundaries. *Journal of Geophysical Research: Solid Earth (1978–2012)*, *112*(B9).

Chacko, T., Riciputi, R., Cole, R., & Horita, J. (1999). A new technique for determining equilibrium hydrogen isotope fractionation factors using the ion microprobe: Application to the epidote-water system. *Geochimica et cosmochimica acta*, *63*(1), 1-10.

Clynne, M. A. (1993). *Geologic studies of the Lassen volcanic center, Cascade Range, California*. University of California, Santa Cruz.

Clynne, M.A., Muffler, L. J. P., Siems, D. F., Taggart Jr, J. E., & Bruggman, P. (2008). *Major and EDXRF trace element chemical analyses of volcanic rocks from Lassen Volcanic National Park and vicinity, California*. US Geological Survey.

Clynne, M. A., & Muffler, L. J. P. (2010). *Geologic map of Lassen Volcanic National Park and vicinity, California*. US Department of the Interior, US Geological Survey.

DePaolo, D. J., & Wasserburg, G. J. (1977). The sources of island arcs as indicated by Nd and Sr isotopic studies. *Geophysical Research Letters*, *4*(10), 465-468.

Donnelly, K. E., Goldstein, S. L., Langmuir, C. H., & Spiegelman, M. Origin of enriched ocean ridge basalts and implications for mantle dynamics. *Earth and Planetary Science Letters*, 226(3), 347-366 (2004).

Gaetani, G. A., O'Leary, J. A., Shimizu, N., Bucholz, C. E., & Newville, M. (2012). Rapid reequilibration of H_2O and oxygen fugacity in olivine-hosted melt inclusions. *Geology, 40(10),* 915–918.

Graham, C. M., Sheppard, S. M., & Heaton, T. H. (1980). Experimental hydrogen isotope studies—I. Systematics of hydrogen isotope fractionation in the systems epidote-H_2O, zoisite-H_2O and AlO (OH)-H_2O. *Geochimica et Cosmochimica Acta*, *44*(2), 353-364.

Graham, C. M., Harmon, R. S., Sheppard, M. F. (1984). Experimental hydrogen isotope studies: hydrogen isotope exchange between amphibole and water. *American Mineralogist*, *69*, 128-138.

Hacker, B. R. (2008). H_2O subduction beyond arcs. *Geochemistry Geophysics Geosystems, 9*(3).

Iwamori, H. (1998). Transportation of H_2O and melting in subduction zones. *Earth and Planetary Science Letters*, *160*(1), 65-80.

Iwamori, H. (2007). Transportation of H_2O beneath the Japan arcs and its implications for global water circulation. *Chemical Geology*, *239*(3), 182-198.

Jicha, B. R., Hart, G. L., Johnson, C. M., Hildreth, W., Beard, B. L., Shirey, S. B., & Valley, J. W. (2008). Isotopic and trace element constraints on the petrogenesis of lavas from the Mount Adams volcanic field, Washington. *Contributions to Mineralogy and Petrology, 157(2),* 189–207.

John, T., Klemd, R., Gao, J., & Garbe-Schönberg, C. D. (2008). Trace-element mobilization in slabs due to non-steady-state fluid–rock interaction: constraints from an eclogite-facies transport vein in blueschist (Tianshan, China). *Lithos*, *103*(1), 1-24.

John, T., Gussone, N., Podladchikov, Y. Y., Bebout, G. E., Dohmen, R., Halama, R., and Seitz, H. M. (2012). Volcanic arcs fed by rapid pulsed fluid flow through subducting slabs. *Nature Geoscience*, *5*(7), 489-492.

Kessel, R., Schmidt, M. W., Ulmer, P., & Pettke, T. (2005). Trace element signature of subduction-zone fluids, melts and supercritical liquids at 120–180 km depth. *Nature*, 437(7059), 724-727.

Klimm, K., Blundy, J. D., & Green, T. H. (2008). Trace element partitioning and accessory phase saturation during H2O-saturated melting of basalt with implications for subduction zone chemical fluxes. *Journal of Petrology*, 49(3), 523-553.

Michael, P. (1995). Regionally distinctive sources of depleted MORB: Evidence from trace elements and H_2O. *Earth and Planetary Science Letters, 131(3),* 301-320.

Newman, S., Epstein, S., & Stolper, E. (1988). Water, carbon dioxide, and hydrogen isotopes in glasses from the ca. 1340 AD eruption of the Mono Craters, California: constraints on degassing phenomena and initial volatile content. *Journal of Volcanology and Geothermal Research*, *35*(1), 75-96.

Plank, T., Cooper, L. B., & Manning, C. E. (2009). Emerging geothermometers for estimating slab surface temperatures. *Nature Geoscience*, 2(9), 611-615.

Portnyagin, M., Hoernle, K., Plechov, P., Mironov, N., & Khubunaya, S. (2007). Constraints on mantle melting and composition and nature of slab components in volcanic arcs from volatiles (H_2O, S, Cl, F) and trace elements in melt inclusions from the Kamchatka Arc. *Earth and Planetary Science Letters*, 255(1-2), 53–69.

Ranero, C. R., Morgan, J. P., McIntosh, K., & Reichert, C. (2003). Bending-related faulting and mantle serpentinization at the Middle America trench. *Nature*, 425(6956), 367-373.

Ruscitto, D. M., Wallace, P. J., Cooper, L. B., & Plank, T. (2012). Global variations in H_2O/Ce: 2. Relationships to arc magma geochemistry and volatile fluxes. *Geochemistry Geophysics Geosystems*, 13(3).

Sakai, H. & Tsutsumi, M. (1978). D/H fractionation factors between serpentine and water at 100 to 500 C and 2000 bar water pressure, and the D/H ratios of natural serpentines. *Earth Planetary Science Letters*, 40: 231-242.

Suzuoki, T., & Epstein, S. (1976). Hydrogen isotope fractionation between OH-bearing minerals and water. *Geochimica et Cosmochimica Acta*, 40(10), 1229-1240.

White, W. M. (2005). Stable isotope geochemistry. Geochemistry: An Online Text Book.

Wilson, C. R., Spiegelman, M., van Keken, P. E., & Hacker, B. R. (2014). Fluid flow in subduction zones: The role of solid rheology and compaction pressure. *Earth and Planetary Science Letters*, 401, 261-274.

Workman, R. K., & Hart, S. R. Major and trace element composition of the depleted MORB mantle (DMM). *Earth and Planetary Science Letters*, 231(1), 53-72 (2005).

APPENDIX B

CHAPTER III SUPPLEMENTARY MATERIALS

B.1. Restored Melt Inclusion Compositions

Data in this table represents individual melt inclusion compositions that have been corrected for Fe loss and post-entrapment crystallization (PEC). Major elements were restored using Petrolog 3.1.1 (Danyushevsky and Plechov, 2011). Volatile and trace elements were restored by the same percent as K_2O because all are incompatible in the olivine host. Major element standard deviations represent an average of those calculated for each melt inclusion from a given sample based on three EPMA point analyses. Trace element standard deviations are also an average from individual inclusions from a given sample based on the methods of Loewen and Kent (2012).

SAMPLE INC #	BBL 1	BBL 3	BBL 4	BBL 6	BBL 8	BBL 9	BBL 13	BBL 15	BBL 18	BBL 20	BBL 21	avg s.d.
wt%												
SiO_2	49.89	49.09	48.35	49.33	50.74	48.85	48.30	49.88	49.09	49.79	49.09	0.11
TiO_2	1.22	0.96	0.82	1.09	1.27	0.99	0.88	1.26	1.05	1.07	1.01	0.03
Al_2O_3	16.85	17.29	16.64	16.90	15.77	17.53	17.42	16.66	17.22	16.43	16.97	0.15
FeO^T	9.42	9.42	9.42	9.42	9.42	9.42	9.42	9.42	9.42	9.42	9.42	0.11
MnO	0.16	0.15	0.09	0.15	0.17	0.13	0.12	0.15	0.14	0.14	0.13	0.01
MgO	7.20	8.15	10.05	7.74	6.84	7.86	9.06	7.27	7.60	8.05	8.48	0.06
CaO	10.30	10.61	10.86	10.35	9.54	10.40	10.14	9.05	10.06	10.01	9.89	0.03
Na_2O	3.17	2.96	2.54	3.11	3.51	3.18	2.90	3.50	3.20	3.19	3.09	0.02
K2O	0.46	0.30	0.15	0.39	0.71	0.37	0.28	0.72	0.41	0.39	0.37	0.01
P_2O_5	0.21	0.15	0.10	0.18	0.27	0.17	0.15	0.29	0.19	0.18	0.16	0.01
S	0.11	0.11	0.08	0.11	0.12	0.11	0.10	0.12	0.12	0.11	0.11	0.003
Cl	0.024	0.014	0.010	0.017	0.024	0.023	0.011	0.025	0.017	0.022	0.015	0.004
CO_2 (ppm)	897	784	437	848	929	866	549	1034	852	712	856	69
H_2O	0.94	0.77	0.80	1.17	1.47	0.94	1.18	1.57	1.47	1.15	1.23	0.06
% PEC	1.20	4.54	14.39	2.38	0.60	2.40	7.81	1.80	1.31	3.87	6.36	
Fo	83.7	85.3	87.8	84.7	83.0	85.0	86.7	84.0	84.5	85.2	85.9	
ppm												
Li	N/A	N/A	8.92	7.78	9.18	7.41	7.78	9.38	5.96	8.05	6.07	1.50
B	N/A	N/A	3.27	1.87	5.16	0.47	2.63	3.59	1.82	2.42	1.38	1.13
Sc	N/A	N/A	45.14	40.10	40.70	36.03	33.19	42.02	41.90	38.61	37.65	3.33
V	N/A	N/A	248	236	266	221	209	219	226	234	226	13
Rb	N/A	N/A	2.06	5.67	9.74	5.21	4.06	8.16	6.11	6.52	5.40	0.31
Sr	N/A	N/A	193	275	308	270	249	307	285	269	275	5
Y	N/A	N/A	19.41	21.35	24.52	20.05	19.09	24.86	23.85	21.60	21.25	1.73
Zr	N/A	N/A	56.34	78.59	118.55	73.80	70.39	106.75	92.64	79.53	81.12	6.63
Nb	N/A	N/A	1.08	2.97	5.41	2.92	2.70	4.96	3.41	3.23	2.73	0.35
Ba	N/A	N/A	70.06	170.44	297.04	147.14	122.48	247.66	174.24	168.02	154.92	4.36
La	N/A	N/A	2.94	6.44	10.98	5.81	4.92	10.44	7.55	6.62	6.10	0.19
Ce	N/A	N/A	8.81	16.81	29.05	14.96	13.12	25.37	17.57	16.95	15.93	0.43
Pr	N/A	N/A	1.26	2.37	3.85	2.04	1.88	3.40	2.54	2.33	2.04	0.10
Nd	N/A	N/A	6.77	11.83	17.27	10.93	9.02	15.23	11.62	11.07	10.35	0.32
Sm	N/A	N/A	2.37	2.93	4.24	2.51	2.53	3.59	2.72	3.02	2.94	0.14
Eu	N/A	N/A	0.83	1.09	1.43	0.98	0.98	1.22	1.03	1.17	1.00	0.08
Gd	N/A	N/A	3.45	3.59	3.87	3.29	2.92	4.47	4.36	3.62	3.24	0.19
Dy	N/A	N/A	3.29	3.74	4.66	3.91	3.53	4.08	4.14	3.83	3.68	0.15
Er	N/A	N/A	2.41	2.47	2.73	2.38	2.17	3.18	2.85	2.74	2.47	0.14
Yb	N/A	N/A	2.45	2.44	2.84	2.24	2.42	3.07	2.47	2.60	2.67	0.15
Hf	N/A	N/A	1.36	1.95	2.58	1.55	1.50	2.57	1.96	2.09	1.61	0.11
Ta	N/A	N/A	0.06	0.17	0.36	0.13	0.15	0.29	0.19	0.18	0.19	0.03
Pb	N/A	N/A	0.89	2.15	3.65	1.70	1.46	3.13	2.08	2.01	1.70	0.11
Th	N/A	N/A	0.18	0.59	0.99	0.57	0.33	0.89	0.55	0.56	0.49	0.05
U	N/A	N/A	0.08	0.23	0.39	0.15	0.13	0.34	0.18	0.20	0.17	0.02

INC #	BPB 1	BPB 3a	BPB 3b	BPB 4	BPB 5	BPB 9	BPB 10a	BPB 10b	BPB 14a	BPB 14b	BPB 17	BPB 18	BPB 19	BPB 20	BPB 21	BPB 22	avg s.d.
wt%																	
SiO_2	50.77	51.21	51.27	50.14	50.44	51.45	50.98	50.39	51.42	52.17	51.42	50.83	49.88	51.26	51.07	51.16	0.24
TiO_2	0.90	0.90	0.91	0.86	0.88	0.90	0.87	0.88	0.87	0.85	0.92	0.89	0.85	0.93	0.96	0.87	0.01
Al_2O_3	17.19	17.07	17.20	16.67	17.73	17.01	15.86	16.68	16.18	15.88	17.16	16.65	17.64	16.98	18.27	16.63	0.07
FeO^T	7.65	7.65	7.65	7.65	7.65	7.65	7.65	7.65	7.65	7.65	7.65	7.65	7.65	7.65	7.65	7.65	0.07
MnO	0.12	0.12	0.12	0.11	0.11	0.12	0.09	0.11	0.10	0.13	0.15	0.12	0.11	0.16	0.11	0.09	0.01
MgO	7.07	6.85	6.84	7.88	7.46	6.84	7.91	7.90	7.77	7.73	7.73	7.83	7.69	7.38	6.14	7.29	0.18
CaO	10.37	10.05	10.13	9.67	9.89	10.21	10.02	10.38	9.96	9.77	10.40	10.00	10.13	10.25	10.08	10.12	0.10
Na_2O	2.61	2.83	2.80	2.91	2.91	2.87	2.93	2.82	2.73	2.88	2.71	2.60	2.55	3.22	2.86	3.08	0.06
K2O	0.77	0.82	0.84	0.81	0.76	0.82	0.75	0.75	0.76	0.82	1.01	0.80	0.78	1.02	0.87	0.78	0.02
P_2O	0.25	0.24	0.23	0.24	0.24	0.27	0.24	0.24	0.24	0.23	0.25	0.24	0.25	0.25	0.26	0.25	0.01
S	0.11	0.09	0.09	0.11	0.11	0.09	0.12	0.11	0.11	0.09	0.06	0.12	0.11	0.09	0.09	0.11	0.003
Cl	0.060	0.061	0.061	0.058	0.050	0.059	0.063	0.057	0.058	0.059	0.059	0.058	0.059	0.069	0.061	0.058	0.001
CO_2 (ppm)	629	370	285	847	581	310	1563	1061	1123	475	135	412	1385	106	231	660	83
H_2O %	2.42	2.37	2.12	3.18	2.04	1.99	2.81	2.34	2.45	2.00	0.72	2.51	2.58	0.96	1.85	2.20	0.16
PEC	2.66	0.55	0.00	2.93	2.24	3.67	10.70	6.78	4.79	3.23	3.61	3.93	4.18	2.69	0.19	4.09	
Fo	86.1	85.8	85.8	87.7	87.0	85.8	87.7	87.7	87.3	87.3	87.4	87.4	87.2	87.1	84.4	86.8	
ppm																	
Li	8.63	8.49	N/A	7.21	4.54	8.17	15.49	14.52	8.12	10.36	10.73	N/A	N/A	12.39	N/A	8.82	1.97
B	4.97	10.13	N/A	17.00	3.09	8.71	5.50	5.34	4.70	7.52	9.85	N/A	N/A	6.63	N/A	11.88	1.68
Sc	34.01	35.74	N/A	35.39	34.32	36.58	53.90	41.41	38.30	28.17	38.40	N/A	N/A	38.90	N/A	36.59	1.51
V	244	207	N/A	217	171	212	318	254	227	217	227	N/A	N/A	263	N/A	226	11
Rb	15.22	16.97	N/A	17.14	11.37	14.87	18.36	14.47	14.90	15.57	18.53	N/A	N/A	21.09	N/A	13.95	0.95
Sr	531	446	N/A	499	481	481	510	523	498	466	476	N/A	N/A	452	N/A	551	7
Y	19.08	16.31	N/A	17.45	16.55	15.69	17.24	16.13	15.41	13.99	17.71	N/A	N/A	18.47	N/A	15.60	0.76
Zr	108	90	N/A	102	96	92	107	96	97	101	106	N/A	N/A	106	N/A	95	4
Nb	6.48	5.54	N/A	5.97	5.37	5.66	5.80	5.22	5.47	5.44	6.11	N/A	N/A	6.88	N/A	6.28	0.36
Ba	328	304	N/A	336	258	308	359	338	304	311	374	N/A	N/A	401	N/A	319	5
La	13.71	10.27	N/A	12.72	11.59	11.54	11.77	11.52	10.52	11.99	12.75	N/A	N/A	13.38	N/A	12.23	0.21
Ce	28.33	22.96	N/A	23.35	20.34	25.62	35.87	29.11	25.95	25.69	28.74	N/A	N/A	30.62	N/A	29.65	0.55
Pr	4.06	3.36	N/A	3.77	3.14	2.96	4.05	3.01	3.40	3.22	3.40	N/A	N/A	4.02	N/A	3.54	0.15
Nd	14.55	15.10	N/A	15.95	11.24	13.80	15.26	18.17	13.45	13.35	17.43	N/A	N/A	18.56	N/A	16.10	0.57
Sm	3.59	3.89	N/A	3.38	3.04	3.47	2.42	2.37	2.45	3.94	3.81	N/A	N/A	3.60	N/A	3.07	0.33
Eu	1.20	1.03	N/A	1.15	1.14	1.02	1.09	1.02	1.01	0.95	1.10	N/A	N/A	1.19	N/A	1.14	0.09
Gd	3.80	3.60	N/A	3.30	2.91	2.80	2.68	3.90	3.22	3.41	3.02	N/A	N/A	4.82	N/A	3.29	0.18
Dy	3.18	3.20	N/A	3.09	2.30	2.92	3.38	3.30	3.12	2.52	2.85	N/A	N/A	3.70	N/A	3.26	0.19
Er	1.69	1.61	N/A	1.73	1.91	2.43	1.68	1.46	1.84	3.26	1.91	N/A	N/A	1.86	N/A	1.99	0.07
Yb	2.02	2.06	N/A	1.64	1.50	2.41	1.89	1.69	1.18	1.63	1.75	N/A	N/A	1.77	N/A	1.85	0.14
Hf	2.69	2.45	N/A	2.24	3.38	2.64	2.36	2.36	1.16	2.41	3.09	N/A	N/A	2.79	N/A	1.70	0.15
Ta	0.33	0.40	N/A	0.37	0.33	0.33	0.32	0.28	0.47	0.27	0.32	N/A	N/A	0.39	N/A	0.24	0.03
Pb	4.29	4.73	N/A	4.46	2.92	4.65	4.76	4.43	4.51	3.33	5.30	N/A	N/A	5.97	N/A	3.81	0.21
Th	2.78	1.93	N/A	1.57	1.53	2.08	1.59	1.60	1.34	1.91	1.99	N/A	N/A	2.03	N/A	1.60	0.13
U	0.61	0.55	N/A	0.40	0.39	0.52	0.53	0.54	0.52	0.64	0.63	N/A	N/A	0.70	N/A	0.64	0.06

INC #	BRM 1	BRM 2	BRM 3	BRM 5	BRM 6	BRM 7	BRM 8	BRM 9	BRM 10	BRM 11	BRM 14a	BRM 14b	BRM 15	BRM 16	BRM 18	avg s.d.
wt%																
SiO_2	49.33	50.01	50.93	49.72	52.70	49.58	48.74	49.63	48.55	50.89	50.28	50.39	49.99	49.72	50.22	0.29
TiO_2	0.85	0.88	0.80	0.86	0.89	0.87	0.93	0.80	0.82	0.82	0.91	0.91	0.92	0.94	0.87	0.01
Al_2O_3	18.74	20.14	18.15	17.32	15.05	17.86	17.64	17.58	17.87	18.93	19.82	19.87	18.19	17.75	19.11	0.22
FeO^T	8.14	8.14	8.14	8.14	8.14	8.14	8.14	8.14	8.14	8.14	8.14	8.14	8.14	8.14	8.14	0.06
MnO	0.09	0.11	0.12	0.09	0.09	0.10	0.09	0.09	0.08	0.12	0.12	0.12	0.08	0.06	0.11	0.01
MgO	7.31	5.61	5.90	7.59	7.68	7.73	7.26	7.72	7.87	5.70	5.59	5.58	7.40	8.46	5.72	0.28
CaO	9.73	8.92	8.38	9.43	7.65	9.95	9.64	9.74	9.68	8.82	8.61	8.63	9.73	9.71	8.23	0.14
Na_2O	4.12	4.26	3.89	3.55	3.45	3.46	3.87	3.85	3.75	3.89	4.06	4.07	3.86	3.43	3.90	0.15
K_2O	0.70	0.83	0.79	0.75	0.91	0.72	0.78	0.64	0.71	0.80	0.75	0.75	0.73	0.86	0.75	0.02
P_2O_5	0.31	0.31	0.28	0.32	0.32	0.30	0.34	0.27	0.28	0.27	0.25	0.25	0.28	0.31	0.24	0.02
S	0.20	0.17	0.17	0.20	0.08	0.21	0.21	0.22	0.23	0.16	0.16	0.16	0.20	0.21	0.16	0.001
Cl	0.24	0.22	0.21	0.20	0.18	0.23	0.21	0.25	0.25	0.21	0.23	0.23	0.25	0.24	0.23	0.001
CO_2 (ppm)	0	0	166	193	378	321	599	251	306	141	0	0	0	0	270	20
H_2O	0.49	0.57	2.36	2.03	2.97	1.14	2.43	1.39	2.11	1.43	1.35	1.14	0.53	0.45	2.57	0.08
% PEC	8.13	2.19	1.20	10.26	8.42	7.48	7.21	8.10	8.15	2.11	3.79	3.72	9.26	12.75	1.23	
Fo	86.5	82.8	83.0	86.5	86.4	86.8	86.4	87.0	87.3	82.6	82.6	82.6	86.5	87.9	82.8	
ppm																
Li	5.33	N/A	11.50	6.27	11.71	N/A	N/A	N/A	N/A	4.51	N/A	N/A	4.86	N/A	6.68	1.22
B	3.02	N/A	2.74	4.65	2.74	N/A	N/A	N/A	N/A	2.18	N/A	N/A	3.71	N/A	3.22	2.30
Sc	25.93	N/A	22.28	26.34	24.27	N/A	N/A	N/A	N/A	20.18	N/A	N/A	22.34	N/A	19.55	2.11
V	223	N/A	181	202	205	N/A	N/A	N/A	N/A	168	N/A	N/A	219	N/A	154	8
Rb	7.30	N/A	11.75	9.97	13.74	N/A	N/A	N/A	N/A	10.24	N/A	N/A	8.81	N/A	11.19	0.46
Sr	1378	N/A	1173	1257	969	N/A	N/A	N/A	N/A	1039	N/A	N/A	1395	N/A	1167	7
Y	11.08	N/A	11.44	11.39	12.27	N/A	N/A	N/A	N/A	9.42	N/A	N/A	11.72	N/A	12.25	0.83
Zr	85.70	N/A	92.69	92.57	98.34	N/A	N/A	N/A	N/A	79.07	N/A	N/A	95.32	N/A	84.94	5.05
Nb	3.96	N/A	4.58	5.14	6.73	N/A	N/A	N/A	N/A	6.63	N/A	N/A	5.26	N/A	4.25	0.49
Ba	236	N/A	283	285	332	N/A	N/A	N/A	N/A	263	N/A	N/A	284	N/A	257	8
La	14.62	N/A	14.98	15.78	16.43	N/A	N/A	N/A	N/A	13.53	N/A	N/A	16.02	N/A	13.95	0.25
Ce	35.41	N/A	36.69	37.51	37.32	N/A	N/A	N/A	N/A	32.29	N/A	N/A	37.74	N/A	31.52	0.51
Pr	4.20	N/A	4.27	4.41	4.71	N/A	N/A	N/A	N/A	4.09	N/A	N/A	4.65	N/A	4.19	0.08
Nd	17.50	N/A	19.52	19.33	20.35	N/A	N/A	N/A	N/A	17.00	N/A	N/A	19.73	N/A	17.92	0.30
Sm	3.61	N/A	2.82	3.54	2.98	N/A	N/A	N/A	N/A	3.10	N/A	N/A	3.64	N/A	3.42	0.26
Eu	1.11	N/A	1.12	1.14	1.15	N/A	N/A	N/A	N/A	1.09	N/A	N/A	1.30	N/A	0.95	0.06
Gd	2.97	N/A	2.88	2.75	2.49	N/A	N/A	N/A	N/A	2.87	N/A	N/A	3.06	N/A	2.97	0.07
Dy	2.36	N/A	1.96	2.45	2.07	N/A	N/A	N/A	N/A	1.54	N/A	N/A	2.40	N/A	2.00	0.13
Er	1.44	N/A	1.31	1.39	1.16	N/A	N/A	N/A	N/A	0.64	N/A	N/A	1.36	N/A	1.39	0.16
Yb	1.34	N/A	1.27	1.77	1.11	N/A	N/A	N/A	N/A	0.71	N/A	N/A	1.23	N/A	1.44	0.20
Hf	2.03	N/A	2.78	2.35	2.32	N/A	N/A	N/A	N/A	1.69	N/A	N/A	2.58	N/A	2.54	0.12
Ta	0.17	N/A	0.22	0.24	0.29	N/A	N/A	N/A	N/A	0.27	N/A	N/A	0.23	N/A	0.18	0.04
Pb	4.57	N/A	5.08	5.08	5.80	N/A	N/A	N/A	N/A	4.15	N/A	N/A	4.39	N/A	4.63	0.17
Th	1.30	N/A	1.94	1.75	1.82	N/A	N/A	N/A	N/A	1.46	N/A	N/A	1.68	N/A	1.82	0.11
U	0.46	N/A	0.47	0.47	0.60	N/A	N/A	N/A	N/A	0.38	N/A	N/A	0.51	N/A	0.51	0.04

	BRVB	BRVB	BRVB	BRVB	BRVB	BRVB	BRVB	BRVB	BRVB	BRVB	BRVB	BRVB	BRVB	BRVB	s.d.
INC#	1	3	4	5	6	8	9	10	11	13	18	20	21	22	
wt%															
SiO$_2$	48.76	49.64	49.12	49.26	49.05	49.23	53.11	49.47	48.35	49.67	49.08	50.96	48.27	48.49	0.17
TiO$_2$	1.29	1.47	1.36	1.34	1.34	1.45	2.37	1.36	1.35	1.31	1.33	1.42	1.44	1.32	0.03
Al$_2$O$_3$	17.81	15.97	16.28	17.50	16.42	16.92	14.18	15.51	16.57	15.78	16.95	15.41	18.48	16.43	0.08
FeO^T	9.39	9.39	9.39	9.39	9.39	9.39	9.39	9.39	9.39	9.39	9.39	9.39	9.39	9.39	0.06
MnO	0.12	0.13	0.13	0.14	0.14	0.14	0.13	0.14	0.13	0.15	0.14	0.12	0.14	0.15	0.01
MgO	7.44	7.35	7.52	7.28	7.45	6.95	6.99	7.15	7.19	8.09	7.21	7.26	6.67	7.28	0.03
CaO	8.67	9.25	9.59	9.46	9.80	9.85	7.99	9.64	9.24	9.59	9.46	9.37	9.91	9.35	0.03
Na$_2$O	3.75	3.27	3.31	3.38	3.32	3.77	2.91	3.27	3.60	3.54	3.49	3.34	3.67	3.24	0.07
K$_2$O	1.25	1.02	1.01	1.05	0.96	1.13	1.66	0.98	1.04	0.93	0.94	1.18	1.13	0.95	0.02
P$_2$O$_5$	0.30	0.32	0.29	0.32	0.29	0.35	0.51	0.30	0.28	0.26	0.29	0.27	0.33	0.28	0.01
S	0.14	0.19	0.16	0.19	0.20	0.17	0.01	0.20	0.19	0.17	0.17	0.04	0.16	0.20	0.002
Cl	0.038	0.048	0.049	0.049	0.049	0.049	0.056	0.050	0.049	0.039	0.039	0.038	0.049	0.04	0.002
CO$_2$ (ppm)	657	748	595	644	0	287	403	410	619	419	551	455	123	560	34
H$_2$O	1.00	2.01	1.82	0.71	1.68	0.63	0.57	2.61	2.70	1.12	1.57	1.07	0.38	2.89	0.10
% PEC	6.85	6.87	4.79	3.55	3.87	3.16	6.53	2.01	2.57	4.77	2.88	7.67	3.23	2.78	
Fo	85.0	84.4	84.8	84.4	84.7	84.2	83.5	84.0	84.5	85.9	84.3	84.2	83.6	84.2	
ppm															
Li	N/A	10.77	10.13	N/A	10.19	N/A	N/A	12.11	9.86	N/A	16.23	N/A	0.26	10.88	1.70
B	N/A	6.17	16.19	N/A	5.28	N/A	N/A	114.73	4.86	N/A	11.14	N/A	10.81	4.25	2.80
Sc	N/A	36.50	30.06	N/A	31.16	N/A	N/A	33.44	29.58	N/A	37.74	N/A	48.40	27.67	1.43
V	N/A	262	230	N/A	249	N/A	N/A	235	239	N/A	310	N/A	408	240	13
Rb	N/A	21.73	18.91	N/A	19.68	N/A	N/A	26.62	18.56	N/A	25.51	N/A	32.25	19.88	0.53
Sr	N/A	456	457	N/A	453	N/A	N/A	454	437	N/A	469	N/A	326	455	7
Y	N/A	18.88	18.69	N/A	18.69	N/A	N/A	17.31	17.81	N/A	19.29	N/A	33.83	17.25	0.74
Zr	N/A	110	107	N/A	103	N/A	N/A	102	99	N/A	112	N/A	200	99	5
Nb	N/A	6.77	6.77	N/A	6.66	N/A	N/A	7.43	6.77	N/A	7.63	N/A	11.80	6.91	0.33
Ba	N/A	412	359	N/A	361	N/A	N/A	386	347	N/A	425	N/A	548	366	7
La	N/A	14.20	13.56	N/A	14.08	N/A	N/A	13.98	13.20	N/A	16.37	N/A	23.82	13.67	0.22
Ce	N/A	35.99	32.43	N/A	32.93	N/A	N/A	33.25	32.71	N/A	43.15	N/A	51.57	33.63	0.70
Pr	N/A	4.45	4.23	N/A	4.16	N/A	N/A	4.32	4.07	N/A	5.15	N/A	7.43	4.22	0.10
Nd	N/A	20.63	18.70	N/A	18.95	N/A	N/A	20.17	18.27	N/A	20.61	N/A	34.49	20.31	0.43
Sm	N/A	4.23	4.35	N/A	4.00	N/A	N/A	4.38	4.00	N/A	4.67	N/A	7.10	4.16	0.13
Eu	N/A	1.40	1.31	N/A	1.36	N/A	N/A	1.31	1.38	N/A	1.45	N/A	1.99	1.25	0.08
Gd	N/A	3.97	3.92	N/A	3.91	N/A	N/A	3.88	3.73	N/A	4.68	N/A	6.88	3.61	0.21
Dy	N/A	3.53	3.60	N/A	3.46	N/A	N/A	3.57	3.37	N/A	4.28	N/A	6.02	3.82	0.20
Er	N/A	2.12	1.91	N/A	2.05	N/A	N/A	1.85	1.94	N/A	2.13	N/A	3.55	1.79	0.08
Yb	N/A	2.00	1.67	N/A	1.92	N/A	N/A	1.65	1.73	N/A	2.78	N/A	3.21	1.70	0.05
Hf	N/A	2.69	2.56	N/A	2.74	N/A	N/A	2.38	2.31	N/A	2.59	N/A	4.36	2.51	0.13
Ta	N/A	0.38	0.38	N/A	0.32	N/A	N/A	0.34	0.29	N/A	0.42	N/A	0.67	0.34	0.06
Pb	N/A	4.11	3.85	N/A	3.84	N/A	N/A	3.92	3.79	N/A	5.32	N/A	6.75	4.15	0.18
Th	N/A	1.77	1.61	N/A	1.76	N/A	N/A	1.73	1.70	N/A	1.99	N/A	2.67	1.80	0.12
U	N/A	0.61	0.54	N/A	0.63	N/A	N/A	0.63	0.61	N/A	0.65	N/A	1.00	0.62	0.05

	BPPC	BPPC	BPPC	BPPC	BPPC	BPPC	BPPC	BPPC	BPPC	BPPC	BPPC	BPPC	BPPC	BPPC	s.d.
INC#	1	2	3	5	7	10	11	12	13	15	17a	17b	18	19	
wt%															
SiO_2	50.52	50.21	50.13	49.64	50.62	50.17	50.27	50.68	51.03	51.55	50.39	50.31	50.22	50.44	0.29
TiO_2	0.78	0.78	0.71	0.76	0.80	0.79	0.77	0.81	0.76	1.01	0.80	0.80	0.82	0.77	0.02
Al_2O_3	16.42	16.52	16.65	16.64	16.47	16.48	16.56	16.47	15.38	15.59	16.24	16.76	16.72	16.72	0.13
FeO^T	7.68	7.68	7.68	7.68	7.68	7.68	7.68	7.68	7.68	7.68	7.68	7.68	7.68	7.68	0.07
MnO	0.13	0.11	0.10	0.12	0.12	0.11	0.13	0.11	0.13	0.18	0.11	0.12	0.14	0.14	0.01
MgO	7.88	8.40	8.43	8.26	7.98	8.04	8.06	8.13	7.55	8.20	8.15	8.19	7.75	7.75	0.18
CaO	10.79	10.71	11.06	11.52	10.77	11.01	10.77	10.89	11.34	11.34	10.93	10.69	11.12	10.89	0.10
Na_2O	2.71	2.68	2.58	2.38	2.73	2.69	2.67	2.82	2.63	3.04	2.77	2.71	2.85	2.80	0.11
K_2O	0.31	0.30	0.24	0.19	0.33	0.31	0.35	0.32	0.30	0.45	0.31	0.30	0.36	0.31	0.02
P_2O_5	0.18	0.17	0.18	0.16	0.19	0.19	0.19	0.18	0.21	0.22	0.19	0.18	0.19	0.18	0.01
S	0.12	0.11	0.11	0.13	0.12	0.12	0.12	0.12	0.12	0.07	0.11	0.11	0.13	0.11	0.003
Cl	0.039	0.039	0.037	0.040	0.040	0.039	0.040	0.039	0.030	0.050	0.039	0.038	0.040	0.040	0.001
CO_2 (ppm)	908	878	954	758	1300	1008	1012	672	892	85	876	1011	954	735	52
H_2O	2.50	2.32	2.12	2.54	2.19	2.43	2.44	1.79	2.85	0.61	2.32	2.15	2.05	2.21	0.11
% PEC	1.48	3.37	9.49	1.47	0.82	2.59	1.13	5.00	1.79	1.26	3.17	4.40	0.82	0.87	
Fo	87	88	88	88	87	87	87	88	86	88	88	88	87	87	
ppm															
Li	6.14	6.06	6.89	N/A	N/A	5.80	7.25	N/A	4.00	6.99	7.35	N/A	7.04	N/A	1.36
B	1.74	2.69	1.31	N/A	N/A	1.32	2.30	N/A	4.61	3.43	N/A	N/A	4.34	N/A	1.77
Sc	35.87	34.04	31.48	N/A	N/A	33.30	33.74	N/A	35.34	40.37	36.71	N/A	36.15	N/A	1.45
V	211	212	215	N/A	N/A	211	208	N/A	209	238	210	N/A	210	N/A	13
Rb	5.09	4.58	2.72	N/A	N/A	4.46	4.95	N/A	5.50	6.75	4.74	N/A	6.16	N/A	0.50
Sr	455	447	345	N/A	N/A	456	432	N/A	458	378	445	N/A	455	N/A	6
Y	14.99	15.36	13.39	N/A	N/A	16.18	15.15	N/A	15.88	18.39	16.19	N/A	16.12	N/A	0.78
Zr	58.30	60.60	41.62	N/A	N/A	54.75	58.19	N/A	58.42	68.02	59.08	N/A	61.90	N/A	3.93
Nb	1.41	1.42	0.83	N/A	N/A	1.39	1.37	N/A	1.30	1.71	1.40	N/A	1.65	N/A	0.34
Ba	111	102	61	N/A	N/A	102	105	N/A	119	136	105	N/A	118	N/A	4
La	5.14	5.23	3.79	N/A	N/A	5.33	5.60	N/A	5.74	6.29	4.99	N/A	5.61	N/A	0.20
Ce	13.10	12.54	9.59	N/A	N/A	12.52	13.01	N/A	12.91	16.22	13.36	N/A	13.57	N/A	0.36
Pr	1.88	1.66	1.23	N/A	N/A	1.66	1.70	N/A	1.85	2.00	1.95	N/A	1.92	N/A	0.13
Nd	9.04	8.29	6.11	N/A	N/A	8.78	8.74	N/A	8.48	9.52	9.26	N/A	8.53	N/A	0.24
Sm	2.37	2.56	1.87	N/A	N/A	2.16	1.96	N/A	2.42	3.00	1.32	N/A	2.85	N/A	0.12
Eu	0.99	0.78	0.65	N/A	N/A	0.75	0.83	N/A	0.82	0.85	0.87	N/A	0.92	N/A	0.06
Gd	2.48	2.62	1.77	N/A	N/A	2.77	2.64	N/A	3.73	2.42	2.48	N/A	2.68	N/A	0.12
Dy	2.78	2.38	2.27	N/A	N/A	2.75	2.73	N/A	2.74	3.16	2.88	N/A	2.43	N/A	0.08
Er	1.57	1.63	1.16	N/A	N/A	1.88	1.62	N/A	1.71	1.91	2.47	N/A	1.76	N/A	0.18
Yb	1.70	1.56	1.54	N/A	N/A	1.75	1.86	N/A	2.02	1.75	1.62	N/A	1.62	N/A	0.10
Hf	1.66	1.52	1.16	N/A	N/A	1.61	1.44	N/A	1.90	1.51	1.95	N/A	1.88	N/A	0.13
Ta	0.09	0.06	N/A	N/A	N/A	0.05	0.13	N/A	0.04	0.12	0.07	N/A	0.10	N/A	0.03
Pb	1.64	1.56	1.02	N/A	N/A	1.50	1.51	N/A	1.96	2.33	1.39	N/A	1.76	N/A	0.18
Th	0.54	0.48	0.30	N/A	N/A	0.45	0.60	N/A	0.46	0.69	0.62	N/A	0.60	N/A	0.08
U	0.18	0.17	0.01	N/A	N/A	0.16	0.19	N/A	0.25	0.22	0.15	N/A	0.19	N/A	0.03

INC#	CC 1	CC 2	CC 6	CC 7	CC 9a	CC 9b	CC 4a	CC 4b	CC 10	CC 13	CC 16a	CC 16b	CC 18	avg s.d.
wt%														
SiO_2	51.11	50.20	49.91	50.71	51.11	50.76	50.63	50.88	50.75	52.64	49.96	49.87	50.88	0.34
TiO_2	0.87	0.94	0.86	0.83	0.81	0.80	0.85	0.83	0.81	0.81	0.83	0.84	0.83	0.03
Al_2O_3	16.65	17.98	16.55	16.65	16.27	16.49	16.82	16.59	16.82	16.71	16.47	16.53	16.44	0.27
FeO^T	6.88	6.88	6.88	6.88	6.88	6.88	6.88	6.88	6.88	6.88	6.88	6.88	6.88	0.13
MnO	0.09	0.09	0.08	0.09	0.09	0.08	0.08	0.09	0.08	0.11	0.10	0.09	0.09	0.01
MgO	7.93	7.47	8.44	8.37	8.38	8.47	7.88	7.95	8.28	7.67	8.25	8.27	8.18	0.75
CaO	10.10	9.42	10.67	10.13	10.15	9.73	10.21	9.90	10.12	8.43	10.68	10.73	10.18	0.22
Na_2O	3.24	3.43	2.89	2.77	3.02	2.85	3.17	3.03	3.02	3.52	2.97	2.93	3.07	0.16
K_2O	0.86	0.84	0.72	0.82	0.79	0.82	0.81	0.88	0.82	1.27	0.68	0.68	0.79	0.03
P_2O_5	0.16	0.18	0.16	0.16	0.15	0.15	0.16	0.15	0.16	0.15	0.16	0.15	0.15	0.01
S	0.09	0.09	0.09	0.09	0.09	0.05	0.09	0.09	0.09	0.08	0.09	0.09	0.09	0.003
Cl	0.036	0.038	0.037	0.034	0.040	0.038	0.038	0.035	0.038	0.036	0.037	0.037	0.036	0.003
CO_2 (ppm)	922	940	1302	1248	0	789	531	640	1151	612	1431	1464	1266	85
H_2O	2.58	3.05	3.33	3.10	2.84	3.46	3.00	3.30	2.74	2.29	3.49	3.52	2.99	0.23
% PEC	6.11	1.70	8.02	0.81	7.49	7.68	6.06	6.76	7.42	6.46	6.05	6.33	6.49	
Fo	90	89	90	90	90	90	90	90	90	90	90	90	90	
ppm														
Li	N/A	N/A	5.85	9.67	15.71	N/A	7.69	7.20	N/A	8.60	24.63	4.83	N/A	1.23
B	N/A	N/A	7.20	5.42	6.52	N/A	5.10	2.29	N/A	5.67	9.41	3.83	N/A	2.93
Sc	N/A	N/A	29.83	30.52	31.25	N/A	26.88	26.93	N/A	25.40	23.61	29.22	N/A	1.36
V	N/A	N/A	196	206	177	N/A	193	174	N/A	189	162	192	N/A	11
Rb	N/A	N/A	10.20	17.00	13.96	N/A	13.48	13.65	N/A	12.56	26.23	9.41	N/A	0.71
Sr	N/A	N/A	347	370	367	N/A	343	346	N/A	325	349	320	N/A	8
Y	N/A	N/A	15.38	14.10	15.63	N/A	13.02	13.19	N/A	12.48	12.73	13.24	N/A	0.86
Zr	N/A	N/A	80.98	75.69	89.69	N/A	68.49	71.84	N/A	68.56	73.03	67.73	N/A	4.29
Nb	N/A	N/A	4.46	4.34	4.05	N/A	3.95	4.04	N/A	3.80	3.90	4.16	N/A	0.33
Ba	N/A	N/A	178	205	206	N/A	189	198	N/A	182	280	157	N/A	5
La	N/A	N/A	8.38	7.81	8.05	N/A	7.12	7.54	N/A	6.96	8.77	6.57	N/A	0.47
Ce	N/A	N/A	17.97	17.59	18.42	N/A	16.72	16.82	N/A	16.13	18.84	15.44	N/A	0.77
Pr	N/A	N/A	2.50	2.31	2.74	N/A	2.28	2.54	N/A	2.23	2.32	2.17	N/A	0.08
Nd	N/A	N/A	10.96	10.34	15.03	N/A	10.61	11.35	N/A	10.11	11.53	9.20	N/A	0.37
Sm	N/A	N/A	2.22	2.61	2.06	N/A	2.30	2.47	N/A	2.51	2.31	2.26	N/A	0.22
Eu	N/A	N/A	1.03	0.90	1.08	N/A	0.81	0.79	N/A	0.70	0.79	0.79	N/A	0.09
Gd	N/A	N/A	3.04	2.74	2.87	N/A	2.54	2.75	N/A	2.17	2.33	2.30	N/A	0.24
Dy	N/A	N/A	2.63	2.56	2.65	N/A	2.30	3.03	N/A	2.58	2.35	2.45	N/A	0.11
Er	N/A	N/A	1.66	1.38	2.46	N/A	1.40	1.21	N/A	1.29	1.42	1.61	N/A	0.10
Yb	N/A	N/A	1.43	1.59	1.74	N/A	1.28	1.55	N/A	1.33	1.31	1.30	N/A	0.14
Hf	N/A	N/A	1.77	1.92	3.45	N/A	1.58	1.91	N/A	1.45	1.82	1.70	N/A	0.15
Ta	N/A	N/A	0.28	0.25	0.43	N/A	0.24	0.18	N/A	0.38	0.24	0.27	N/A	0.03
Pb	N/A	N/A	2.40	2.91	2.86	N/A	2.84	2.88	N/A	2.46	6.59	1.66	N/A	0.13
Th	N/A	N/A	1.29	1.64	1.65	N/A	1.55	1.65	N/A	1.53	2.27	1.12	N/A	0.08
U	N/A	N/A	0.35	0.51	0.54	N/A	0.46	0.58	N/A	0.46	0.76	0.37	N/A	0.04

BORG	BORG	BORG	BORG	BORG	BORG	BORG	BORG	BORG A20-2	BORG	BORG	BORG A24-2	BORG	BORG AA1 c	BORG	BORG	s.d.
INC #	A1	A3	A5	A6 c	A9	A10	A18	2	A23	A24	2	A28	c	AA4	AA5	
wt%																
SiO_2	47.78	48.41	48.65	49.61	48.20	48.45	49.08	49.31	48.70	48.31	48.46	48.41	49.93	49.15	49.42	0.41
TiO_2	0.66	0.67	0.71	0.82	0.64	0.66	0.72	0.80	0.72	0.70	0.68	0.69	0.83	0.85	0.74	0.02
Al_2O_3	16.95	16.75	16.23	19.21	16.35	17.47	15.72	17.87	16.30	15.89	16.17	17.03	16.88	17.90	15.88	0.28
FeO^T	8.54	8.54	8.54	8.54	8.54	8.54	8.54	8.54	8.54	8.54	8.54	8.54	8.54	8.54	8.54	0.11
MnO	0.12	0.11	0.12	0.12	0.11	0.10	0.09	0.13	0.10	0.08	0.10	0.10	0.12	0.12	0.09	0.01
MgO	9.80	9.73	9.51	6.97	9.77	9.69	9.47	7.44	8.99	10.32	10.28	9.67	8.14	7.90	9.34	0.14
CaO	9.76	9.96	9.97	8.73	10.02	9.03	10.13	9.16	10.02	10.73	10.62	10.38	8.76	8.71	9.99	0.11
Na_2O	2.63	2.48	2.48	2.46	2.41	2.73	2.41	3.27	2.56	2.36	2.49	2.46	2.74	3.22	2.47	0.14
K_2O	0.50	0.47	0.51	0.55	0.49	0.50	0.48	0.52	0.50	0.38	0.40	0.46	0.57	0.54	0.48	0.02
P_2O_5	0.10	0.07	0.09	0.13	0.07	0.08	0.10	0.10	0.10	0.09	0.09	0.08	0.11	0.11	0.11	0.01
S	0.10	0.11	0.12	0.15	0.12	0.12	0.12	0.11	0.12	0.11	0.12	0.12	0.10	0.21	0.11	0.004
Cl	0.05	0.05	0.05	0.05	0.05	0.06	0.05	0.04	0.05	0.06	0.06	0.05	0.04	0.04	0.05	0.002
CO_2 (ppm)	518	853	1114	724	945	887	1493	841	1104	1123	950	793	786	840	984	53
H_2O	3.00	2.67	3.07	2.74	3.27	2.62	3.11	2.73	3.34	2.45	2.04	2.04	3.26	2.75	2.80	0.12
PEC	9.80	10.13	9.27	9.25	9.20	19.03	11.61	3.15	13.96	13.95	12.61	14.58	8.99	5.27	12.74	
Fo	88.6	88.4	88.2	83.8	88.5	88.4	88.0	85.4	87.5	89.1	89.1	88.4	86.2	86.1	87.9	
ppm																
Li	7.60	N/A	5.76	N/A	5.43	N/A	10.48	6.51	5.01	6.75	N/A	7.74	6.01	N/A	7.66	1.18
B	2.87	N/A	3.36	N/A	4.41	N/A	3.82	6.91	2.49	4.09	N/A	4.99	3.72	N/A	4.98	1.77
Sc	38.35	N/A	35.93	N/A	37.47	N/A	41.11	29.58	35.29	41.35	N/A	39.69	30.05	N/A	39.37	1.60
V	272	N/A	245	N/A	250	N/A	339	227	236	288	N/A	305	225	N/A	280	16
Rb	5.20	N/A	4.25	N/A	5.95	N/A	6.91	8.83	4.37	5.63	N/A	5.78	4.58	N/A	6.93	0.63
Sr	475	N/A	436	N/A	443	N/A	466	642	337	477	N/A	434	382	N/A	631	9
Y	12.58	N/A	11.99	N/A	12.30	N/A	12.56	12.08	11.77	13.52	N/A	13.71	11.24	N/A	17.19	1.11
Zr	51.88	N/A	48.59	N/A	54.42	N/A	50.32	54.97	47.73	58.74	N/A	53.78	48.40	N/A	71.87	4.25
Nb	1.98	N/A	1.82	N/A	2.19	N/A	2.26	2.49	1.78	2.40	N/A	1.97	2.07	N/A	3.42	0.45
Ba	147	N/A	133	N/A	147	N/A	160	264	110	153	N/A	138	123	N/A	223	4
La	4.96	N/A	4.65	N/A	5.52	N/A	4.95	7.93	4.00	5.83	N/A	5.03	4.57	N/A	7.55	0.37
Ce	12.07	N/A	11.48	N/A	13.39	N/A	13.84	17.65	10.58	14.32	N/A	13.61	11.64	N/A	17.82	0.85
Pr	1.68	N/A	1.51	N/A	1.84	N/A	1.72	2.28	1.45	1.96	N/A	1.72	1.52	N/A	2.40	0.35
Nd	7.94	N/A	8.05	N/A	8.56	N/A	8.16	10.76	7.22	9.69	N/A	8.15	7.43	N/A	11.35	0.51
Sm	2.21	N/A	2.58	N/A	2.26	N/A	2.01	2.27	1.85	2.63	N/A	2.11	1.94	N/A	2.67	0.37
Eu	0.85	N/A	0.76	N/A	0.89	N/A	0.89	1.00	0.73	0.93	N/A	0.82	0.74	N/A	1.16	0.41
Gd	2.51	N/A	1.96	N/A	2.40	N/A	2.23	2.45	2.06	2.73	N/A	3.13	1.86	N/A	3.07	0.37
Dy	2.18	N/A	2.40	N/A	2.43	N/A	2.50	2.75	2.22	2.84	N/A	2.44	2.00	N/A	3.38	0.42
Er	1.42	N/A	1.39	N/A	1.33	N/A	1.35	1.41	1.31	1.70	N/A	1.27	1.18	N/A	2.01	0.65
Yb	1.49	N/A	1.27	N/A	1.33	N/A	1.30	1.45	1.27	1.57	N/A	1.36	1.07	N/A	1.90	0.40
Hf	1.22	N/A	1.27	N/A	1.37	N/A	1.34	1.51	1.26	1.40	N/A	1.55	1.25	N/A	1.80	3.86
Ta	0.10	N/A	0.11	N/A	0.11	N/A	0.11	0.14	0.10	0.14	N/A	0.13	0.10	N/A	0.16	12.69
Pb	2.29	N/A	2.06	N/A	2.18	N/A	3.20	4.30	1.51	2.44	N/A	2.12	1.83	N/A	2.98	1.34
Th	0.60	N/A	0.58	N/A	0.55	N/A	0.60	1.28	0.49	0.62	N/A	0.62	0.54	N/A	1.01	1.01
U	0.24	N/A	0.26	N/A	0.51	N/A	0.31	0.55	0.16	0.30	N/A	0.27	0.23	N/A	0.37	0.04

BAS-44	B1	B2	B3	B6	B6-2	B7	B9	B17	B18	B20	B22	B23	B24	B25	BB2	BB3	BB4	s.d.
wt%																		
SiO_2	48.89	47.78	48.23	49.50	48.91	49.04	48.51	48.61	49.08	49.01	48.68	49.12	48.78	49.64	48.59	49.15	49.04	0.35
TiO_2	0.95	0.93	0.96	0.95	0.96	0.93	0.95	0.95	0.93	0.95	0.93	0.93	0.97	0.95	0.97	0.96	0.97	0.02
Al_2O_3	16.66	17.81	16.83	15.88	16.50	16.48	16.96	16.43	16.13	16.13	16.50	16.27	16.65	16.37	16.62	16.61	17.04	0.19
FeO^T	8.88	8.88	8.88	8.88	8.88	8.88	8.88	8.88	8.88	8.88	8.88	8.88	8.88	8.88	8.88	8.88	8.88	0.08
MnO	0.13	0.13	0.11	0.13	0.11	0.13	0.11	0.12	0.12	0.12	0.13	0.12	0.11	0.13	0.11	0.12	0.12	0.01
MgO	9.52	9.64	10.13	9.78	9.72	9.86	9.55	10.04	10.21	9.63	10.02	9.82	9.59	10.43	9.76	9.33	9.38	0.07
CaO	10.48	10.48	10.57	10.38	10.53	10.55	10.66	10.44	10.08	10.57	10.45	10.41	10.61	10.66	10.64	10.72	10.34	0.11
Na_2O	2.81	2.82	2.72	2.92	2.91	2.54	2.83	2.83	3.02	2.88	2.80	2.76	2.81	1.47	2.80	3.03	2.65	0.05
K_2O	0.27	0.29	0.26	0.32	0.28	0.27	0.29	0.30	0.27	0.29	0.27	0.29	0.29	0.27	0.27	0.29	0.34	0.01
P_2O_5	0.17	0.14	0.16	0.16	0.15	0.16	0.15	0.15	0.16	0.16	0.15	0.16	0.16	0.16	0.15	0.16	0.15	0.01
S	0.11	0.10	0.11	0.11	0.11	0.12	0.12	0.11	0.12	0.12	0.11	0.12	0.12	0.10	0.12	0.11	0.10	0.00
Cl	0.026	0.031	0.029	0.025	0.024	0.026	0.029	0.025	0.029	0.025	0.030	0.025	0.027	0.031	0.033	0.025	0.028	0.00
CO_2 (ppm)	494	413	554	446	575	505	654	557	835	615	489	357	784	336	649	90	334	37
H_2O	1.14	1.02	1.04	1.01	0.93	1.08	0.99	1.16	1.02	1.26	1.11	1.14	1.07	0.95	1.12	0.64	1.00	0.04
PEC	5.85	7.57	8.19	6.81	6.87	6.91	6.72	6.84	6.21	7.09	6.82	7.43	6.98	7.83	7.05	4.81	6.56	
Fo	87.4	87.7	88.2	87.7	87.7	87.7	87.5	88.1	88.3	87.6	88.0	87.7	87.5	87.7	87.8	87.3	87.1	
ppm																		
Li	8.53	N/A	9.37	5.26	5.75	0.63	N/A	6.49	6.23	5.72	7.27	6.21	6.18	N/A	5.84	2.35	N/A	1.49
B	5.75	N/A	2.89	2.55	2.18	2.13	N/A	1.96	2.05	2.04	1.61	3.73	1.72	N/A	2.65	1.67	N/A	1.52
Sc	57.5	N/A	45.2	38.8	39.9	39.0	N/A	43.3	34.9	38.8	38.7	43.2	36.8	N/A	35.8	38.0	N/A	2.9
V	236	N/A	246	211	215	211	N/A	229	180	215	263	222	218	N/A	226	226	N/A	16
Rb	4.47	N/A	7.25	5.19	4.30	4.72	N/A	4.72	4.27	4.54	5.15	5.61	4.59	N/A	4.76	5.93	N/A	1.01
Sr	391	N/A	393	399	408	411	N/A	384	378	413	380	472	404	N/A	396	423	N/A	8
Y	19.59	N/A	19.44	17.88	18.48	19.53	N/A	18.99	17.97	17.72	c	19.35	18.11	N/A	17.99	18.00	N/A	3.00
Zr	79.0	N/A	83.5	77.3	76.6	84.3	N/A	77.6	74.3	72.5	78.9	79.7	74.4	N/A	77.6	79.2	N/A	6.2
Nb	2.57	N/A	2.98	2.67	2.93	2.84	N/A	2.65	2.36	2.59	2.62	3.27	2.63	N/A	2.48	2.79	N/A	1.02
Ba	112	N/A	125	118	111	115	N/A	107	98	108	97	177	109	N/A	104	129	N/A	4
La	7.43	N/A	7.43	7.50	7.57	7.15	N/A	6.96	7.20	7.52	7.26	7.89	7.17	N/A	7.56	7.85	N/A	0.79
Ce	20.6	N/A	22.1	18.6	19.8	18.7	N/A	19.4	17.5	19.4	19.2	21.0	19.2	N/A	20.2	20.5	N/A	1.4
Pr	2.63	N/A	2.83	2.59	2.62	2.72	N/A	2.69	2.58	2.71	2.58	2.83	2.72	N/A	2.61	2.66	N/A	0.83
Nd	12.0	N/A	12.3	11.5	13.0	12.5	N/A	11.9	12.1	12.0	12.2	13.7	11.6	N/A	12.4	12.7	N/A	1.0
Sm	3.0	N/A	2.4	3.0	3.1	3.1	N/A	2.7	2.6	2.9	2.6	3.1	2.8	N/A	3.0	2.9	N/A	1.0
Eu	0.86	N/A	1.09	1.07	1.05	0.97	N/A	1.07	0.94	0.99	1.05	1.12	1.05	N/A	1.18	0.90	N/A	0.85
Gd	3.14	N/A	3.23	3.09	3.22	3.29	N/A	3.18	3.14	3.25	3.20	3.22	2.86	N/A	3.17	3.38	N/A	0.88
Dy	3.34	N/A	3.66	3.36	3.45	3.61	N/A	3.80	3.04	3.11	3.33	3.15	3.31	N/A	3.25	0.00	N/A	1.72
Er	2.22	N/A	2.10	2.12	2.16	1.93	N/A	2.28	2.20	2.30	2.18	2.30	2.17	N/A	2.19	2.33	N/A	0.92
Yb	2.38	N/A	2.13	2.01	2.01	1.91	N/A	2.10	2.14	2.14	1.76	2.20	2.18	N/A	2.02	2.03	N/A	0.82
Hf	1.95	N/A	2.14	1.90	2.02	1.99	N/A	1.94	1.86	1.94	1.97	2.28	1.99	N/A	1.98	1.91	N/A	1.93
Ta	0.15	N/A	0.14	0.15	0.15	0.16	N/A	0.17	0.13	0.15	0.16	0.13	0.12	N/A	0.15	0.17	N/A	3.45
Pb	1.46	N/A	2.07	1.65	1.38	1.35	N/A	1.55	1.62	1.42	1.44	2.00	1.40	N/A	1.46	1.74	N/A	11.91
Th	0.54	N/A	0.61	0.60	0.67	0.59	N/A	0.57	0.58	0.53	0.58	0.62	0.56	N/A	0.60	0.66	N/A	1.71
U	0.20	N/A	0.26	0.21	0.22	0.19	N/A	0.23	0.19	0.18	0.25	0.25	0.19	N/A	0.20	0.29	N/A	0.02

B.2. Boron Isotope Compositions

Sample	$\delta^{11}B$	2SE		Sample	$\delta^{11}B$	2SE
LCC-9-S-06	-12.63	1.30		BRVB-S-11	-4.69	1.20
LCC-9-S-07	-11.67	1.24		BRVB-S-14	-5.20	1.08
LCC-9-S-01	-11.49	1.48		BRVB-S-01	-4.62	1.28
LCC-9-S-09	-8.79	1.03		BRVB-S-09	-5.38	1.37
LCC-2-S-07	-5.30	1.86		BPB-S-02	-5.84	1.61
LCC-2-S-03	-7.98	1.36		BPB-S-04	-3.90	1.62
LCC-2-S-06	-13.09	1.51		BPB-S-07	-5.53	1.48
LCC-2-S-10	-8.18	1.32		BRM-S-08	-3.60	1.92
BORG-S-01	-3.50	2.24		BRM-S-09	-3.17	1.61
BORG-S-04	-4.21	1.75		BRM-S-03	-2.10	1.54
BORG-S-10	-3.42	1.81		BRM-S-05	-0.65	1.75
BORG-S-9	1.52	1.68		BPPC-S-04	-4.90	1.60
BORG-S-6	-0.82	1.98		BPPC-S-07	-5.40	1.60
BORG-S-13	-5.43	1.68		BPPC-S-11	-5.28	1.71
BBL-S-11	-2.89	2.35		BPPC-S-01	-4.23	2.67
BBL-S-06	-7.21	4.16		BAS-44-S-08	-3.22	4.36
BBL-S-08	-2.78	2.57		BAS-44-S-06	-6.75	1.55
BBL-S-04	-5.10	3.21		BAS-44-S-01	-2.78	2.71
BBL-S-05	-3.24	1.10		BAS-44-S-01	-5.38	2.90

B.3. Radiogenic Isotope Compositions

Sample ID	BPCB-1	BORG-1	BPB-1	BBL-05	BAS-44-01	BRVB-1
208Pb/204Pb	38.4640093	38.5386438	38.612363	38.6502638	38.56384767	38.6456054
2SE	0.0027	0.00226	0.00382	0.00206	0.00242	0.00218
207Pb/204Pb	15.5897941	15.6012692	15.612799	15.6183439	15.60589745	15.6166351
2SE	0.001028	0.001022	0.001204	0.000878	0.000878	0.000832
206Pb/204Pb	18.8429231	18.8979534	18.954407	18.9642892	18.92165526	18.977124
2SE	0.00118	0.001138	0.00103	0.001004	0.00091	0.000884
143Nd/144Nd	0.512926	0.51286409	0.5128272	0.51285886	0.512948154	0.51283266
2SE	0.00000594	0.00000642	6.46E-06	0.00000582	0.0000056	0.00000644
176Hf/177Hf	0.28305201	0.28305515	0.2830588	0.28305717	0.283093557	0.28303467
2SE	0.00000722	0.00000646	8.86E-06	0.00000626	0.00000622	0.00000532
87Sr/86Sr	0.70339631	0.70381332	0.7038772	0.70393874	0.703528686	0.70398503
2SE	0.000006	0.000008	0.000008	0.000007	0.000008	0.000008

APPENDIX C

CHAPTER IV SUPPLEMENTARY MATERIALS

C.1. PEC Corrected Melt Inclusion Compositions

Data in this table represent individual melt inclusion compositions that have been corrected for Fe loss and post entrapment crystallization (PEC). Major elements were restored using Petrolog 3.1.1 (Danyushevsky and Plechov, 2011). H_2O, Cl, S, and trace elements were restored by the same percent as K_2O because they are incompatible with olivine. H_2O values in this table are not corrected for H^+ diffusive loss (i.e. they are different from values shown Fig. 4.6). CO_2 values were corrected using methods described in the text modified from Wallace et al. (2015) and Aster et al. (in prep). Analyzed CO_2 concentrations for these inclusions are reported in C.2. FeO and Fe_2O_3 were calculated using Petrolog 3.1.1 assuming an fO_2 of QFM +1. Temperatures are calculated by Petrolog 3.1.1 and represent temperatures of melt inclusion entrapment. Major element standard deviations represent an average of those calculated for each melt inclusion based on three EPMA point analyses. Trace element standard deviations are also an average from individual inclusions based on the methods of Loewen and Kent (2012).

LCC	9-01	9-02	9-06	9-07	09-09	9-04	9-04(2)	9-10	9-16(1)	9-16(2)	9-18(1)	S.D.
wt%												
SiO$_2$	50.64	49.76	49.47	50.23	50.28	50.17	50.41	50.29	49.53	49.43	50.40	0.34
TiO$_2$	0.84	0.91	0.83	0.80	0.77	0.82	0.80	0.78	0.80	0.81	0.80	0.03
Al$_2$O$_3$	16.06	17.37	15.94	16.03	15.88	16.23	16.00	16.21	15.88	15.93	15.85	0.27
Fe$_2$O$_3$	1.05	1.01	1.02	1.01	1.02	1.03	1.03	1.03	1.03	1.02	1.04	
FeO	6.06	6.10	6.09	6.10	6.09	6.08	6.08	6.08	6.08	6.09	6.07	0.13
MnO	0.09	0.09	0.08	0.09	0.08	0.08	0.08	0.08	0.10	0.09	0.09	0.01
MgO	8.93	8.42	9.47	9.41	9.51	8.86	8.94	9.29	9.26	9.28	9.20	0.75
CaO	9.74	9.10	10.27	9.76	9.37	9.85	9.55	9.75	10.30	10.34	9.81	0.22
Na$_2$O	3.13	3.32	2.78	2.67	2.74	3.06	2.92	2.92	2.87	2.82	2.96	0.16
K$_2$O	0.83	0.81	0.69	0.79	0.79	0.78	0.85	0.79	0.66	0.66	0.76	0.03
P$_2$O$_5$	0.16	0.17	0.16	0.15	0.15	0.15	0.15	0.15	0.15	0.14	0.15	0.01
S	0.08	0.09	0.09	0.09	0.05	0.09	0.08	0.09	0.09	0.09	0.09	0.003
Cl	0.034	0.037	0.037	0.034	0.037	0.037	0.034	0.036	0.035	0.036	0.035	0.003
H$_2$O	2.59	3.06	3.35	3.11	3.47	3.02	3.32	2.75	3.51	3.53	3.01	0.25
CO$_2$ (ppm) RESTORED	2180	1011	3298	1252	2101	1371	1727	2912	3030	3101	2792	91
T °C	1254	1247	1260	1260	1267	1251	1254	1260	1255	1255	1258	
Fo	89.7	89.2	90.2	90.0	90.1	89.6	89.6	90.0	90.0	90.0	89.9	
% PEC	9.7	5.0	11.8	4.4	11.5	9.6	10.4	11.2	9.7	10.0	10.2	
ppm												
Li			5.84	9.69	15.76	7.24	7.60		4.84	7.55		1.93
B			7.20	5.43	6.54	2.30	5.04		3.83	5.32		2.83
Sc			29.83	30.58	31.34	27.11	26.57		29.25	28.73		1.58
V			196	206	178	175	190		192	209		12
Rb			10.20	17.03	14.00	13.74	13.32		9.42	11.75		0.69
Sr			347	371	368	349	339		321	331		9
Y			15.37	14.13	15.67	13.28	12.86		13.25	12.37		0.81
Zr			80.96	75.83	89.94	72.31	67.69		67.79	63.42		4.59
Nb			4.46	4.34	4.06	4.07	3.90		4.17	4.10		0.35
Ba			178	206	207	200	186		157	160		6
La			8.38	7.83	8.08	7.59	7.03		6.57	6.44		0.28
Ce			17.96	17.62	18.47	16.93	16.53		15.46	16.09		0.68
Pr			2.50	2.32	2.74	2.55	2.25		2.18	1.99		0.14
Nd			10.96	10.36	15.07	11.42	10.49		9.21	9.66		0.57
Sm			2.22	2.61	2.07	2.48	2.27		2.26	2.05		0.24
Eu			1.03	0.90	1.09	0.80	0.80		0.79	0.81		0.08
Gd			3.04	2.74	2.87	2.77	2.51		2.30	2.65		0.17
Dy			2.63	2.56	2.66	3.05	2.27		2.45	2.27		0.17
Er			1.66	1.38	2.46	1.22	1.39		1.61	1.52		0.12
Yb			1.43	1.60	1.74	1.56	1.27		1.30	1.48		0.12
Hf			1.77	1.92	3.46	1.92	1.56		1.70	1.15		0.18
Ta			0.28	0.25	0.43	0.18	0.24		0.27	0.26		0.05
Pb			2.40	2.91	2.87	2.90	2.80		1.66	2.13		0.20
Th			1.29	1.65	1.66	1.66	1.53		1.12	0.99		0.12
U			0.35	0.51	0.54	0.58	0.46		0.37	0.37		0.05

	LCC-7-02	LCC-7-03	LCC-7-04	LCC-7-05	LCC-7-08	LCC-7-10	S.D.
wt%							
SiO_2	50.23	50.78	50.48	50.75	50.24	50.27	0.23
TiO_2	0.76	0.76	0.78	0.77	0.77	0.78	0.02
Al_2O_3	16.05	15.86	15.84	15.49	15.86	15.68	0.13
Fe_2O_3	0.99	1.04	1.04	1.02	1.02	1.03	
FeO	6.11	6.07	6.07	6.08	6.08	6.08	0.06
MnO	0.07	0.08	0.08	0.09	0.08	0.08	0.01
MgO	9.73	9.50	9.77	9.70	9.03	9.25	0.12
CaO	10.47	10.22	10.63	9.41	10.06	10.18	0.07
Na_2O	2.59	2.95	2.89	2.60	2.92	2.84	0.12
K_2O	0.60	0.65	0.61	0.77	0.69	0.66	0.02
P_2O_5	0.12	0.14	0.13	0.12	0.14	0.14	0.01
S	0.09	0.09	0.08	0.08	0.08	0.07	0.001
Cl	0.038	0.039	0.039	0.037	0.039	0.039	0.001
H_2O	2.36	2.04	1.76	3.34	3.24	3.16	0.16
$CO_{2\ (ppm)}$ RESTORED	2801	2356	N/A	1592	2009	2465	75
T °C	1260	1261	1264	1269	1252	1255	
Fo	90.3	90.2	90.5	90.2	89.7	89.9	
% PEC	13.2	10.3	12.0	10.1	9.5	10.5	
ppm							
Li				17.02	7.11	7.32	1.72
B				4.42	6.37	3.52	2.14
Sc				28.86	29.44	26.14	1.57
V				190	206	220	13
Rb				14.06	13.40	13.18	0.65
Sr				321	338	333	6
Y				13.54	13.84	12.20	0.85
Zr				70.47	72.06	65.83	4.23
Nb				4.02	4.25	4.33	0.34
Ba				195	185	177	5
La				7.39	7.07	6.34	0.23
Ce				15.97	16.51	15.54	0.47
Pr				2.10	2.19	2.04	0.08
Nd				9.08	9.22	9.12	0.39
Sm				2.30	2.49	2.02	0.13
Eu				0.82	0.85	0.75	0.06
Gd				2.53	2.30	2.15	0.22
Dy				2.32	2.63	2.30	0.09
Er				1.35	1.48	1.20	0.09
Yb				1.57	1.38	1.21	0.07
Hf				1.69	1.67	1.65	0.13
Ta				0.19	0.25	0.27	0.03
Pb				3.95	2.82	2.42	0.19
Th				1.27	1.18	1.01	0.09
U				0.43	0.43	0.38	0.03

	LCC-6-01	LCC-6-02	LCC-6-06	LCC-6-07	LCC-6-08	LCC-6-10	S.D.
wt%							
SiO$_2$	49.92	51.00	50.05	50.57	50.29	53.65	*0.31*
TiO$_2$	0.82	0.81	0.85	0.84	0.82	0.70	*0.02*
Al$_2$O$_3$	16.14	16.08	16.38	16.02	16.94	15.67	*0.11*
Fe$_2$O$_3$	1.03	1.02	1.00	1.02	0.99	1.12	
FeO	6.08	6.09	6.10	6.09	6.11	6.00	*0.04*
MnO	0.07	0.08	0.11	0.10	0.08	0.09	*0.01*
MgO	9.57	8.83	9.16	8.87	9.02	9.02	*0.07*
CaO	9.87	9.48	9.70	9.61	9.89	7.24	*0.07*
Na$_2$O	2.90	2.95	2.82	2.94	2.91	3.15	*0.25*
K$_2$O	0.70	0.78	0.75	0.78	0.77	1.45	*0.02*
P$_2$O$_5$	0.15	0.15	0.16	0.16	0.15	0.15	*0.01*
S	0.09	0.09	0.08	0.09	0.09	0.06	*0.003*
Cl	0.040	0.037	0.038	0.038	0.039	0.032	*0.002*
H$_2$O	2.87	2.85	3.04	3.13	2.11	1.84	*0.16*
CO$_2$ (ppm) RESTORED	2924	1782	2300	3025	1534	0	*77*
T °C	1266	1251	1255	1251	1250	1284	
Fo	90.3	89.4	89.8	89.5	89.7	89.7	
% PEC	12.1	11.5	10.1	10.1	10.9	13.1	
ppm							
Li	9.04	7.04	9.05			35.27	*2.62*
B	3.56	3.30	5.27			13.09	*3.03*
Sc	24.70	24.93	26.13			20.54	*1.28*
V	242	189	196			134	*14*
Rb	14.32	15.52	15.01			27.66	*0.83*
Sr	344	351	344			316	*8*
Y	13.42	13.08	13.44			13.12	*0.84*
Zr	67.77	68.02	70.46			68.45	*4.49*
Nb	5.03	4.37	4.63			4.69	*0.41*
Ba	177	195	189			312	*5*
La	7.05	7.86	7.32			9.51	*0.29*
Ce	17.91	18.16	16.88			19.91	*0.54*
Pr	2.11	2.08	2.07			2.47	*0.10*
Nd	10.04	9.53	10.09			11.15	*0.33*
Sm	2.38	2.39	2.34			2.44	*0.20*
Eu	0.81	0.79	0.81			1.06	*0.08*
Gd	3.02	2.65	2.68			2.44	*0.19*
Dy	2.30	2.38	2.15			2.53	*0.13*
Er	1.64	1.19	1.38			1.36	*0.12*
Yb	1.48	1.46	1.32			1.73	*0.14*
Hf	1.80	1.84	1.84			1.72	*0.14*
Ta	0.28	0.27	0.26			0.34	*0.04*
Pb	2.88	3.02	2.80			8.29	*0.28*
Th	1.08	1.58	1.44			3.26	*0.14*
U	0.38	0.42	0.48			1.62	*0.06*

LCC	5-01(MI_1)	5-01(MI_2)	5-03	5-04	5-05	5-07	5-11(MI_1)	5-11(MI_3)	5-12	S.D.
wt%										
SiO_2	50.83	50.94	52.20	54.25	51.45	51.84	53.89	55.30	51.46	0.22
TiO_2	0.81	0.81	0.87	0.77	0.89	0.85	0.67	0.67	0.78	0.02
Al_2O_3	16.13	15.76	15.90	15.86	15.87	16.29	15.11	15.28	16.57	0.14
Fe_2O_3	1.05	1.06	1.10	1.13	1.10	1.04	1.23	1.02	1.06	
FeO	6.06	6.04	6.01	5.99	6.02	6.06	5.90	6.09	6.05	0.08
MnO	0.09	0.09	0.08	0.10	0.07	0.08	0.10	0.11	0.10	0.02
MgO	8.56	8.56	8.38	8.37	8.61	8.60	8.30	9.28	7.87	0.18
CaO	9.81	9.72	9.60	7.52	9.73	10.04	6.92	6.97	9.56	0.14
Na_2O	3.20	3.25	3.55	3.43	3.54	3.21	3.69	1.94	3.41	0.19
K_2O	0.85	0.82	0.91	1.46	0.82	0.85	1.77	1.72	1.03	0.02
P_2O_5	0.16	0.16	0.16	0.16	0.17	0.16	0.13	0.13	0.17	0.01
S	0.09	0.09	0.06	0.08	0.10	0.08	0.06	0.06	0.08	0.003
Cl	0.037	0.036	0.039	0.035	0.036	0.040	0.035	0.035	0.037	0.001
H_2O	2.53	2.90	1.28	1.00	1.79	1.03	2.39	1.56	2.01	0.28
CO_2 (ppm) RESTORED	2555	2677	1751	1052	908	2705	0	0	2055	106
T °C	1245	1247	1246	1269	1251	1242	1284	1277	1231	
Fo	89.3	89.3	89.2	89.1	89.5	89.3	89.3	89.3	88.5	
% PEC	8.8	9.6	6.8	12.1	11.4	9.9	11.7	13.8	8.3	
ppm										
Li			9.17	33.23			51.64		11.13	4.95
B			5.36	10.20			12.39		5.33	4.29
Sc			26.06	18.91			18.28		21.07	1.23
V			186	142			139		180	11
Rb			15.63	28.26			33.25		22.00	1.03
Sr			350	328			296		376	8
Y			13.71	14.07			12.81		12.51	0.83
Zr			76.08	76.37			67.65		70.25	4.45
Nb			4.75	5.21			4.64		4.67	0.42
Ba			208	332			323		243	7
La			8.41	10.56			9.30		8.75	0.27
Ce			18.32	21.67			20.47		19.14	0.56
Pr			2.35	2.52			2.33		2.49	0.09
Nd			9.91	11.45			10.19		10.35	0.40
Sm			2.19	2.41			2.19		2.74	0.20
Eu			0.76	0.77			0.65		0.78	0.06
Gd			2.26	2.55			2.63		2.26	0.17
Dy			2.17	2.49			2.02		2.31	0.13
Er			1.49	1.47			1.39		1.41	0.07
Yb			1.27	1.46			1.74		1.30	0.07
Hf			1.90	1.52			1.72		1.79	0.13
Ta			0.28	0.38			0.31		0.24	0.05
Pb			3.14	9.74			9.82		3.81	0.47
Th			1.60	2.69			2.84		1.46	0.17
U			0.54	1.51			1.63		0.45	0.10

	LCC-4-05	LCC-4-06(MI_1)	LCC-4-13	avg 1 s.d.
wt%				
SiO$_2$	52.66	52.08	50.73	*0.42*
TiO$_2$	0.93	0.94	0.92	*0.02*
Al$_2$O$_3$	16.64	17.25	16.28	*0.07*
Fe$_2$O$_3$	1.10	1.03	1.07	
FeO	6.02	6.10	6.05	*0.04*
MnO	0.10	0.08	0.07	*0.01*
MgO	8.56	7.57	8.65	*0.06*
CaO	8.33	9.60	9.54	*0.09*
Na$_2$O	3.25	3.45	3.38	*0.06*
K$_2$O	1.56	1.00	0.84	*0.01*
P$_2$O$_5$	0.19	0.18	0.18	*0.003*
S	0.02	0.06	0.10	*0.004*
Cl	0.042	0.039	0.046	*0.002*
H$_2$O	0.71	0.73	2.39	*0.28*
CO$_2$ (ppm) RESTORED	1711	3702	2655	*99*
T °C	1262	1219	1252	
Fo	89.4	88.0	89.5	
% PEC	15.6	9.5	10.5	
ppm				
Li	6.24	68.95		*5.96*
B	3.35	23.12		*4.57*
Sc	20.48	27.77		*1.45*
V	148	194		*13*
Rb	11.19	53.70		*1.08*
Sr	278	461		*8*
Y	9.84	19.25		*1.25*
Zr	54.70	105.92		*6.77*
Nb	3.95	7.92		*0.49*
Ba	160	515		*10*
La	6.47	14.92		*0.31*
Ce	15.21	33.70		*0.69*
Pr	1.85	3.65		*0.13*
Nd	7.87	15.52		*0.46*
Sm	1.87	3.05		*0.32*
Eu	0.65	1.03		*0.08*
Gd	1.85	3.98		*0.27*
Dy	1.92	3.82		*0.26*
Er	1.10	2.23		*0.12*
Yb	1.13	2.13		*0.14*
Hf	1.26	3.29		*0.21*
Ta	0.28	0.57		*0.05*
Pb	2.62	14.00		*0.57*
Th	1.24	4.78		*0.17*
U	0.32	2.89		*0.09*

	LCC-2-01	LCC-2-02	LCC-2-04	LCC-2-05	LCC-2-07	LCC-2-08	LCC-2-09	LCC-2-10	S.D.
wt%									
SiO$_2$	50.98	50.96	50.60	50.55	50.57	50.76	50.83	49.99	0.26
TiO$_2$	0.96	0.94	0.95	0.97	0.95	0.94	0.94	0.92	0.02
Al$_2$O$_3$	16.54	16.66	16.57	17.04	16.85	17.03	16.87	16.74	0.11
Fe$_2$O$_3$	1.07	1.00	1.03	1.04	1.06	1.03	1.05	1.05	
FeO	6.04	6.10	6.08	6.06	6.05	6.08	6.06	6.06	0.07
MnO	0.09	0.08	0.08	0.09	0.08	0.09	0.09	0.09	0.01
MgO	7.94	8.32	8.24	8.20	8.18	7.66	7.98	8.12	0.05
CaO	9.53	9.07	9.24	9.39	9.47	9.50	9.47	9.41	0.05
Na$_2$O	3.58	2.91	3.22	3.42	3.49	3.43	3.46	3.40	0.14
K$_2$O	0.89	0.95	0.90	0.92	0.91	0.91	0.91	0.89	0.01
P$_2$O$_5$	0.19	0.20	0.20	0.20	0.20	0.20	0.20	0.19	0.01
S	0.09	0.09	0.09	0.09	0.09	0.10	0.09	0.09	0.003
Cl	0.037	0.037	0.038	0.038	0.039	0.039	0.038	0.039	0.002
H$_2$O	2.27	2.93	2.99	2.19	2.27	2.46	2.22	3.25	0.18
CO$_2$ (ppm) RESTORED	1541	1902	2904	2096	2021	1852	1522	2288	62
T °C	1235	1240	1241	1240	1240	1224	1234	1240	
Fo	88.7	88.8	88.9	89.0	89.0	88.2	88.7	88.9	
% PEC	7.9	9.0	9.2	8.1	8.1	6.2	7.5	8.4	
ppm									
Li	10.53		7.71		9.59	8.50			1.43
B	6.57		4.77		6.69	6.08			2.70
Sc	26.02		24.16		27.18	27.57			1.37
V	256		191		195	200			13
Rb	24.05		16.82		17.06	17.67			0.78
Sr	392		379		377	388			8
Y	13.90		14.32		14.96	15.32			0.86
Zr	81.28		85.86		86.72	86.62			5.04
Nb	6.69		6.07		6.69	6.31			0.51
Ba	234		228		232	233			6
La	9.13		8.99		9.36	9.53			0.25
Ce	22.40		20.42		21.42	21.04			0.51
Pr	2.66		2.60		2.64	2.69			0.10
Nd	12.04		11.70		12.07	12.03			0.38
Sm	2.54		2.17		2.75	2.86			0.21
Eu	0.84		0.89		0.88	0.90			0.06
Gd	2.66		2.65		2.84	2.61			0.15
Dy	2.77		2.68		2.72	2.59			0.13
Er	1.46		1.73		1.52	1.65			0.13
Yb	1.04		1.70		1.52	1.14			0.16
Hf	1.94		1.72		1.84	2.14			0.15
Ta	0.34		0.33		0.35	0.35			0.04
Pb	3.91		2.95		2.97	3.48			0.19
Th	1.70		1.43		1.61	1.72			0.11
U	0.61		0.48		0.48	0.50			0.04

C.2. Analyzed (uncorrected) Melt Inclusion Compositions

LCC	9-01	9-02	9-06	9-07	9-09(1)	9-09(2)	9-04	9-04(2)	9-10	9-13	9-16(1)	9-16(2)	9-18(1)	1 S.D.
wt%														
SiO_2	51.04	49.89	50.48	50.57	51.04	51.44	50.89	51.28	51.15	53.14	49.96	50.10	51.18	*0.34*
Al_2O_3	17.42	18.12	17.82	16.72	17.20	17.73	17.72	17.61	17.95	17.70	17.27	17.45	17.39	*0.27*
FeO^T	5.34	5.39	4.99	5.18	4.94	5.05	5.30	5.25	5.18	6.21	5.46	5.31	5.21	*0.13*
MgO	5.71	7.15	5.72	8.59	5.80	5.88	5.77	5.58	5.67	4.87	6.03	6.05	5.94	*0.75*
CaO	10.57	9.49	11.48	10.17	10.73	10.46	10.76	10.51	10.79	8.92	11.20	11.32	10.77	*0.22*
Na_2O	3.39	3.46	3.11	2.78	3.19	3.06	3.34	3.22	3.23	3.72	3.12	3.09	3.24	*0.16*
K_2O	0.90	0.85	0.77	0.82	0.83	0.88	0.85	0.93	0.87	1.35	0.71	0.72	0.83	*0.03*
TiO_2	0.91	0.95	0.93	0.83	0.85	0.86	0.89	0.88	0.86	0.85	0.87	0.89	0.87	*0.03*
MnO	0.10	0.09	0.09	0.09	0.09	0.09	0.09	0.09	0.09	0.11	0.10	0.10	0.10	*0.01*
P_2O_5	0.17	0.18	0.18	0.16	0.16	0.16	0.17	0.16	0.17	0.16	0.17	0.16	0.16	*0.01*
S	0.09	0.09	0.10	0.09	0.09	0.06	0.10	0.09	0.10	0.08	0.10	0.10	0.09	*0.003*
Cl	0.04	0.04	0.04	0.03	0.04	0.04	0.04	0.04	0.04	0.04	0.04	0.04	0.04	*0.003*
CO_2 (ppm)	965	947	1402	1252	0	848	560	679	1227	648	1500	1545	1339	*91*
H_2O	2.70	3.07	3.59	3.11	3.00	3.71	3.16	3.51	2.92	2.43	3.66	3.71	3.17	*0.25*
ppm														
Li				6.28	9.78	17.32	7.87	8.35		26.82	5.26	8.21		*1.93*
B				7.74	5.49	7.19	2.50	5.54		10.25	4.17	5.78		*2.83*
Sc				32.07	30.89	34.44	29.46	29.19		25.71	31.79	31.23		*1.58*
V				211	209	195	190	209		177	209	227		*11.89*
Ni				68.29	274.75	175.40	62.74	232.51		47.50	84.43	57.81		*20.22*
Rb				10.97	17.20	15.39	14.93	14.64		28.57	10.23	12.78		*0.69*
Sr				373	375	405	379	373		380	349	360		*8.53*
Y				16.53	14.27	17.22	14.43	14.13		13.86	14.40	13.45		*0.81*
Zr				87.06	76.60	98.84	78.59	74.38		79.53	73.69	68.94		*4.59*
Nb				4.80	4.39	4.46	4.42	4.29		4.25	4.53	4.46		*0.35*
Ba				191	208	227	217	205		305	171	174		*5.96*
La				9.01	7.90	8.87	8.25	7.73		9.55	7.14	7.00		*0.28*
Ce				19.32	17.80	20.30	18.40	18.16		20.52	16.80	17.49		*0.68*
Pr				2.68	2.34	3.02	2.77	2.48		2.53	2.36	2.17		*0.14*
Nd				11.78	10.46	16.56	12.41	11.53		12.56	10.01	10.50		*0.57*
Sm				2.38	2.64	2.27	2.70	2.49		2.52	2.46	2.23		*0.24*
Eu				1.11	0.91	1.19	0.87	0.88		0.86	0.86	0.88		*0.08*
Gd				3.27	2.77	3.16	3.01	2.76		2.53	2.51	2.88		*0.17*
Dy				2.82	2.59	2.92	3.32	2.50		2.56	2.66	2.47		*0.17*
Er				1.79	1.39	2.71	1.33	1.52		1.55	1.75	1.65		*0.12*
Yb				1.53	1.61	1.92	1.69	1.39		1.43	1.42	1.61		*0.12*
Hf				1.91	1.94	3.80	2.09	1.71		1.98	1.85	1.26		*0.18*
Ta				0.30	0.25	0.48	0.20	0.26		0.26	0.29	0.29		*0.05*
Pb				2.58	2.94	3.15	3.15	3.08		7.18	1.80	2.31		*0.20*
Th				1.39	1.66	1.82	1.80	1.68		2.48	1.22	1.08		*0.12*
U				0.38	0.51	0.59	0.63	0.50		0.83	0.40	0.40		*0.05*

	LCC-7-02	LCC-7-03	LCC-7-04	LCC-7-05	LCC-7-08	LCC-7-10	1 S.D.
wt%							
SiO$_2$	51.17	51.51	51.47	52.01	51.34	51.48	*0.23*
Al$_2$O$_3$	18.05	17.38	17.68	17.13	17.43	17.39	*0.13*
FeO^T	4.77	4.96	4.80	5.80	4.89	4.82	*0.06*
MgO	5.54	6.37	6.07	6.28	6.30	6.18	*0.12*
CaO	11.78	11.21	11.86	10.40	11.06	11.29	*0.07*
Na$_2$O	2.91	3.23	3.23	2.87	3.21	3.15	*0.12*
K$_2$O	0.68	0.72	0.68	0.85	0.76	0.73	*0.02*
TiO$_2$	0.86	0.83	0.87	0.86	0.85	0.86	*0.02*
MnO	0.08	0.09	0.08	0.10	0.08	0.09	*0.01*
P$_2$O$_5$	0.14	0.15	0.15	0.14	0.15	0.16	*0.01*
S	0.10	0.10	0.08	0.09	0.09	0.07	*0.001*
Cl	0.04	0.04	0.04	0.04	0.04	0.04	*0.001*
CO$_2$ (ppm)	974	1159	1014	654	1043	1198	*75*
H$_2$O	2.54	2.14	1.88	3.54	3.42	3.36	*0.16*
ppm							
Li				18.50	7.64	7.96	*1.72*
B				4.81	6.85	3.82	*2.14*
Sc				31.37	31.66	28.41	*1.57*
V				207	221	239	*13*
Ni				78.33	107.05	105.84	*10.79*
Rb				15.28	14.41	14.33	*0.65*
Sr				349	363	362	*6*
Y				14.72	14.88	13.26	*0.85*
Zr				76.60	77.49	71.55	*4.23*
Nb				4.37	4.57	4.70	*0.34*
Ba				212	199	192	*5*
La				8.03	7.60	6.89	*0.23*
Ce				17.36	17.76	16.89	*0.47*
Pr				2.29	2.36	2.21	*0.08*
Nd				9.87	9.91	9.91	*0.39*
Sm				2.50	2.67	2.20	*0.13*
Eu				0.89	0.91	0.81	*0.06*
Gd				2.75	2.47	2.33	*0.22*
Dy				2.53	2.83	2.50	*0.09*
Er				1.47	1.59	1.30	*0.09*
Yb				1.71	1.48	1.31	*0.07*
Hf				1.83	1.80	1.79	*0.13*
Ta				0.20	0.27	0.29	*0.03*
Pb				4.29	3.03	2.63	*0.19*
Th				1.39	1.27	1.10	*0.09*
U				0.47	0.46	0.41	*0.03*

	LCC-6-01	LCC-6-02	LCC-6-06	LCC-6-07	LCC-6-08	LCC-6-10	*1 S.D.*
wt%							
SiO_2	50.72	52.26	50.43	51.18	49.98	55.27	*0.31*
Al_2O_3	17.98	17.96	17.84	17.51	18.30	17.70	*0.11*
FeO	4.96	4.81	5.47	5.23	4.69	5.62	*0.04*
MgO	5.70	5.27	5.73	5.58	5.56	4.31	*0.07*
CaO	11.00	10.58	10.56	10.50	10.68	8.17	*0.07*
Na_2O	3.23	3.29	3.07	3.21	3.14	3.56	*0.25*
K_2O	0.78	0.88	0.82	0.86	0.83	1.63	*0.02*
TiO_2	0.91	0.90	0.92	0.91	0.89	0.80	*0.02*
MnO	0.08	0.08	0.12	0.11	0.08	0.11	*0.01*
P_2O_5	0.16	0.17	0.17	0.17	0.16	0.17	*0.01*
S	0.10	0.10	0.09	0.09	0.10	0.07	*0.003*
Cl	0.04	0.04	0.04	0.04	0.04	0.04	*0.002*
CO_2 (ppm)	1147	633	970	1426	583	1290	*77*
H_2O	3.06	3.06	3.18	3.29	2.19	1.99	*0.16*
ppm							
Li	10.04	7.73	9.94			40.54	*2.62*
B	3.95	3.63	5.79			15.05	*3.03*
Sc	27.45	27.40	28.72			23.61	*1.28*
V	269	208	215			154	*14*
Ni	389.75	72.98	148.33			18.70	*32.28*
Rb	15.91	17.05	16.49			31.80	*0.83*
Sr	382	385	378			364	*8*
Y	14.91	14.37	14.77			15.09	*0.84*
Zr	75.30	74.75	77.43			78.67	*4.49*
Nb	5.59	4.80	5.08			5.40	*0.41*
Ba	197	214	207			359	*5*
La	7.84	8.64	8.05			10.93	*0.29*
Ce	19.91	19.95	18.55			22.89	*0.54*
Pr	2.35	2.29	2.28			2.84	*0.10*
Nd	11.15	10.47	11.08			12.82	*0.33*
Sm	2.64	2.63	2.57			2.80	*0.20*
Eu	0.90	0.87	0.89			1.22	*0.08*
Gd	3.36	2.92	2.95			2.80	*0.19*
Dy	2.55	2.61	2.36			2.91	*0.13*
Er	1.82	1.30	1.51			1.57	*0.12*
Yb	1.64	1.60	1.45			1.98	*0.14*
Hf	2.00	2.03	2.02			1.98	*0.14*
Ta	0.31	0.29	0.29			0.39	*0.04*
Pb	3.19	3.32	3.08			9.53	*0.28*
Th	1.20	1.74	1.58			3.75	*0.14*
U	0.42	0.47	0.53			1.86	*0.06*

	5-01(MI_1)	5-01(MI_2)	5-03	5-04	5-05	5-07	5-11(MI_1)	5-11(MI_3)	5-12	5-13	1 S.D.
wt%										reentrant	
SiO_2	50.35	50.64	52.53	56.06	52.25	51.00	54.70	55.71	51.28	55.66	0.22
Al_2O_3	17.08	16.84	16.83	17.83	17.54	17.24	16.66	16.90	17.57	17.23	0.14
FeO^T	5.41	5.03	4.79	5.95	4.53	5.01	5.78	6.00	5.93	5.81	0.08
MgO	5.55	5.43	6.68	3.87	5.15	5.27	3.92	3.94	4.78	3.69	0.18
CaO	10.39	10.39	10.16	8.46	10.75	10.63	7.63	7.71	10.13	7.91	0.14
Na_2O	3.39	3.47	3.76	3.86	3.91	3.40	4.07	2.15	3.62	4.02	0.19
K_2O	0.90	0.88	0.97	1.64	0.91	0.90	1.95	1.90	1.09	1.87	0.02
TiO_2	0.86	0.86	0.92	0.86	0.98	0.90	0.74	0.74	0.83	0.74	0.02
MnO	0.10	0.10	0.09	0.11	0.08	0.08	0.11	0.12	0.11	0.11	0.02
P_2O_5	0.17	0.17	0.17	0.18	0.19	0.17	0.14	0.14	0.18	0.16	0.01
S	0.09	0.09	0.06	0.08	0.10	0.08	0.06	0.06	0.08	0.06	0.003
Cl	0.04	0.04	0.04	0.04	0.04	0.04	0.04	0.04	0.04	0.04	0.001
CO_2 (ppm)	1259	1283	786	198	1093	1300	1484	317	813	141	106
H_2O	2.58	2.98	1.31	1.08	1.90	1.04	2.53	1.65	2.05	1.13	0.28
ppm											
Li			10.54	37.77			60.05		12.10	43.23	4.95
B			6.16	11.59			14.41		5.79	14.93	4.29
Sc			29.96	21.49			21.26		22.90	18.54	1.23
V			214	161			161		196	151	11
Ni			280.29	27.14			663.83		215.13	29.76	74.65
Rb			17.96	32.12			38.67		23.92	40.48	1.03
Sr			403	373			344		409	346	8
Y			15.76	15.99			14.90		13.60	14.72	0.83
Zr			87.45	86.78			78.67		76.36	81.45	4.45
Nb			5.46	5.92			5.39		5.08	5.80	0.42
Ba			239	377			375		264	386	7
La			9.67	12.00			10.81		9.51	11.15	0.27
Ce			21.06	24.62			23.80		20.81	23.18	0.56
Pr			2.70	2.87			2.71		2.70	2.83	0.09
Nd			11.39	13.01			11.85		11.25	12.18	0.40
Sm			2.52	2.74			2.55		2.98	2.43	0.20
Eu			0.87	0.88			0.76		0.85	0.80	0.06
Gd			2.60	2.90			3.05		2.46	2.72	0.17
Dy			2.50	2.83			2.35		2.51	2.69	0.13
Er			1.71	1.68			1.61		1.53	1.60	0.07
Yb			1.46	1.66			2.02		1.41	1.73	0.07
Hf			2.18	1.73			2.01		1.95	1.98	0.13
Ta			0.33	0.43			0.36		0.26	0.48	0.05
Pb			3.61	11.07			11.42		4.14	11.59	0.47
Th			1.84	3.05			3.30		1.59	3.71	0.17
U			0.62	1.72			1.89		0.49	2.19	0.10

	LCC-4-01	LCC-4-05	LCC-4-06(MI_1)	LCC-4-06(MI_2)	LCC-4-08	1 S.D.
wt%	reentrant				reentrant	
SiO_2	52.29	54.49	51.08	55.38	56.67	*0.42*
Al_2O_3	18.46	19.23	18.14	17.38	18.22	*0.07*
FeO^T	4.34	5.63	4.79	5.80	5.93	*0.04*
MgO	3.39	2.75	4.48	3.68	2.86	*0.06*
CaO	10.67	9.62	10.10	7.77	7.87	*0.09*
Na_2O	4.01	3.76	3.63	4.21	4.15	*0.06*
K_2O	0.91	1.80	1.05	1.94	1.97	*0.01*
TiO_2	1.00	1.07	0.99	0.77	0.81	*0.02*
MnO	0.08	0.11	0.09	0.11	0.12	*0.01*
P_2O_5	0.21	0.22	0.19	0.18	0.18	*0.003*
S	0.10	0.02	0.06	0.04	0.10	*0.004*
Cl	0.05	0.05	0.04	0.04	0.04	*0.002*
CO_2 (ppm)	671	251	-105	1323	1046	*99*
H_2O	1.94	0.79	0.74	2.20	2.31	*0.28*
ppm						
Li	63.09	7.52	74.95	11.31		*5.96*
B	10.38	4.04	25.13	5.43		*4.57*
Sc	34.09	24.68	30.18	27.77		*1.45*
V	240	179	211	236		*13*
Ni	566.96	274.08	2643.00	76.74		*138.44*
Rb	30.31	13.48	58.37	30.21		*1.08*
Sr	454	335	501	319		*8*
Y	19.69	11.86	20.92	15.59		*1.25*
Zr	109.97	65.91	115.13	73.27		*6.77*
Nb	7.60	4.76	8.61	4.37		*0.49*
Ba	394	193	560	578		*10*
La	12.98	7.80	16.22	9.94		*0.31*
Ce	29.61	18.33	36.63	24.33		*0.69*
Pr	3.80	2.23	3.97	3.30		*0.13*
Nd	16.47	9.48	16.87	14.83		*0.46*
Sm	4.25	2.25	3.32	3.18		*0.32*
Eu	1.31	0.79	1.12	0.90		*0.08*
Gd	3.58	2.23	4.33	3.60		*0.27*
Dy	3.24	2.31	4.16	3.23		*0.26*
Er	2.24	1.33	2.43	1.65		*0.12*
Yb	2.34	1.36	2.31	1.31		*0.14*
Hf	2.53	1.52	3.57	1.67		*0.21*
Ta	0.42	0.33	0.62	0.30		*0.05*
Pb	16.08	3.16	15.22	4.61		*0.57*
Th	2.50	1.49	5.20	1.68		*0.17*
U	0.93	0.38	3.14	0.55		*0.09*

	LCC-2-01	LCC-2-02	LCC-2-04	LCC-2-05	LCC-2-07	LCC-2-08	LCC-2-09	LCC-2-10	1 S.D.
wt%									
SiO_2	51.36	51.75	51.52	50.85	50.76	50.62	51.20	50.69	*0.26*
Al_2O_3	17.69	18.10	18.09	18.24	17.99	17.81	17.99	18.11	*0.11*
FeO^T	4.93	5.12	5.07	5.16	5.35	5.68	5.22	5.22	*0.07*
MgO	5.68	5.59	5.46	5.71	5.56	5.64	5.75	5.57	*0.05*
CaO	10.20	9.85	10.09	10.05	10.12	9.93	10.10	10.18	*0.05*
Na_2O	3.83	3.16	3.52	3.66	3.73	3.58	3.69	3.68	*0.14*
K_2O	0.95	1.03	0.98	0.98	0.97	0.95	0.97	0.96	*0.01*
TiO_2	1.02	1.02	1.03	1.04	1.02	0.98	1.01	0.99	*0.02*
MnO	0.10	0.09	0.09	0.09	0.09	0.09	0.09	0.09	*0.01*
P_2O_5	0.20	0.21	0.22	0.22	0.21	0.21	0.21	0.21	*0.01*
S	0.09	0.10	0.10	0.10	0.10	0.10	0.10	0.10	*0.003*
Cl	0.04	0.04	0.04	0.04	0.04	0.04	0.04	0.04	*0.002*
CO_2 (ppm)	819	895	1467	1099	993	1111	812	1168	*62*
H_2O	2.34	3.08	3.16	2.26	2.35	2.49	2.29	3.40	*0.18*
ppm									
Li	11.20		8.38		10.31	9.14			*1.43*
B	6.99		5.19		7.20	6.54			*2.70*
Sc	27.68		26.26		29.22	29.65			*1.37*
V	272		208		210	215			*13*
Ni	201.94		102.16		1352.67	86.05			*36.10*
Rb	25.59		18.28		18.34	19.00			*0.78*
Sr	417		412		406	418			*8*
Y	14.79		15.57		16.08	16.48			*0.86*
Zr	86.47		93.33		93.24	93.14			*5.04*
Nb	7.12		6.60		7.19	6.78			*0.51*
Ba	249		247		250	250			*6*
La	9.72		9.77		10.06	10.24			*0.25*
Ce	23.82		22.19		23.03	22.62			*0.51*
Pr	2.83		2.83		2.84	2.90			*0.10*
Nd	12.81		12.72		12.97	12.93			*0.38*
Sm	2.70		2.36		2.96	3.08			*0.21*
Eu	0.89		0.97		0.95	0.97			*0.06*
Gd	2.83		2.88		3.06	2.80			*0.15*
Dy	2.94		2.92		2.92	2.78			*0.13*
Er	1.55		1.88		1.64	1.78			*0.13*
Yb	1.10		1.85		1.63	1.22			*0.16*
Hf	2.07		1.87		1.98	2.30			*0.15*
Ta	0.36		0.36		0.38	0.38			*0.04*
Pb	4.16		3.20		3.19	3.74			*0.19*
Th	1.81		1.55		1.73	1.85			*0.11*
U	0.65		0.52		0.52	0.54			*0.04*

REFERENCES CITED

Chapter I

Anderson, A. T. (1974). Evidence for a picritic, volatile-rich magma beneath Mt. Shasta, California. *Journal of Petrology*, *15*(2), 243-267.

Cai, Y., LaGatta, A., Goldstein, S. L., Langmuir, C. H., Gómez-Tuena, A., Martín-del Pozzo, A. L., & Carrasco-Núñez, G. (2014). Hafnium isotope evidence for slab melt contributions in the Central Mexican Volcanic Belt and implications for slab melting in hot and cold slab arcs. *Chemical Geology*, 377, 45-55.

Grove, T., Parman, S., Bowring, S., Price, R., & Baker, M. (2002). The role of an H_2O-rich fluid component in the generation of primitive basaltic andesites and andesites from the Mt. Shasta region, N. California. *Contributions to Mineralogy and Petrology*, 142(4), 375-396.

Hacker, B. R. (2008). H_2O subduction beyond arcs. *Geochemistry, Geophysics, Geosystems*, 9(3).

Holloway, J. R., & Blank, J. G. (1994). Application of experimental results to COH species in natural melts. *Reviews in Mineralogy and Geochemistry*, *30*(1), 187-230.

Johnson, E. R., Wallace, P. J., Cashman, K. V., Granados, H. D., & Kent, A. J. (2008). Magmatic volatile contents and degassing-induced crystallization at Volcán Jorullo, Mexico: implications for melt evolution and the plumbing systems of monogenetic volcanoes. *Earth and Planetary Science Letters*, 269(3), 478-487.

Jung, H., & Karato, S. I. (2001). Water-induced fabric transitions in olivine.*Science*, *293*(5534), 1460-1463.

Kessel, R., Schmidt, M. W., Ulmer, P., & Pettke, T. (2005). Trace element signature of subduction-zone fluids, melts and supercritical liquids at 120–180 km depth. *Nature,* 437(7059), 724-727.

Kirby, S., Wang, K., & Dunlop, S. (Eds.). (2002). The Cascadia Subduction Zone and Related Subduction Systems: Seismic Structure, Intraslab Earthquakes and Processes, and Earthquake Hazards (pp. 79-80). US Geological Survey.

Leeman, W. P., Smith, D. R., Hildreth, W., Palacz, Z., & Rogers, N. (1990). Compositional diversity of late Cenozoic basalts in a transect across the southern Washington Cascades: implications for subduction zone magmatism.*Journal of Geophysical Research: Solid Earth (1978–2012)*, *95*(B12), 19561-19582.

Métrich, N., & Wallace, P. J. (2008). Volatile abundances in basaltic magmas and their degassing paths tracked by melt inclusions. *Reviews in Mineralogy and Geochemistry*, *69*(1), 363-402.

Pioli, L., Erlund, E., Johnson, E., Cashman, K., Wallace, P., Rosi, M., & Granados, H. D. (2008). Explosive dynamics of violent Strombolian eruptions: the eruption of Parícutin Volcano 1943–1952 (Mexico). *Earth and Planetary Science Letters*, *271*(1), 359-368.

Plank, T., & Langmuir, C. H. (1993). Tracing trace elements from sediment input to volcanic output at subduction zones. *Nature*, *362*(6422), 739-743.

Ringwood, A. E. (1974). The petrological evolution of island arc systems Twenty-seventh William Smith Lecture. *Journal of the Geological Society*,*130*(3), 183-204.

Roggensack, K., Hervig, R. L., McKnight, S. B., & Williams, S. N. (1997). Explosive basaltic volcanism from Cerro Negro volcano: influence of volatiles on eruptive style. *Science*, *277*(5332), 1639-1642.

Ruscitto, D. M., Wallace, P. J., Johnson, E. R., Kent, A. J. R., & Bindeman, I. N. (2010). Volatile contents of mafic magmas from cinder cones in the Central Oregon High Cascades: Implications for magma formation and mantle conditions in a hot arc. *Earth and Planetary Science Letters*, 298(1), 153-161.

Schmidt, M. W., & Poli, S. (1998). Experimentally based water budgets for dehydrating slabs and consequences for arc magma generation. *Earth and Planetary Science Letters*, 163(1), 361-379.

Schiano, P. (2003). Primitive mantle magmas recorded as silicate melt inclusions in igneous minerals. *Earth-Science Reviews*, *63*(1), 121-144.

Sheppard, P. R., Ort, M. H., Anderson, K. C., Clynne, M. A., & May, E. M. (2009). Multiple dendrochronological responses to the eruption of Cinder Cone, Lassen volcanic National Park, California. *Dendrochronologia*, *27*(3), 213-221.

Syracuse, E. M., van Keken, P. E., & Abers, G. A. (2010). The global range of subduction zone thermal models. *Physics of the Earth and Planetary Interiors*,183(1), 73-90.

van Keken, P. E., Hacker, B. R., Syracuse, E. M., & Abers, G. A. (2011). Subduction factory: 4. Depth-dependent flux of H_2O from subducting slabs worldwide. *Journal of Geophysical Research: Solid Earth* (1978–2012), 116(B1).

Wilson, D. S. (2002). The Juan de Fuca plate and slab: Isochron structure and Cenozoic plate motions. US Geological Survey.

Chapter II

1. Kirby, S. H., Engdahl, E. R., & Villaseñor, A. Warm-slab subduction as a global process. The Cascadia Subduction Zone and related subduction systems–Seismic structure, intraslab earthquakes and processes, and earthquake hazards, *USGS Open-File Report,* **328**, 79-80 (2002).

2. Wada, I., & Wang, K.. Common depth of slab-mantle decoupling: Reconciling diversity and uniformity of subduction zones. Geochemistry Geophysics Geosystems, **10**, 1-36 (2009).

3. Wilson, D.S., The Juan de Fuca plate and slab — isochron structure and Cenozoic plate motions. *U.S. Geological Survey Open-File Report,* **328**, 9–12 (2002).

4. Rondenay, S., Abers, G. A., & Van Keken, P. E.. Seismic imaging of subduction zone metamorphism. Geology, **36**, 275-278 (2008).

5. Abers, G. A., et al. Imaging the source region of Cascadia tremor and intermediate-depth earthquakes. *Geology*, **37**, 1119-1122 (2009).

6. Van Keken, P. E., Hacker, B. R., Syracuse, E. M., & Abers, G. A.. Subduction factory: 4. Depth-dependent flux of H_2O from subducting slabs worldwide. Journal of Geophysical Research, **116**, B01401 (2011).

7. Ruscitto, D. M., Wallace, P. J., Johnson, E. R., Kent, A. J. R., & Bindeman, I. N. Volatile contents of mafic magmas from cinder cones in the Central Oregon High Cascades: Implications for magma formation and mantle conditions in a hot arc. *Earth and Planetary Science Letters*, **298**, 153–161 (2010).

8. Ruscitto, D. M., Wallace, P. J., & Kent, A. J. R.. Revisiting the compositions and volatile contents of olivine-hosted melt inclusions from the Mount Shasta region: implications for the formation of high-Mg andesites. *Contributions to Mineralogy and Petrology*, **162**, 109-132 (2011).

9. Le Voyer, M., Rose-Koga, E. F., Shimizu, N., Grove, T. L., & Schiano, P. Two contrasting H_2O-rich components in primary melt inclusions from Mount Shasta. *Journal of Petrology*, **51**, 1571-1595 (2010).

10. Plank, T., Kelley, K. A., Zimmer, M. M., Hauri, E. H., & Wallace, P. J. Why do mafic arc magmas contain ~4 wt % water on average? *Earth and Planetary Science Letters*, **364**, 168–179 (2013).

11. Shaw, A. M., Hauri, E. H., Fischer, T. P., Hilton, D. R., & Kelley, K. A. Hydrogen isotopes in Mariana arc melt inclusions: Implications for subduction dehydration and the deep-Earth water cycle. *Earth and Planetary Science Letters*, **275**, 138–145 (2008).

12. Leeman, W. P., Tonarini, S., Chan, L. H., & Borg, L. E. Boron and lithium isotopic variations in a hot subduction zone—the southern Washington Cascades. *Chemical Geology*, **212**, 101–124 (2004).

13. Borg, L. E., Clynne, M. A., & Bullen, T. D. The variable role of slab-derived fluids in the generation of a suite of primitive lavas from the Southernmost Cascades. *The Canadian Mineralogist*, **35**, 425-452 (1997).

14. Borg, L. E., Blichert-Toft, J., Clynne, M. A. Ancient and modern subduction zone contributions to the mantle sources of lavas from the Lassen Region of California inferred from Lu − Hf isotopic systematics. *Journal of Petrology*, **43**, 705–723 (2002).

15. Grove, T., Parman, S., Bowring, S., Price, R., & Baker, M. The role of an H_2O-rich fluid component in the generation of primitive basaltic andesites and andesites from the Mt. Shasta region, N. California. *Contributions to Mineralogy and Petrology*, **142**, 375–396 (2002).

16. McDonough, W. F. and Sun, S. S. The composition of the Earth. *Chemical Geology*, **120**, 223-253 (1995).

17. Cooper, L. B., et al., Global variations in H_2O/Ce: 1. Slab surface temperatures beneath volcanic arcs. *Geochemistry Geophysics Geosystems*, **13**, 1-27 (2012).

18. McCrory, P. A., Blair, J. L., Waldhauser, F., & Oppenheimer, D. H. Juan de Fuca slab geometry and its relation to Wadati- Benioff zone seismicity. *Journal of Geophysical Research: Solid Earth*, **117**, 1-16 (2012).

19. Cozzens, B. D., & Spinelli, G. A. A wider seismogenic zone at Cascadia due to fluid circulation in subducting oceanic crust. *Geology*, **40**, 899-902 (2012).

20. Wilson, C. R., Spiegelman, M., van Keken, P. E., & Hacker, B. R. Fluid flow in subduction zones: The role of solid rheology and compaction pressure. *Earth and Planetary Science Letters*, **401**, 261-274, (2014).

21. Schmidt, M. W., & Poli, S. Experimentally based water budgets for dehydrating slabs and consequences for arc magma generation. *Earth and Planetary Science Letters*, **163**, 361–379 (1998).

22. Hermann, J. & Spandler, C. J. Sediment melts at sub-arc depths: An experimental study. *Journal of Petrology*, **49**, 717-740 (2008).

23. Gaetani, G. A., O'Leary, J. A., Shimizu, N., Bucholz, C. E., & Newville, M. Rapid reequilibration of H_2O and oxygen fugacity in olivine-hosted melt inclusions. *Geology*, **40**, 915-918 (2012).

24. Bucholz, C. E., Gaetani, G. A., Behn, M. D., & Shimizu, N.. Post-entrapment modification of volatiles and oxygen fugacity in olivine-hosted melt inclusions. *Earth and Planetary Science Letters*, **374**, 145–155 (2013).

25. Newman, S., Epstein, S., & Stolper, E. Water, carbon dioxide, and hydrogen isotopes in glasses from the ca. 1340 AD eruption of the Mono Craters, California: constraints on degassing phenomena and initial volatile content. *Journal of Volcanology and Geothermal Research*, **35**, 75-96 (1988).

26. Poreda, R., Schilling, J. G., & Craig, H. Helium and hydrogen isotopes in ocean-ridge basalts north and south of Iceland. *Earth and Planetary Science Letters*, **78**, 1-17 (1986).

27. Taran, Y. A., Pokrovsky B. G., & Volynets, O. N.. Hydrogen isotopes in hornblendes and biotites from Quaternary volcanic rocks of the Kamchatka-Kurile arc. *Geochemical Journal – Japan*, **31**, 203-222 (1997).

28. Giggenbach, W. F. Isotopic shifts in waters from geothermal and volcanic systems along convergent plate boundaries and their origin. *Earth and Planetary Science Letters*, **113**, 495-510 (1992).

29. Wada, I., Behn, M. D., & Shaw, A. M. Effects of heterogeneous hydration in the incoming plate, slab rehydration, and mantle wedge hydration on slab-derived H_2O flux in subduction zones. *Earth and Planetary Science Letters*, **353**, 60-71 (2012).

30. Connolly, J. A. D. The geodynamic equation of state: what and how. *Geochemistry, Geophysics, Geosystems*, **10**, 1-19 (2009).

31. Wannamaker, P. E. et al. Segmentation of plate coupling, fate of subduction fluids, and modes of arc magmatism in Cascadia, inferred from magnetotelluric resistivity. *Geochemistry, Geophysics, Geosystems*, **15**, 4230-4253 (2014).

32. Liu, K., Levander, A., Zhai, Y., Porritt, R. W., & Allen, R. M. Asthenospheric flow and lithospheric evolution near the Mendocino Triple Junction. *Earth and Planetary Science Letters*, **323**, 60-71 (2012).

33. Alt, J. C., et al. Recycling of water, carbon, and sulfur during subduction of serpentinites: A stable isotope study of Cerro del Almirez, Spain. *Earth and Planetary Science Letters*, **327**, 50-60 (2012).

34. Plank, T. Constraints from thorium/lanthanum on sediment recycling at subduction zones and the evolution of the continents. *Journal of Petrology,* **46**, 921–944 (2005).

35. Davis, A. S., Clague, D. A., Cousens, B. L., Keaten, R., & Paduan, J. B. Geochemistry of basalt from the North Gorda segment of the Gorda Ridge: Evolution toward ultraslow spreading ridge lavas due to decreasing magma supply. *Geochemistry, Geophysics, Geosystems*, **9**, 1-24 (2008).

36. Jicha, B. R. et al. Isotopic and trace element constraints on the petrogenesis of lavas from the Mount Adams volcanic field, Washington. *Contributions to Mineralogy and Petrology*, **157**, 189-207 (2009).

37. Mullen, E. K., & Weis, D. Evidence for trench-parallel mantle flow in the northern Cascade Arc from basalt geochemistry. *Earth and Planetary Science Letters*, **414**, 100-107 (2015).

38. Skora, S., & Blundy, J. High-pressure hydrous phase relations of radiolarian clay and implications for the involvement of subducted sediment in arc magmatism. *Journal of Petrology*, **51**, 2211-2243 (2010).

39. Till, C. B., Grove, T. L., & Withers, A. C. The beginnings of hydrous mantle wedge melting. *Contributions to Mineralogy and Petrology*, **163**, 669-688 (2012).

40. Spandler, C., & Pirard, C. Element recycling from subducting slabs to arc crust: a review. *Lithos*, **170**, 208-223 (2013).

41. Defant, M.J., Drummond, M.S. Derivation of some modern arc magmas by melting of young subducted lithosphere. *Nature*, **347**, 662–665 (1990).

42. Klimm, K., Blundy, J. D., & Green, T. H. Trace element partitioning and accessory phase saturation during H_2O-saturated melting of basalt with implications for subduction zone chemical fluxes. *Journal of Petrology*, **49**, 523-553 (2008).

43. Jégo, S., & Dasgupta, R. Fluid-present melting of sulfide-bearing ocean-crust: Experimental constraints on the transport of sulfur from subducting slab to mantle wedge. *Geochimica et Cosmochimica Acta*, **110**, 106-134 (2013).

44. Hauri, E. H. et al. Matrix effects in hydrogen isotope analysis of silicate glasses by SIMS. *Chemical Geology*, **235**, 352-365 (2006).

45. Loewen, M. W., & Kent, A. J. Sources of elemental fractionation and uncertainty during the analysis of semi-volatile metals in silicate glasses using LA-ICP-MS. *Journal of Analytical Atomic Spectrometry*, **27**, 1502-1508 (2012).

46. Workman, R. K., & Hart, S. R. Major and trace element composition of the depleted MORB mantle (DMM). *Earth and Planetary Science Letters*, **231**, 53-72 (2005).

47. Donnelly, K. E., Goldstein, S. L., Langmuir, C. H., & Spiegelman, M. Origin of enriched ocean ridge basalts and implications for mantle dynamics. *Earth and Planetary Science Letters*, **226**, 347-366 (2004).

48. Shaw, A. M. Long-term preservation of slab signatures in the mantle inferred from hydrogen isotopes. *Nature Geoscience*, **5**, 224-228 (2012).

49. Hauri, E. H. SIMS analysis of volatiles in silicate glasses, 2: isotopes and abundances in Hawaiian melt inclusions. *Chemical Geology*, **183**, 115-141 (2002).

Chapter III

Bach, W., Peucker-Ehrenbrink, B., Hart, S. R., & Blusztajn, J. S. (2003). Geochemistry of hydrothermally altered oceanic crust: DSDP/ODP Hole 504B–Implications for seawater-crust exchange budgets and Sr-and Pb-isotopic evolution of the mantle. *Geochemistry, Geophysics, Geosystems,* 4(3).

Bacon, C. R., Bruggman, P. E., Christiansen, R. L., Clynne, M. A., Donnelly-Nolan, J. M., & Hildreth, W. (1997). Primitive magmas at five Cascades volcanic fields: melts from hot, heterogeneous sub-arc mantle. *Canadian Mineralogist*, 35, 397-424.

Baker, M. B., & Stolper, E. M. (1994). Determining the composition of high-pressure mantle melts using diamond aggregates. *Geochimica et Cosmochimica Acta*, 58(13), 2811-2827.

Baker, M. B., Grove, T. L., & Price, R. (1994). Primitive basalts and andesites from the Mt. Shasta region, N. California: products of varying melt fraction and water content. *Contributions to Mineralogy and Petrology*, 118(2), 111-129.

Bebout, G. E., Ryan, J. G., & Leeman, W. P. (1993). B-Be systematics in subduction-related metamorphic rocks: Characterization of the subducted component. *Geochimica et Cosmochimica Acta*, 57(10), 2227-2237.

Berge, P. A., & Stauber, D. A. (1987). Seismic refraction study of upper crustal structure in the Lassen Peak Area, northern California. *Journal of Geophysical Research: Solid Earth* (1978–2012), 92(B10), 10571-10579.

Boschi, C., Dini, A., Früh-Green, G. L., & Kelley, D. S. (2008). Isotopic and element exchange during serpentinization and metasomatism at the Atlantis Massif (MAR 30 N): insights from B and Sr isotope data. *Geochimica et Cosmochimica Acta*, 72(7), 1801-1823.

Borg, L. E. (1995). The origin and evolution of magmas from the Lassen Region of the southernmost Cascades. University of Texas at Austin.

Borg, L. E., Clynne, M. A., & Bullen, T. D. (1997). The variable role of slab-derived fluids in the generation of a suite of primitive calc-alkaline lavas from the southernmost Cascades, Calilornia. *Canadian Mineralogist*, 35, 425-452.

Borg, L. E., Brandon, A. D., Clynne, M. A., & Walker, R. J. (2000). Re–Os isotopic systematics of primitive lavas from the Lassen region of the Cascade arc, California. *Earth and Planetary Science Letters*, 177(3), 301-317.

Borg, L. E., Blichert-Toft, J., & Clynne, M. A. (2002). Ancient and modern subduction zone contributions to the mantle sources of lavas from the Lassen region of California inferred from Lu–Hf isotopic systematics. *Journal of Petrology*, 43(4), 705-723.

Bucholz, C. E., Gaetani, G. A., Behn, M. D., & Shimizu, N. (2013). Post-entrapment modification of volatiles and oxygen fugacity in olivine-hosted melt inclusions. *Earth and Planetary Science Letters*, 374, 145-155.

Cagnioncle, A. M., Parmentier, E. M., & Elkins-Tanton, L. T. (2007). Effect of solid flow above a subducting slab on water distribution and melting at convergent plate boundaries. *Journal of Geophysical Research: Solid Earth* (1978–2012), 112(B9).

Cai, Y., LaGatta, A., Goldstein, S. L., Langmuir, C. H., Gómez-Tuena, A., Martín-del Pozzo, A. L., & Carrasco-Núñez, G. (2014). Hafnium isotope evidence for slab melt contributions in the Central Mexican Volcanic Belt and implications for slab melting in hot and cold slab arcs. *Chemical Geology*, 377, 45-55.

Carpentier, M., Weis, D., & Chauvel, C. (2013). Large U loss during weathering of upper continental crust: the sedimentary record. *Chemical Geology*, 340, 91-104.

Carpentier, M., Weis, D., & Chauvel, C. (2014). Fractionation of Sr and Hf isotopes by mineral sorting in Cascadia Basin terrigenous sediments. *Chemical Geology*, 382, 67-82.

Cecil, M. R., Rotberg, G. L., Ducea, M. N., Saleeby, J. B., & Gehrels, G. E. (2012). Magmatic growth and batholithic root development in the northern Sierra Nevada, California. *Geosphere,* 8(3), 592-606.

Chaussidon, M., & Jambon, A. (1994). Boron content and isotopic composition of oceanic basalts: geochemical and cosmochemical implications. *Earth and Planetary Science Letters*, 121(3), 277-291.

Clynne, M. A. (1993). Geologic studies of the Lassen volcanic center, Cascade Range, California. University of California, Santa Cruz.

Clynne, M. A., & Muffler, L. J. P. (2010). Geologic map of Lassen Volcanic National Park and vicinity, California. US Department of the Interior, US Geological Survey.

Clynne, M. A., & Borg, L. E. (1997). Olivine and chromian spinel in primitive calc-alkaline and tholeiitic lavas from the southernmost Cascade Range, California: a reflection of relative fertility of the source. *Canadian Mineralogist*, 35, 453-472.

Cooper, L. B., Ruscitto, D. M., Plank, T., Wallace, P. J., Syracuse, E. M., & Manning, C. E. (2012). Global variations in H_2O/Ce: 1. Slab surface temperatures beneath volcanic arcs. *Geochemistry, Geophysics, Geosystems*, 13(3).

Danyushevsky, L. V., & Plechov, P. (2011). Petrolog3: Integrated software for modeling crystallization processes. *Geochemistry, Geophysics, Geosystems*, 12(7).

Davis, A. S., Clague, D. A., Cousens, B. L., Keaten, R., & Paduan, J. B. (2008). Geochemistry of basalt from the North Gorda segment of the Gorda Ridge: Evolution toward ultraslow spreading ridge lavas due to decreasing magma supply. *Geochemistry, Geophysics, Geosystems*, 9(4).

Defant, M. J., & Drummond, M. S. (1990). Derivation of some modern arc magmas by melting of young subducted lithosphere. *Nature*, 347(6294), 662-665.

Eiler, J. M. (2001). Oxygen isotope variations of basaltic lavas and upper mantle rocks. *Reviews in Mineralogy and Geochemistry*, 43(1), 319-364.

Eiler, J. M., Carr, M. J., Reagan, M., & Stolper, E. (2005). Oxygen isotope constraints on the sources of Central American arc lavas. *Geochemistry, Geophysics, Geosystems*, 6(7).

Gaetani, G. A., O'Leary, J. A., Shimizu, N., Bucholz, C. E., & Newville, M. (2012). Rapid reequilibration of H_2O and oxygen fugacity in olivine-hosted melt inclusions. *Geology*, 40(10), 915-918.

Garth, T., & Rietbrock, A. (2014). Order of magnitude increase in subducted H_2O due to hydrated normal faults within the Wadati-Benioff zone. Geology, 42(3), 207-210.

Ghiorso, M. S., Hirschmann, M. M., Reiners, P. W., & Kress, V. C. (2002). The pMELTS: A revision of MELTS for improved calculation of phase relations and major element partitioning related to partial melting of the mantle to 3 GPa. *Geochemistry, Geophysics, Geosystems*, 3(5), 1-35.

Grove, T., Parman, S., Bowring, S., Price, R., & Baker, M. (2002). The role of an H_2O-rich fluid component in the generation of primitive basaltic andesites and andesites from the Mt. Shasta region, N. California. *Contributions to Mineralogy and Petrology*, 142(4), 375-396.

Guffanti, M., & Weaver, C. S. (1988). Distribution of late Cenozoic volcanic vents in the Cascade Range: Volcanic arc segmentation and regional tectonic considerations. *Journal of Geophysical Research: Solid Earth* (1978–2012), 93(B6), 6513-6529.

Guffanti, M., Clynne, M. A., Smith, J. G., Muffler, L. J. P., & Bullen, T. D. (1990). Late Cenozoic volcanism, subduction, and extension in the Lassen region of California, southern Cascade Range. *Journal of Geophysical Research: Solid Earth* (1978–2012), 95(B12), 19453-19464.

Hacker, B. R. (2008). H_2O subduction beyond arcs. *Geochemistry, Geophysics, Geosystems*, 9(3).

Hermann, J., Spandler, C., Hack, A., & Korsakov, A. V. (2006). Aqueous fluids and hydrous melts in high-pressure and ultra-high pressure rocks: implications for element transfer in subduction zones. *Lithos*, 92(3), 399-417.

Hirschmann, M. M., Baker, M. B., & Stolper, E. M. (1998). The effect of alkalis on the silica content of mantle-derived melts. *Geochimica et Cosmochimica Acta*, 62(5), 883-902.

Hughes, S. S., & Taylor, E. M. (1986). Geochemistry, petrogenesis, and tectonic implications of central High Cascade mafic platform lavas. *Geological Society of America Bulletin*, 97(8), 1024-1036.

Ishikawa, T., & Nakamura, E. (1993). Boron isotope systematics of marine sediments. *Earth and Planetary Science Letters*, 117(3), 567-580.

Ishikawa, T., & Tera, F. (1999). Two isotopically distinct fluid components involved in the Mariana arc: Evidence from Nb/B ratios and B, Sr, Nd, and Pb isotope systematics. *Geology,* 27(1), 83-86.

Ishikawa, T., Tera, F., & Nakazawa, T. (2001). Boron isotope and trace element systematics of the three volcanic zones in the Kamchatka arc. *Geochimica et Cosmochimica Acta*, 65(24), 4523-4537.

Jégo, S., & Dasgupta, R. (2013). Fluid-present melting of sulfide-bearing ocean-crust: Experimental constraints on the transport of sulfur from subducting slab to mantle wedge. *Geochimica et Cosmochimica Acta*, 110, 106-134.

Johnson, E. R., Wallace, P. J., Cashman, K. V., Granados, H. D., & Kent, A. J. (2008). Magmatic volatile contents and degassing-induced crystallization at Volcán Jorullo, Mexico: implications for melt evolution and the plumbing systems of monogenetic volcanoes. *Earth and Planetary Science Letters*, 269(3), 478-487.

Kelemen, P. B., Shimizu, N., & Dunn, T. (1993). Relative depletion of niobium in some arc magmas and the continental crust: partitioning of K, Nb, La and Ce during melt/rock reaction in the upper mantle. *Earth and Planetary Science Letters*, 120(3), 111-134.

Kessel, R., Schmidt, M. W., Ulmer, P., & Pettke, T. (2005). Trace element signature of subduction-zone fluids, melts and supercritical liquids at 120–180 km depth. *Nature,* 437(7059), 724-727.

Kirby, S., Wang, K., & Dunlop, S. (Eds.). (2002). The Cascadia Subduction Zone and Related Subduction Systems: Seismic Structure, Intraslab Earthquakes and Processes, and Earthquake Hazards (pp. 79-80). US Geological Survey.

Klimm, K., Blundy, J. D., & Green, T. H. (2008). Trace element partitioning and accessory phase saturation during H_2O-saturated melting of basalt with implications for subduction zone chemical fluxes. *Journal of Petrology*, 49(3), 523-553.

Krawczynski, M. J., Grove, T. L., & Behrens, H. (2012). Amphibole stability in primitive arc magmas: effects of temperature, H_2O content, and oxygen fugacity. *Contributions to Mineralogy and Petrology*, 164(2), 317-339.

Leeman, W. P., Tonarini, S., Chan, L. H., & Borg, L. E. (2004). Boron and lithium isotopic variations in a hot subduction zone—the southern Washington Cascades. *Chemical Geology*, 212(1), 101-124.

Liu, K., Levander, A., Zhai, Y., Porritt, R. W., & Allen, R. M. (2012). Asthenospheric flow and lithospheric evolution near the Mendocino Triple Junction. *Earth and Planetary Science Letters*, 323, 60-71.

Lloyd, A. S., Plank, T., Ruprecht, P., Hauri, E. H., & Rose, W. (2013). Volatile loss from melt inclusions in pyroclasts of differing sizes. *Contributions to Mineralogy and Petrology*, 165(1), 129-153.

Loewen, M. W., & Kent, A. J. (2012). Sources of elemental fractionation and uncertainty during the analysis of semi-volatile metals in silicate glasses using LA-ICP-MS. *Journal of Analytical Atomic Spectrometry*, 27(9), 1502-1508.

Le Voyer, M., Rose-Koga, E. F., Shimizu, N., Grove, T. L., & Schiano, P. (2010). Two contrasting H_2O-rich components in primary melt inclusions from Mount Shasta. Journal of Petrology, 51(7), 1571-1595.

Manea, V. C., Leeman, W. P., Gerya, T., Manea, M., & Zhu, G. (2014). Subduction of fracture zones controls mantle melting and geochemical signature above slabs. *Nature communications*, 5.

Manning, C. E. (2004). The chemistry of subduction-zone fluids. *Earth and Planetary Science Letters*, 223(1), 1-16.

Marschall, H. R., & Monteleone, B. D. (2014). Boron Isotope Analysis of Silicate Glass with Very Low Boron Concentrations by Secondary Ion Mass Spectrometry. *Geostandards and Geoanalytical Research.*

Marschall, H. R., Altherr, R., & Rüpke, L. (2007). Squeezing out the slab—modelling the release of Li, Be and B during progressive high-pressure metamorphism. *Chemical Geology*, 239(3), 323-335.

Mullen, E. K., & Weis, D. (2015). Evidence for trench-parallel mantle flow in the northern Cascade Arc from basalt geochemistry. *Earth and Planetary Science Letters*, 414, 100-107.

Nedimović, M. R., Bohnenstiehl, D. R., Carbotte, S. M., Canales, J. P., & Dziak, R. P. (2009). Faulting and hydration of the Juan de Fuca plate system. *Earth and Planetary Science Letters*, 284(1), 94-102.

Peccerillo, A., & Taylor, S. R. (1976). Geochemistry of Eocene calc-alkaline volcanic rocks from the Kastamonu area, northern Turkey. *Contributions to mineralogy and petrology*, 58(1), 63-81.

Plank, T. (2005). Constraints from thorium/lanthanum on sediment recycling at subduction zones and the evolution of the continents. *Journal of Petrology*, 46(5), 921-944.

Plank, T., Cooper, L. B., & Manning, C. E. (2009). Emerging geothermometers for estimating slab surface temperatures. *Nature Geoscience*, 2(9), 611-615.

Portnyagin, M., Hoernle, K., Plechov, P., Mironov, N., & Khubunaya, S. (2007). Constraints on mantle melting and composition and nature of slab components in volcanic arcs from volatiles (H_2O, S, Cl, F) and trace elements in melt inclusions from the Kamchatka Arc. *Earth and Planetary Science Letters*, 255(1), 53-69.

Ranero, C. R., Morgan, J. P., McIntosh, K., & Reichert, C. (2003). Bending-related faulting and mantle serpentinization at the Middle America trench. *Nature*, 425(6956), 367-373.

Rose, E. F., Shimizu, N., Layne, G. D., & Grove, T. L. (2001). Melt production beneath Mt. Shasta from boron data in primitive melt inclusions. *Science*, 293(5528), 281-283.

Ryan, J. G., & Langmuir, C. H. (1993). The systematics of boron abundances in young volcanic rocks. *Geochimica et Cosmochimica Acta*, 57(7), 1489-1498.

Ruscitto, D. M., Wallace, P. J., Johnson, E. R., Kent, A. J. R., & Bindeman, I. N. (2010). Volatile contents of mafic magmas from cinder cones in the Central Oregon High Cascades: Implications for magma formation and mantle conditions in a hot arc. *Earth and Planetary Science Letters*, 298(1), 153-161.

Ruscitto, D. M., Wallace, P. J., & Kent, A. J. R. (2011). Revisiting the compositions and volatile contents of olivine-hosted melt inclusions from the Mount Shasta region: implications for the formation of high-Mg andesites. *Contributions to Mineralogy and Petrology*, 162(1), 109-132.

Ruscitto, D. M., Wallace, P. J., Cooper, L. B., & Plank, T. (2012). Global variations in H_2O/Ce: 2. Relationships to arc magma geochemistry and volatile fluxes. *Geochemistry, Geophysics, Geosystems,* 13(3).

Schmidt, M. W., & Poli, S. (1998). Experimentally based water budgets for dehydrating slabs and consequences for arc magma generation. *Earth and Planetary Science Letters*, 163(1), 361-379.

Sherrod, D. R., & Smith, J. G. (1990). Quaternary extrusion rates of the Cascade Range, northwestern United States and southern British Columbia. *Journal of Geophysical Research: Solid Earth* (1978–2012), 95(B12), 19465-19474.

Spandler, C., & Pirard, C. (2013). Element recycling from subducting slabs to arc crust: a review. *Lithos*, 170, 208-223.

Spandler, C., Pettke, T., & Hermann, J. (2014). Experimental study of trace element release during ultrahigh-pressure serpentinite dehydration. *Earth and Planetary Science Letters*, 391, 296-306.

Smith, H. J., Spivack, A. J., Staudigel, H., & Hart, S. R. (1995). The boron isotopic composition of altered oceanic crust. *Chemical Geology*, 126(2), 119-135.

Sun, S. S., & McDonough, W. F. (1989). Chemical and isotopic systematics of oceanic basalts: implications for mantle composition and processes. *Geological Society, London, Special Publications*, 42(1), 313-345.

Syracuse, E. M., van Keken, P. E., & Abers, G. A. (2010). The global range of subduction zone thermal models. *Physics of the Earth and Planetary Interiors*, 183(1), 73-90.

Till, C. B., Grove, T. L., Carlson, R. W., Donnelly-Nolan, J. M., Fouch, M. J., Wagner, L. S., & Hart, W. K. (2013). Depths and temperatures of< 10.5 Ma mantle melting and the lithosphere-asthenosphere boundary below southern Oregon and northern California. *Geochemistry, Geophysics, Geosystems*, 14(4), 864-879.

Tonarini, S., Armienti, P., D'Orazio, M., & Innocenti, F. (2001). Subduction-like fluids in the genesis of Mt. Etna magmas: evidence from boron isotopes and fluid mobile elements. Earth and Planetary Science Letters, 192(4), 471-483.

Wada, I., & Wang, K. (2009). Common depth of slab-mantle decoupling: Reconciling diversity and uniformity of subduction zones. *Geochemistry, Geophysics, Geosystems*, 10(10).

Wada, I., Behn, M. D., & Shaw, A. M. (2012). Effects of heterogeneous hydration in the incoming plate, slab rehydration, and mantle wedge hydration on slab-derived H_2O flux in subduction zones. *Earth and Planetary Science Letters*, 353, 60-71.

Wannamaker, P. E., Booker, J. R., Jones, A. G., Chave, A. D., Filloux, J. H., Waff, H. S., & Law, L. K. (1989). Resistivity cross section through the Juan de Fuca subduction system and its tectonic implications. *Journal of Geophysical Research: Solid Earth* (1978–2012), 94(B10), 14127-14144.

Weis, D., Kieffer, B., Maerschalk, C., Barling, J., De Jong, J., Williams, G. A., ... & Mahoney, J. B. (2006). High-precision isotopic characterization of USGS reference materials by TIMS and MC-ICP-MS. *Geochemistry, Geophysics, Geosystems*, 7(8).

Weis, D., Kieffer, B., Hanano, D., Nobre Silva, I., Barling, J., Pretorius, W. & Mattielli, N. (2007). Hf isotope compositions of US Geological Survey reference materials. *Geochemistry, Geophysics, Geosystems*, 8(6).

Wilson, D. S. (2002). The Juan de Fuca plate and slab: Isochron structure and Cenozoic plate motions. US Geological Survey Open-File Report, 02-328.

White, S. M., Crisp, J. A., & Spera, F. J. (2006). Long-term volumetric eruption rates and magma budgets. *Geochemistry, Geophysics, Geosystems*, 7(3).

Workman, R. K., & Hart, S. R. (2005). Major and trace element composition of the depleted MORB mantle (DMM). *Earth and Planetary Science Letters*, 231(1), 53-72.

van Keken, P. E., Hacker, B. R., Syracuse, E. M., & Abers, G. A. (2011). Subduction factory: 4. Depth-dependent flux of H_2O from subducting slabs worldwide. *Journal of Geophysical Research: Solid Earth* (1978–2012), 116(B1).

Walowski, K. J., Wallace, P. J., Hauri, E. H., Wada, I., & Clynne, M. A. (2015). Slab melting beneath the Cascade Arc driven by dehydration of altered oceanic peridotite. *Nature Geoscience*, 8(5), 404-408.

Yogodzinski, G. M., Kay, R. W., Volynets, O. N., Koloskov, A. V., & Kay, S. M. (1995). Magnesian andesite in the western Aleutian Komandorsky region: implications for slab melting and processes in the mantle wedge. *Geological Society of America Bulletin*, 107(5), 505-519.

Chapter IV

Anderson, A. T. (1974). Evidence for a picritic, volatile-rich magma beneath Mt. Shasta, California. *Journal of Petrology*, *15*(2), 243-267.

Beattie, P. (1994). Systematics and energetics of trace-element partitioning between olivine and silicate melts: implications for the nature of mineral/melt partitioning. *Chemical Geology*, *117*(1), 57-71.

Berge, P. A., & Stauber, D. A. (1987). Seismic refraction study of upper crustal structure in the Lassen Peak Area, northern California. *Journal of Geophysical Research: Solid Earth (1978–2012)*, *92*(B10), 10571-10579.

Blatter, D. L., Sisson, T. W., & Hankins, W. B. (2013). Crystallization of oxidized, moderately hydrous arc basalt at mid-to lower-crustal pressures: implications for andesite genesis. *Contributions to Mineralogy and Petrology*,*166*(3), 861-886.

Brenna, M., Cronin, S. J., Nemeth, K., Smith, I. E., & Sohn, Y. K. (2011). The influence of magma plumbing complexity on monogenetic eruptions, Jeju Island, Korea. *Terra Nova*, *23*(2), 70-75.

Brenna, M., Cronin, S. J., Smith, I. E., Sohn, Y. K., & Németh, K. (2010). Mechanisms driving polymagmatic activity at a monogenetic volcano, Udo, Jeju Island, South Korea. *Contributions to Mineralogy and Petrology*, *160*(6), 931-950.

Borg, L. E., Clynne, M. A., & Bullen, T. D. (1997). The variable role of slab-derived fluids in the generation of a suite of primitive calc-alkaline lavas from the southernmost Cascades, Calilornia. *Canadian Mineralogist*, *35*, 425-452.

Borg, L. E., Blichert-Toft, J., & Clynne, M. A. (2002). Ancient and modern subduction zone contributions to the mantle sources of lavas from the Lassen region of California inferred from Lu–Hf isotopic systematics. *Journal of Petrology*, *43*(4), 705-723.

Bucholz, C. E., Gaetani, G. A., Behn, M. D., & Shimizu, N. (2013). Post-entrapment modification of volatiles and oxygen fugacity in olivine-hosted melt inclusions. *Earth and Planetary Science Letters*, *374*, 145-155.

Cecil, M. R., Rotberg, G. L., Ducea, M. N., Saleeby, J. B., & Gehrels, G. E. (2012). Magmatic growth and batholithic root development in the northern Sierra Nevada, California. *Geosphere*, *8*(3), 592-606.

Clynne, M. A. (1993). *Geologic studies of the Lassen volcanic center, Cascade Range, California*. University of California, Santa Cruz.

Clynne, M. A. (2011, December). Stratigraphy and compositional evolution of Cinder Cone, a composite monogenetic cone in Lassen Volcanic National Park, California. In *AGU Fall Meeting Abstracts* (Vol. 1, p. 2621).

Clynne, M. A., & Muffler, L. J. P. (2010). *Geologic map of Lassen Volcanic National Park and vicinity, California*. US Department of the Interior, US Geological Survey.

Danyushevsky, L. V., Della-Pasqua, F. N., & Sokolov, S. (2000). Re-equilibration of melt inclusions trapped by magnesian olivine phenocrysts from subduction-related magmas: petrological implications. *Contributions to Mineralogy and Petrology*, *138*(1), 68-83.

Danyushevsky, L. V., & Plechov, P. (2011). Petrolog3: Integrated software for modeling crystallization processes. *Geochemistry, Geophysics, Geosystems*, *12*(7).

Dixon, J. E., & Pan, V. (1995). Determination of the molar absorptivity of dissolved carbonate in basanitic glass. *American Mineralogist*, *80*(11-12), 1339-1342.

Dohmen, R., & Chakraborty, S. (2007). Fe–Mg diffusion in olivine II: point defect chemistry, change of diffusion mechanisms and a model for calculation of diffusion coefficients in natural olivine. *Physics and Chemistry of Minerals*, *34*(6), 409-430.

Erlund, E. J., Cashman, K. V., Wallace, P. J., Pioli, L., Rosi, M., Johnson, E., & Granados, H. D. (2010). Compositional evolution of magma from Parícutin Volcano, Mexico: the tephra record. *Journal of Volcanology and Geothermal Research*, *197*(1), 167-187.

Esposito, R., Bodnar, R. J., Danyushevsky, L. V., De Vivo, B., Fedele, L., Hunter, J., ... & Shimizu, N. (2011). Volatile evolution of magma associated with the Solchiaro eruption in the Phlegrean Volcanic District (Italy). *Journal of Petrology*, *52*(12), 2431-2460.

Ford, C. E., Russell, D. G., Craven, J. A., & Fisk, M. R. (1983). Olivine-liquid equilibria: temperature, pressure and composition dependence of the crystal/liquid cation partition coefficients for Mg, Fe2+, Ca and Mn. *Journal of Petrology*, *24*(3), 256-266.

Gaetani, G. A., & Grove, T. L. (1998). The influence of water on melting of mantle peridotite. *Contributions to Mineralogy and Petrology*, *131*(4), 323-346.

Gaetani, G. A., O'Leary, J. A., Shimizu, N., Bucholz, C. E., & Newville, M. (2012). Rapid reequilibration of H_2O and oxygen fugacity in olivine-hosted melt inclusions. *Geology*, *40*(10), 915-918.

Ghiorso, M. S., Hirschmann, M. M., Reiners, P. W., & Kress, V. C. (2002). The pMELTS: A revision of MELTS for improved calculation of phase relations and major element partitioning related to partial melting of the mantle to 3 GPa. *Geochemistry, Geophysics, Geosystems*, 3(5), 1-35.

Grove, T. L., Kinzler, R. J., Baker, M. B., Donnelly-Nolan, J. M., & Lesher, C. E. (1988). Assimilation of granite by basaltic magma at Burnt Lava flow, Medicine Lake volcano, northern California: decoupling of heat and mass transfer. *Contributions to Mineralogy and Petrology*, *99*(3), 320-343.

Grove, T. L., Chatterjee, N., Parman, S. W., & Médard, E. (2006). The influence of $_{H2O}$ on mantle wedge melting. *Earth and Planetary Science Letters*, *249*(1), 74-89.

Gualda, G. A., Ghiorso, M. S., Lemons, R. V., & Carley, T. L. (2012). Rhyolite-MELTS: a modified calibration of MELTS optimized for silica-rich, fluid-bearing magmatic systems. *Journal of Petrology*, *53*(5), 875-890.

Guffanti, M., Clynne, M. A., Smith, J. G., Muffler, L. J. P., & Bullen, T. D. (1990). Late Cenozoic volcanism, subduction, and extension in the Lassen region of California, southern Cascade Range. *Journal of Geophysical Research: Solid Earth (1978–2012)*, *95*(B12), 19453-19464.

Hartley, M. E., Maclennan, J., Edmonds, M., & Thordarson, T. (2014). Reconstructing the deep CO_2 degassing behaviour of large basaltic fissure eruptions. *Earth and Planetary Science Letters*, *393*, 120-131.

Hauri, E. H., Wagner, T. P., & Grove, T. L. (1994). Experimental and natural partitioning of Th, U, Pb and other trace elements between garnet, clinopyroxene and basaltic melts. *Chemical Geology*, *117*(1), 149-166.

Heiken, G. (1978). Characteristics of tephra from cinder cone, Lassen volcanic national park, California. *Bulletin Volcanologique*, *41*(2), 119-130.

165

Hildreth, W. (2007). Quaternary magmatism in the Cascades-geologic perspectives. *US Geological Survey professional paper*, (1744), 1-125.

Hirschmann, M. M., Tenner, T., Aubaud, C., & Withers, A. C. (2009). Dehydration melting of nominally anhydrous mantle: the primacy of partitioning. *Physics of the Earth and Planetary Interiors*, *176*(1), 54-68.

Holloway, J. R., & Blank, J. G. (1994). Application of experimental results to COH species in natural melts. *Reviews in Mineralogy and Geochemistry*, *30*(1), 187-230.

Iacono-Marziano, G., Morizet, Y., Le Trong, E., & Gaillard, F. (2012). New experimental data and semi-empirical parameterization of H_2O–CO_2 solubility in mafic melts. *Geochimica et Cosmochimica Acta*, *97*, 1-23.

Johnson, E. R., Wallace, P. J., Cashman, K. V., Granados, H. D., & Kent, A. J. (2008). Magmatic volatile contents and degassing-induced crystallization at Volcán Jorullo, Mexico: implications for melt evolution and the plumbing systems of monogenetic volcanoes. *Earth and Planetary Science Letters*, *269*(3), 478-487.

Johnson, E. R., Wallace, P. J., Cashman, K. V., & Granados, H. D. (2010). Degassing of volatiles (H_2O, CO_2, S, Cl) during ascent, crystallization, and eruption at mafic monogenetic volcanoes in central Mexico. *Journal of Volcanology and Geothermal Research*, *197*(1), 225-238.

Kumazawa, M., & Anderson, O. L. (1969). Elastic moduli, pressure derivatives, and temperature derivatives of single-crystal olivine and single-crystal forsterite. Journal of Geophysical Research, 74(25), 5961-5972.

Lange, R. L., & Carmichael, I. S. (1990). Thermodynamic properties of silicate liquids with emphasis on density, thermal expansion and compressibility. Reviews in Mineralogy and Geochemistry, 24(1), 25-64.

Le Bas, M. J., Le Maitre, R. W., Streckeisen, A., & Zanettin, B. (1986). A chemical classification of volcanic rocks based on the total alkali-silica diagram. *Journal of Petrology*, 27(3), 745-750.

Le Voyer, M., Rose-Koga, E. F., Shimizu, N., Grove, T. L., & Schiano, P. (2010). Two contrasting H_2O-rich components in primary melt inclusions from Mount Shasta. *Journal of Petrology*, 51(7), 1571-1595.

Leeman, W. P., Tonarini, S., Chan, L. H., & Borg, L. E. (2004). Boron and lithium isotopic variations in a hot subduction zone—the southern Washington Cascades. *Chemical Geology*, *212*(1), 101-124.

Lloyd, A. S., Plank, T., Ruprecht, P., Hauri, E. H., & Rose, W. (2013). Volatile loss from melt inclusions in pyroclasts of differing sizes. *Contributions to Mineralogy and Petrology*, *165*(1), 129-153.

Loewen, M. W., & Kent, A. J. (2012). Sources of elemental fractionation and uncertainty during the analysis of semi-volatile metals in silicate glasses using LA-ICP-MS. *Journal of Analytical Atomic Spectrometry*, *27*(9), 1502-1508.

Lowenstern, J. B. (1995). Applications of silicate-melt inclusions to the study of magmatic volatiles. *Magmas, Fluids and Ore Deposits. Mineralogical Association of Canada Short Course*, *23*, 71-99.

Luhr, J. F. (2001). Glass inclusions and melt volatile contents at Paricutin Volcano, Mexico. *Contributions to Mineralogy and Petrology*, *142*(3), 261-283.

Luhr, J. F., & Carmichael, I. S. (1985). Jorullo Volcano, Michoacán, Mexico (1759–1774): the earliest stages of fractionation in calc-alkaline magmas. *Contributions to Mineralogy and Petrology*, *90*(2-3), 142-161.

McBirney, A. R., Taylor, H. P., & Armstrong, R. L. (1987). Paricutin re-examined: a classic example of crustal assimilation in calc-alkaline magma.*Contributions to Mineralogy and Petrology*, *95*(1), 4-20.

Mallmann, G., & O'Neill, H. S. C. (2009). The crystal/melt partitioning of V during mantle melting as a function of oxygen fugacity compared with some other elements (Al, P, Ca, Sc, Ti, Cr, Fe, Ga, Y, Zr and Nb). *Journal of Petrology*, *50*(9), 1765-1794.

Marks, J.K. (2012). Physical Volcanology of the 1666 C.E. Cinder Cone Eruption, Lassen Volcanic National Park, California. University of Oregon.

McKenzie, D. A. N., & O'nions, R. K. (1991). Partial melt distributions from inversion of rare earth element concentrations. *Journal of Petrology*, *32*(5), 1021-1091.

Métrich, N., & Wallace, P. J. (2008). Volatile abundances in basaltic magmas and their degassing paths tracked by melt inclusions. *Reviews in Mineralogy and Geochemistry*, *69*(1), 363-402.

Moore, L. R. Gazel, E., Tuohy, R., Lloyd, A., Esposito, R., Steele-MacInnis, M., Hauri, E.H., Wallace, P.J., Plank, T., Bodnar, R.J. (2014). Bubbles matter: An assessment of the contribution of vapor bubbles to melt inclusion volatile budgets. *The American Mineralogist*, in press.

Newman, S., & Lowenstern, J. B. (2002). VolatileCalc: a silicate melt–H_2O–CO_2 solution model written in Visual Basic for Excel. *Computers & Geosciences*, *28*(5), 597-604.

Papale, P., Moretti, R., & Barbato, D. (2006). The compositional dependence of the saturation surface of $H_2O + CO_2$ fluids in silicate melts. *Chemical Geology*, *229*(1), 78-95.

Paster, T. P., Schauwecker, D. S., & Haskin, L. A. (1974). The behavior of some trace elements during solidification of the Skaergaard layered series.*Geochimica et Cosmochimica Acta*, *38*(10), 1549-1577.

Petry, C., Chakraborty, S., & Palme, H. (2004). Experimental determination of Ni diffusion coefficients in olivine and their dependence on temperature, composition, oxygen fugacity, and crystallographic orientation. *Geochimica et Cosmochimica Acta*, *68*(20), 4179-4188.

Pioli, L., Erlund, E., Johnson, E., Cashman, K., Wallace, P., Rosi, M., & Granados, H. D. (2008). Explosive dynamics of violent Strombolian eruptions: the eruption of Parícutin Volcano 1943–1952 (Mexico). *Earth and Planetary Science Letters*, *271*(1), 359-368.

Riker, J., (2005) The 1859 eruption of Mauna Loa Volcano, Hawaii: Controls on the development of long lava channels. Unpublished M.S. Thesis, University of Oregon.

Roberge, J., Wallace, P. J., White, R. V., & Coffin, M. F. (2005). Anomalous uplift and subsidence of the Ontong Java Plateau inferred from CO_2 contents of submarine basaltic glasses. *Geology*, *33*(6), 501-504.

Roedder, E. (1979). Origin and significance of magmatic inclusions. *Bulletin of Mineralogy*, *102*, 487-510.

Roggensack, K., Hervig, R. L., McKnight, S. B., & Williams, S. N. (1997). Explosive basaltic volcanism from Cerro Negro volcano: influence of volatiles on eruptive style. *Science*, *277*(5332), 1639-1642.

Ruprecht, P., & Plank, T. (2013). Feeding andesitic eruptions with a high-speed connection from the mantle. *Nature*, *500* (7460), 68-72.

Ruscitto, D. M., Wallace, P. J., Johnson, E. R., Kent, A. J. R., & Bindeman, I. N. (2010). Volatile contents of mafic magmas from cinder cones in the Central Oregon High Cascades: Implications for magma formation and mantle conditions in a hot arc. *Earth and Planetary Science Letters*, *298*(1), 153-161.

Ruscitto, D. M., Wallace, P. J., & Kent, A. J. R. (2011). Revisiting the compositions and volatile contents of olivine-hosted melt inclusions from the Mount Shasta region: implications for the formation of high-Mg andesites.*Contributions to Mineralogy and Petrology*, *162*(1), 109-132.

Saleeby, J. B., Shaw, H. F., Niemeyer, S., Moores, E. M., & Edelman, S. H. (1989). U/Pb, Sm/Nd and Rb/Sr geochronological and isotopic study of northern Sierra Nevada ophiolitic assemblages, California. *Contributions to Mineralogy and Petrology*, *102*(2), 205-220.

Schiano, P. (2003). Primitive mantle magmas recorded as silicate melt inclusions in igneous minerals. *Earth-Science Reviews*, *63*(1), 121-144.

Sheppard, P. R., Ort, M. H., Anderson, K. C., Clynne, M. A., & May, E. M. (2009). Multiple dendrochronological responses to the eruption of Cinder Cone, Lassen volcanic National Park, California. *Dendrochronologia*, *27*(3), 213-221.

Sherrod, D. R., & Smith, J. G. (1990). Quaternary extrusion rates of the Cascade Range, northwestern United States and southern British Columbia. *Journal of Geophysical Research: Solid Earth (1978–2012)*, *95*(B12), 19465-19474.

Straub, S. M., Gómez-Tuena, A., Zellmer, G. F., Espinasa-Perena, R., Stuart, F. M., Cai, Y., & Mesko, G. T. (2013). The processes of melt differentiation in arc volcanic rocks: Insights from OIB-type arc magmas in the central Mexican volcanic belt. *Journal of Petrology*, *54*(4), 665-701.

Suzuki, I. (1975). Thermal expansion of periclase and olivine, and their anharmonic properties. Journal of Physics of the Earth, 23(2), 145-159.

Wallace, P. J., Kamenetsky, V. S., & Cervantes, P. (2015). Melt inclusion CO_2 contents, pressures of olivine crystallization, and the problem of shrinkage bubbles. *American Mineralogist*, *100*(4), 787-794.

Walowski, K. J., Wallace, P. J., Hauri, E. H., Wada, I., & Clynne, M. A. (2015). Slab melting beneath the Cascade Arc driven by dehydration of altered oceanic peridotite. *Nature Geoscience*, *8*(5), 404-408.

Workman, R. K., & Hart, S. R. (2005). Major and trace element composition of the depleted MORB mantle (DMM). Earth and Planetary Science Letters, 231(1), 53-72.